Development of an Implantable Blood Flow and Pressure Monitor for Pulmonary Hypertension: New Finite Element Modelling Based Conductance Catheter Techniques for Measuring Blood Flow

by

Simon Ellis Locke

B.E. (Mechanical), University of Tasmania

Submitted in fulfilment of the

requirements for the degree of

Doctor of Philosophy

University of Tasmania

January, 2007

Declarations

This Thesis is my own work and contains no material that has been accepted for a degree or diploma by the University or any other institution, except by way of background material and duly acknowledged in the Thesis, and to the best of my knowledge and belief no material previously published or written by another person except where due acknowledgement is made in the text of the Thesis.

Signed: .....

Date: 25th January, 2007

This thesis is not to be made available for loan or copying for two years following the date this statement was signed. Following that time the thesis may be made available for loan and limited copying in accordance with the *Copyright Act 1968.*

Signed: .....

Date: 25th January, 2006

Abstract

Pulmonary hypertension patients could greatly benefit from use of an implantable blood flow and pressure monitor that can be used to derive pulmonary resistance. This thesis concentrates on the development of a suitable implantable sensor for measuring flow. Various methods for measuring flow are assessed. Conductance catheter techniques are proposed as some of the most promising, but suffer from limited accuracy. The main chapters of the thesis concentrate on the development of more accurate conductance catheter techniques. Realistic three-dimensional dynamic models of the heart, developed from MRI and tagged MRI scans, were used with finite element analysis to simulate the electric field arising from the conductance catheter in the heart. Results show that catheter movement and tissue impedance changes give non-negligible error using existing methods for calculating volume from impedance measurements. A new method for calculating volume from impedance measurements was developed that corrects for these and other errors. The new method finds the inverse mapping of a parameterised numerical model. It also allows use of additional data available from the conductance catheter technique, including data from different current source configurations and frequencies. The new technique was tested in a simplified model of the heart. Derivatives of the catheter measurements with respect to the model parameters were determined at one parameter configuration and formed into vectors. Derivative angles were then found between the vectors, providing a method for assessing the separability of the different model parameters. In addition they did not require creation of the inverse mapping. Two different types of techniques for creating the inverse mapping were tested. These were a new technique based on a distance metric and optimisation, and traditional artificial intelligence techniques. Even in the presence of no measurement error, limitations of traditional artificial intelligence techniques prevented successful application. The new technique performed to the order of accuracy of the numerical model on the same amount of data the traditional artificial intelligence techniques were trained on. The new technique was further developed to compensate for measurement error, and resulted in a further increase in accuracy. This thesis has developed and tested new conductance catheter methods, and has moved us a step closer to enabling practical development of an implantable blood flow and pressure monitor.

Acknowledgements

I would like to thank my supervisor, Dr. Timothy J. Gale, for many hours reviewing my work and filling out administrative forms for my project.

I would also like to thank my co-supervisor, Professor D. Kilpatrick, and Dr. Yong, from the School of Medicine, for helpful advice during the project.

Thanks are also extended to Wendy Strugnell from the Cardiovascular MRI Research Centre at The Prince Charles Hospital in Queensland and William P. Segars from the Johns Hopkins Outpatient Center in Baltimore for raw data used in this thesis for numerical modelling.

Finally I'd like to thank Mr D. Warren of Zentel Pty Ltd. for financial support of my project.

CONTENTS

Glossary

Derivative vector

Vector consisting of the partial derivatives of catheter measurements with respect to one particular parameter (Section 5.2).

Derivative angle

Angle between two derivative vectors.

Chapter 1. Introduction

Background

Development of implantable blood flow and pressure monitoring technology promises to provide improved health information with minimum inconvenience to patients as they go about their lives. The developed technology may also transfer to non-implantable monitoring. A potential application where the invasive nature of an implantable device out weighs potential risks is the pulmonary hypertension patient. Such patients have a short life expectancy and current treatment methods are only in an early stage of development.

The condition of pulmonary hypertension is the medical condition where there is unusually high blood pressure in the lungs and supplying artery (the pulmonary artery). This condition often leads to secondary conditions such as right heart failure and consequently has a very high mortality. Mechanisms involved include narrowing of the small blood vessels in the lungs, with obstruction of blood flow and the raising of pressures.

Current treatment is either with very expensive drugs or by heart and lung transplantation. Treatment drugs act to reduce the increase in vascular resistance in the small vessels in the lungs. Vascular resistance may be calculated by dividing vascular pressure drop by the vascular flow rate. Assuming a "normal" left atrial pressure, vascular resistance can be estimated knowing (mean) pulmonary artery pressure and flow rate (left atrial pressure is typically approximated as the capillary wedge pressure or end-diastole pulmonary artery pressure).

Pulmonary hypertension (primary) has only very recently started to draw attention from clinicians. This has been due to the recent introduction of pharmaceuticals to treat the condition. These pharmaceuticals however only treat the symptoms of the condition and not the cause. They delay death and provide a pre-death higher quality of life for those with the condition. Effects of the drugs are typically monitored with the six minute walk test (how far can a patient walk in six minutes). A more accurate assessment of pulmonary resistance would be beneficial in optimising selection and dosage. This would reduce costs and improve patient treatment. Improved ability to

measure the effect of drugs would allow more efficient drug development and better clinical trials (improved study end points).

Implantable technology is relatively mature. Catheters attached to implantable monitoring and control units have been extensively implanted. Pacemakers and implantable defibrillators have been the largest application of implantable technology. Implantable blood pressure (absolute pressure corrected by external atmospheric pressure measuring device) monitoring devices have recently become commercially available. They have been demonstrated to be reliable in long term trials. However, no implantable blood flow sensor has been developed for routine use. The difficulty is accurate continuous measurement of flow. Current high accuracy techniques are all intermittent and costly. Alternative techniques with the potential for continuous high-accuracy flow measurement currently suffer from impediments that limit their accuracy and practicality. The focus of this thesis is on developing blood flow sensing methods that have the potential to be used in an implanted device in a patient. This is ambitious, since even an equivalent non-implantable device has never been developed. The aim of the thesis is to move closer to achieving this goal.

The approach this thesis takes is to make an objective detailed assessment of the merits of different techniques for measuring blood flow. The thesis then concentrates on overcoming methodological limitations related to one of the more promising techniques, the conductance catheter. This approach is based on a broad foundation of previous research.

Aims

Specific aims of this thesis are to:

1. Identify the most promising techniques for an implantable blood flow sensor.
2. Develop a numerical model to simulate a conductance catheter.
3. Use this numerical model to determine the theoretical significance of error in existing conductance catheter methods due to the main variables (catheter position and tissue impedance).
4. Develop a method to correct for these main variables and other errors.
5. Further develop the new method by reducing the effect of noise.

Structure

The thesis is composed of seven chapters. These seven chapters comprise an introduction, background, literature review, three investigation chapters and a conclusion. The investigation chapters are structured with individual methods, results and discussion sections. There is limited interpretation of the data in the results section and the results and discussion sections should be read together to fully interpret the results.

The second chapter presents background information. Included is basic relevant anatomy and physiology of the heart related to aim two, and a detailed introduction to the conductance catheter technique, for the unfamiliar reader.

The third chapter presents a detailed literature review. It concentrates on addressing the first aim of the thesis and relevant research data related to aim two.

The fourth, fifth and sixth chapters are the investigation chapters. These main chapters of the thesis concentrate on the development of the conductance catheter technique. These chapters address aim three, four and five of the thesis respectively.

In chapter four, dynamic three-dimensional numerical models of the heart are developed to enable simulation of the conductance catheter. Two different models are used: one developed from MRI and one developed from tagged MRI data. The two models allow comparison of models developed from two different patients. One of the models (tagged MRI) is then used to assess the effect of catheter position and blood conductivity/myocardium conductivity on the conductance catheter output. No one has previously undertaken such detailed studies in the controlled environment of a realistic, three-dimensional numerical model. The outcome of these studies provide the motivation for the work in the next two investigation chapters.

In chapter five a new methodology for mapping conductance catheter voltages to blood flow (stroke volume) is developed. The approach involves developing an inverse solution to the numerical model. Two different inverse methods are applied and compared, a new technique based on a distance metric and optimisation, and the neural network (direct arbitrary function fitting) technique used commonly with

inverse problems. This chapter only assesses the performance of inverse mapping with no error. The outcome of this chapter provides motivation for the last investigation chapter.

In chapter six the new inverse technique is further developed based on probability concepts and applied to the inverse problem with error.

The conclusion brings the literature review and three investigation chapters together and provides direction for possible future work.

Chapter 2. Background

2.1 Introduction

This chapter presents material related to the second aim of the thesis and a detailed introduction to the conductance catheter technique for the unfamiliar reader. The first section covers basic heart anatomy and physiology. The second section, introduces the conductance catheter technique. Numerous raw figures carefully selected from books and research literature are included in this chapter. Diagrammatic explanations have been included from other sources to more efficiently communicate the discussions for the reader. These have been referenced as required by copyright law (review and criticism purpose).

2.2 Basic Heart Anatomy and Physiology

As indicated in Figure 2.2.1 the heart of a normal person contains two pumps in series. The right pump delivers blood to the lungs and receives blood from the body. The left pump delivers blood to the body and receives blood from the lungs. One way valves control the flow of blood into and out of the heart (not shown). The heart muscles contract to eject blood through the one way flow path created by the valves. The heart consists of four cavities. Blood flows into a receiving chamber, the right atrium, before flowing through a valve, the tricuspid valve, into the main pumping chamber, the right ventricle. From here the blood flows through another valve, the pulmonary valve, into the pulmonary trunk, which branches into two vessels, the right and left pulmonary arteries, which supply the right and left lungs respectively. Blood flows from the lungs through four vessels. These four vessels are the pulmonary veins. From these pulmonary veins the blood flows into a receiving chamber, the left atrium, then through a valve, the mitral valve, into the main pumping chamber, the left ventricle. From the left ventricle blood is ejected through another valve, the aortic valve, into a vessel, the aorta, which supplies blood to the body.

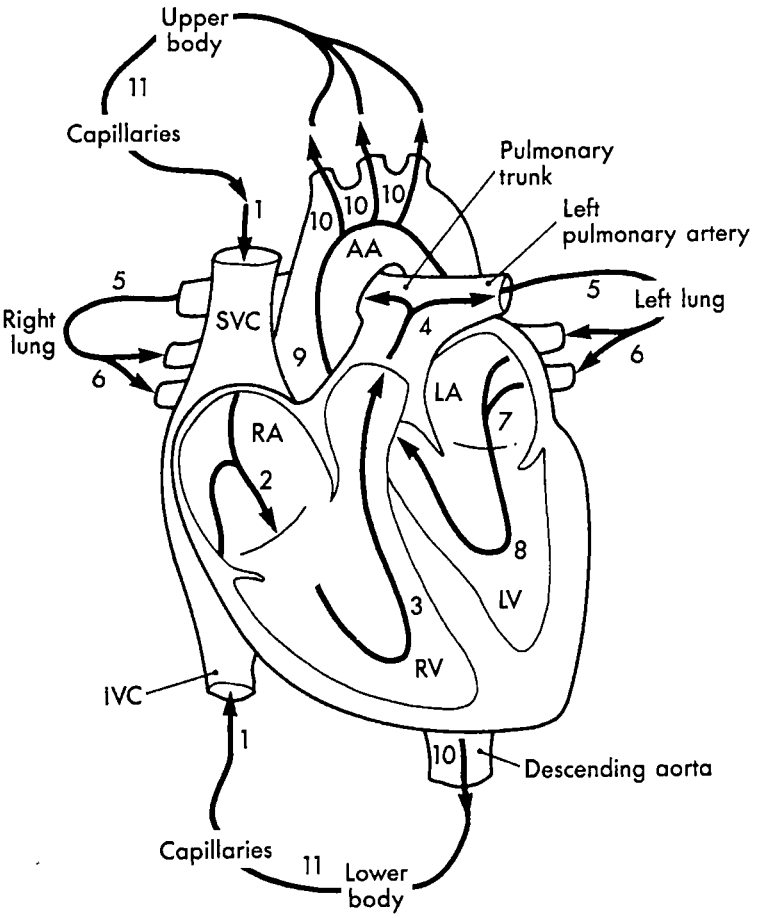

Fig. C-1 Blood flow through the heart and peripheral circulatory system. *AA*, Aortic arch; *IVC*, inferior vena cava; *LA*, left atrium; *LV*, left ventricle; *RA*, right atrium; *RV*, right ventricle; *SVC*, superior vena cava.

Figure 2.2.1: Schematic of blood flow path through the four chambers of the heart. [79].

Figure 2.2.2 shows the detailed blood flow from the heart through the body. Essentially the volume of blood that flows through the right side of the heart must be the same as the volume of blood that flows through the left side of the heart. A small amount of blood does actually bypass the right heart through the bronchial arteries, but this is very small (less than 1%) and practically negligible. The coronary arteries supply blood to the heart itself. One way valves in the veins of the extremities help to pump blood back to the heart against gravity. All blood vessels are non-rigid and distensible to some extent. However, the veins, carrying blood from tissues of the body back to the heart are considerably more distensible than the arteries which carry blood to the tissues.

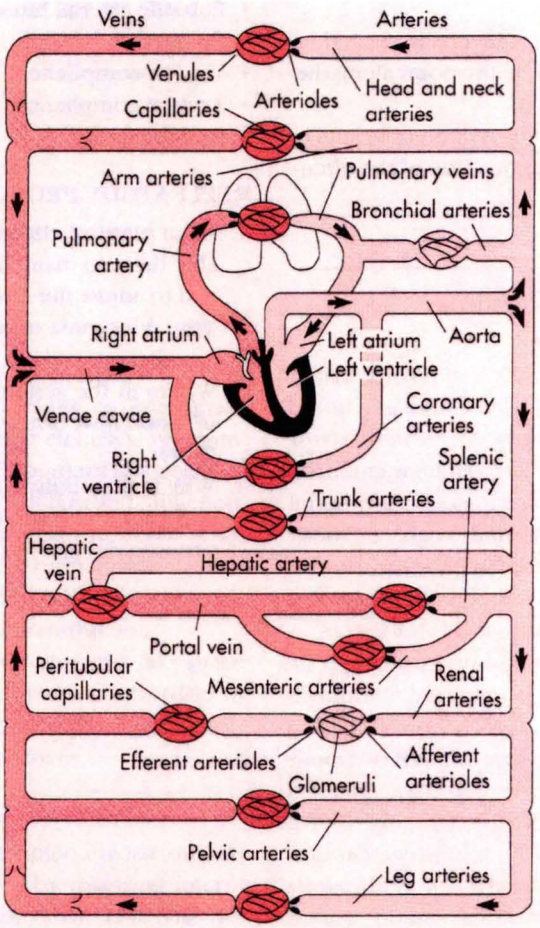

Figure 1-4 ■ Schematic diagram of the parallel and series arrangement of the vessels composing the circulatory system. The capillary beds are represented by thin lines connecting the arteries (on the right) with the veins (on the left). The crescent-shaped thickenings proximal to the capillary beds represent the arterioles (resistance vessels). (Redrawn from Green HD: In Glasser O, editor: *Medical physics*, vol 1, Chicago, 1944, Mosby-Year Book.)

Figure 2.2.2: Simplified schematic of the circulatory system - flow of blood from the heart around the body. [80].

Figure 2.2.3 shows the location of the heart in the body. The heart is located in the pericardium, a double membrane, fluid filled sac. This fluid filled sack is only slightly distensible and has limited ability to stretch limiting the volume of the heart in the short term. The inner membrane of the pericardial sac lies on the outer heart surface (epicardium) and the thicker outer membrane is the fibrous pericardium. On either side of the heart are the lungs contained in their own fluid filled sac. Below the lungs and heart is the diaphragm and below this, directly underneath the heart, is the liver (not shown). Adipose tissue or fat may lie around the various organs.

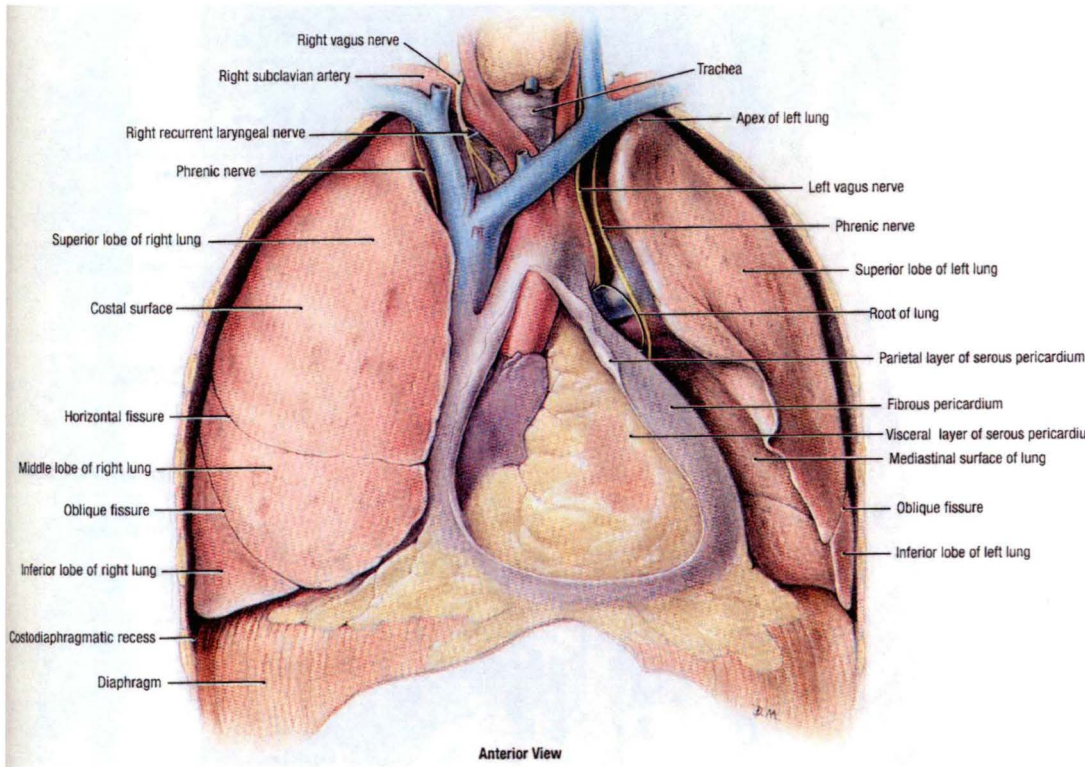

Figure 2.2.3: Heart located in the pericardium. [81].

The pericardial membrane inverts at the veins and arteries entering and exiting the heart as shown in Figure 2.2.4.

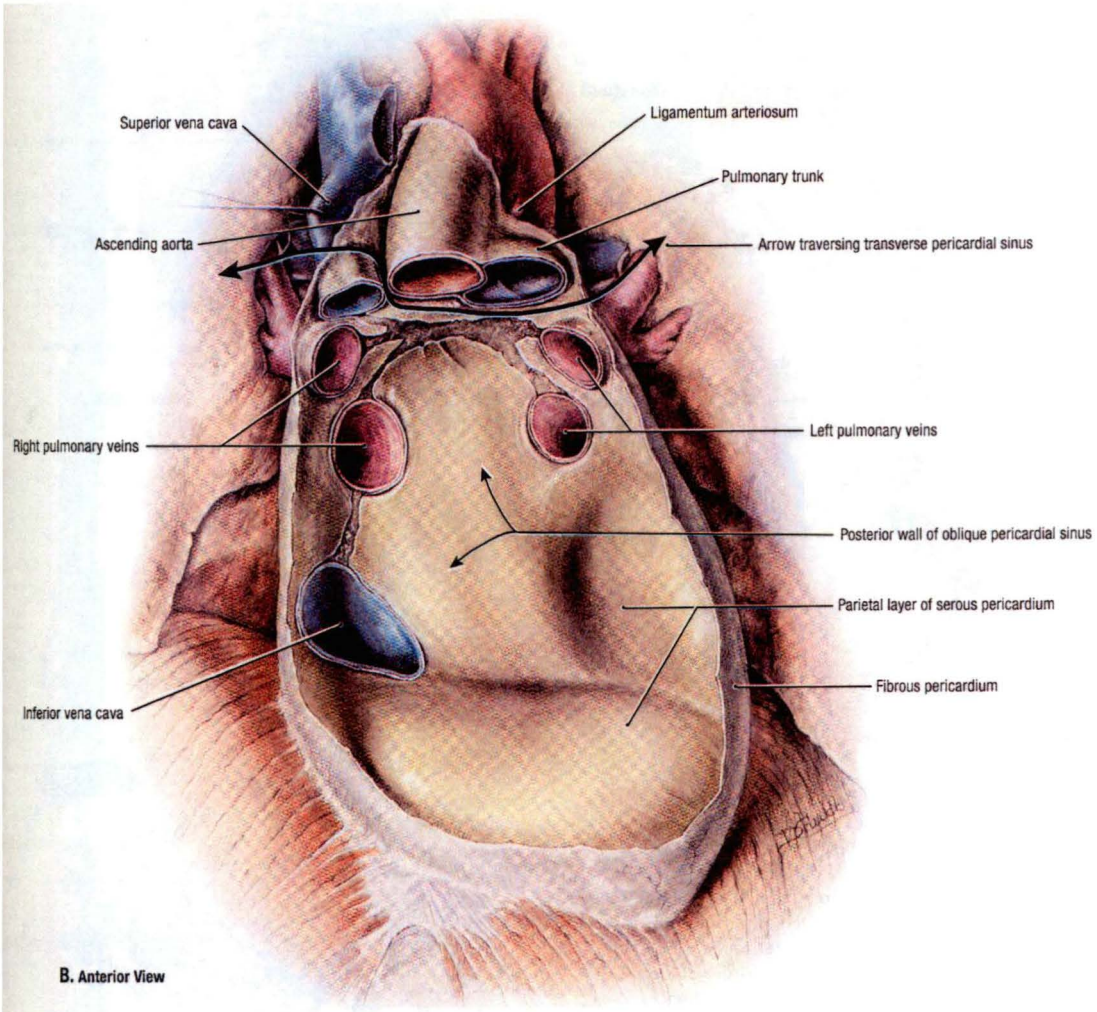

Figure 2.2.4: Pericardium membrane with heart removed. [81].

The lungs do not completely surround the heart as can be seen in body cross section of Figure 2.2.5. The pericardium is attached rigidly to the sternum at the front by way of the sternopericardial ligaments (not shown). One of these ligaments is near the base of the pericardium, the other is higher up. Higher up still, the thymus (not shown) lies between the pericardium and sternum. The thymus is only significant in size during childhood. In humans the base of the pericardium is bonded to the diaphragm.

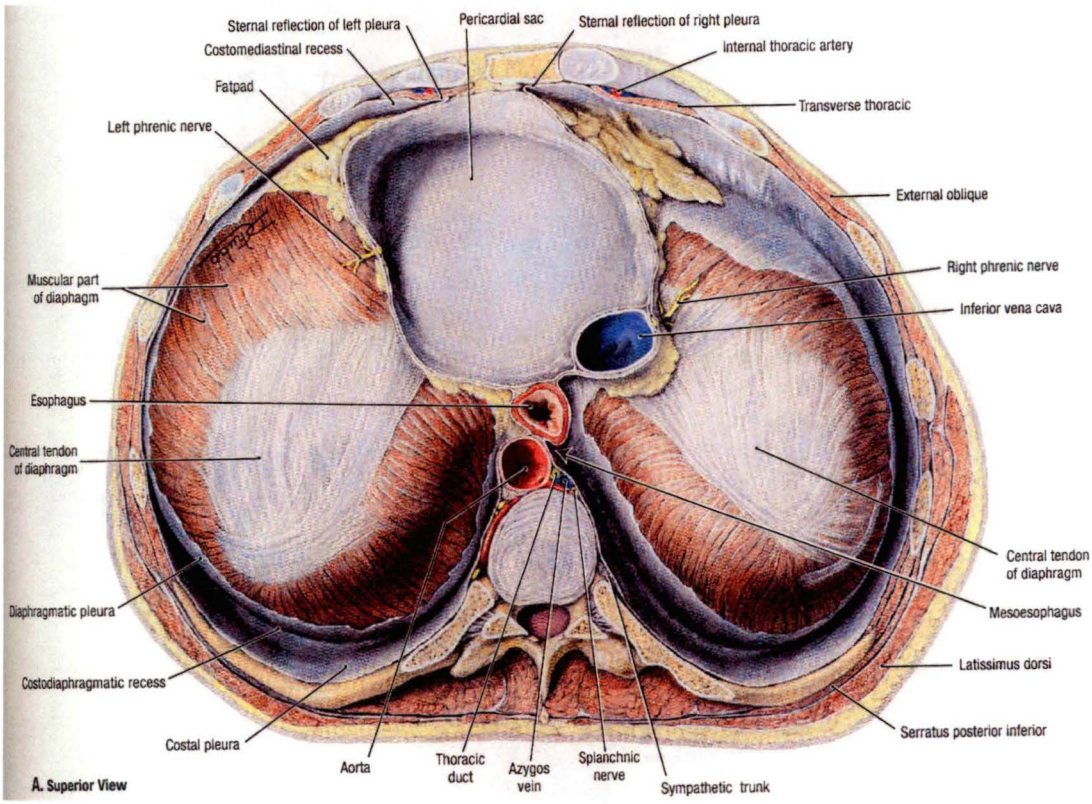

Figure 2.2.5: Cross section of the body at the base of the pericardium. [81].

Figure 2.2.6 shows the location of the heart underneath the sternum and ribs/costal cartilages.

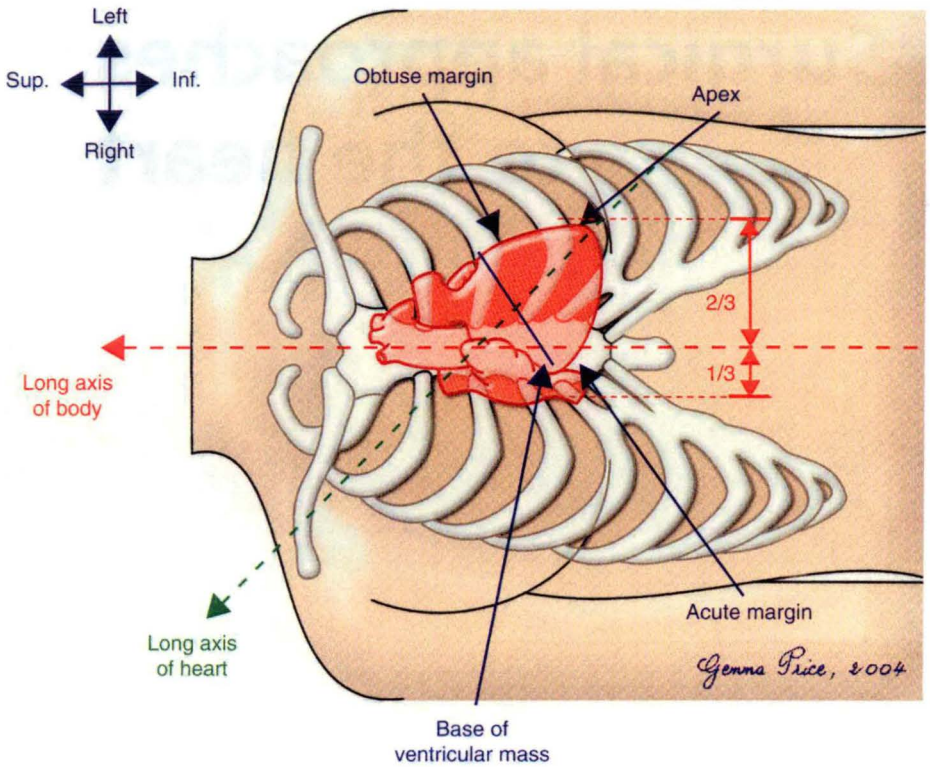

Figure 2.2.6: Position of the heart relative to external body markings. [82].

Figure 2.2.7 shows an anterior (front) view of the heart removed from the pericardium. The cut away shows the right ventricle, pulmonary valve and tricuspid valve. Also shown is the outside of the right atrium towards the top left of the image and the end of the left atrium wrapping around the heart on the top right of the image.

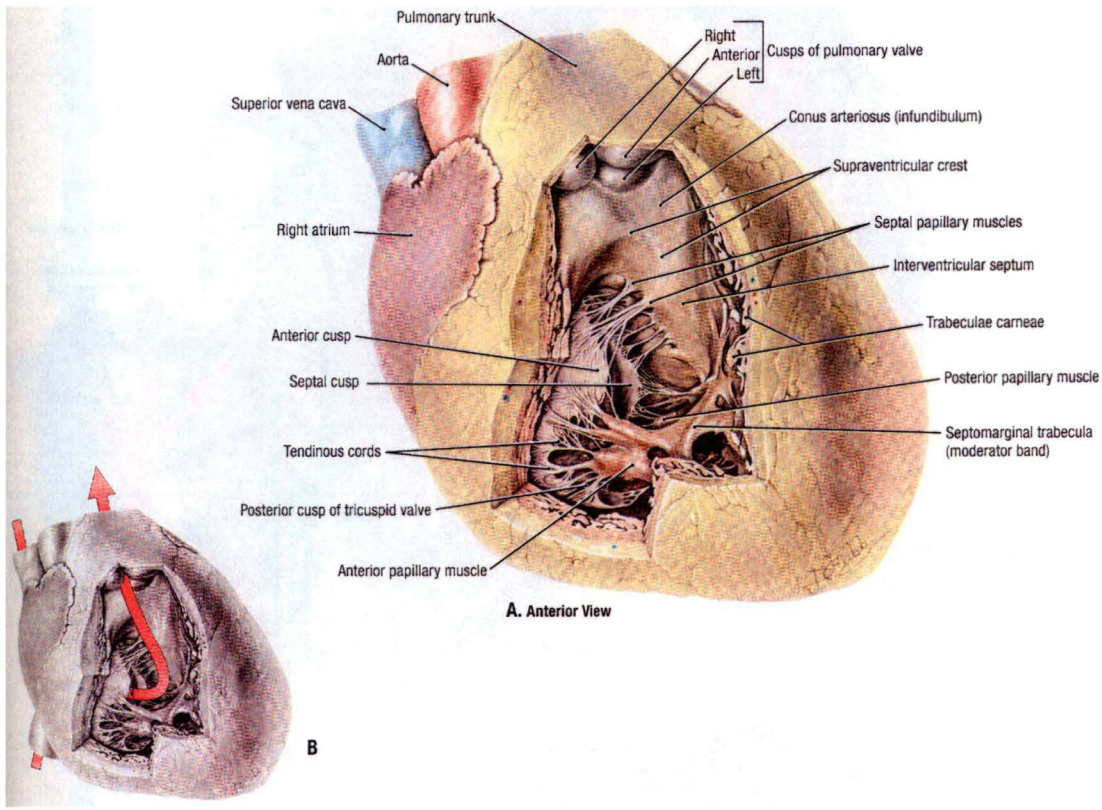

Figure 2.2.7: A.) Anterior view of the heart removed from the pericardium with cutaway of the right ventricle. B.) Blood flow through the right side of the heart. [81].

Figure 2.2.8 shows a surgical view of the heart in the pericardium after removal of the sternum and opening of pericardium. The image is rotated 90 degrees anticlockwise to that in Figure 2.2.7. In contrast to Figure 2.2.7, this heart shows unusually little epicardial fat.

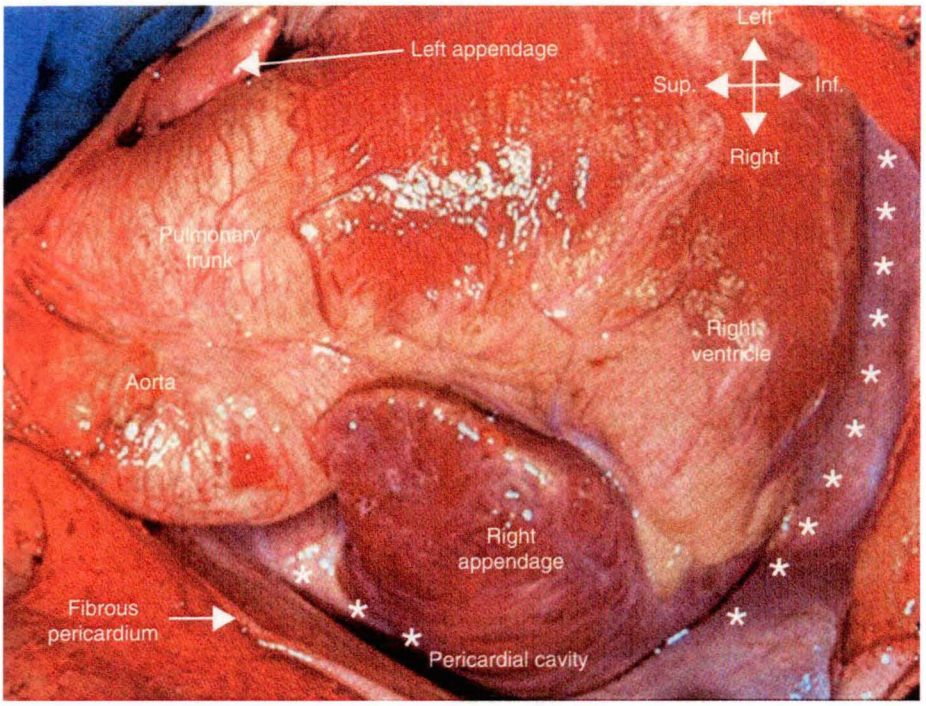

Figure 2.2.8: Surgical view of the heart in the pericardium with the sternum removed and pericardium opened. [82].

Figure 2.2.9 shows a posterior (back) view of the heart removed from the pericardium. This figure shows the matching cut surfaces of the heart in Figure 2.2.4. The outer surface of the left ventricle is shown on the bottom left of the image. Entry of the four pulmonary veins to the left atria is shown along with entry of the superior vena cava and inferior vena cava to the right atrium. The aorta from the left ventricle passes around the pulmonary trunk from the right ventricle.

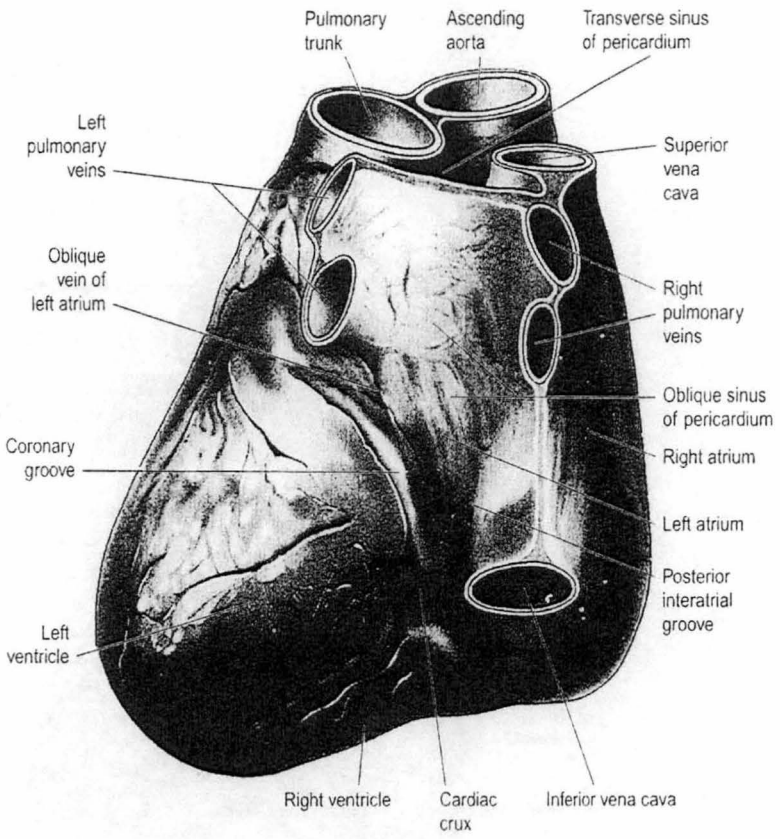

Fig. 60.2 The base and the diaphragmatic surface of the heart. The serosal pericardium is *in situ* and its cut edge is seen around the great vessels; its disposition is highly schematic (recesses omitted). *See* text for additional details. The cardiac crux results from the confluence of the posterior interatrial groove, the posterior atrioventricular groove and the posterior interventricular groove.

Figure 2.2.9: Posterior view of the heart removed from the pericardium. [83]

The apex, base of the ventricles and the long axis of the heart are indicated in Figure 2.2.6. Figure 2.1.10 shows slices of a real heart perpendicular to the long axis of the heart from apex (bottom) to base of ventricles (top). The circumference of the circular shaped hole is the left ventricle endocardium. The circumference of the crescent shaped hole is the right ventricular endocardium. The white tissue is adipose tissue or fat. The darker tissue is heart muscle (myocardium).

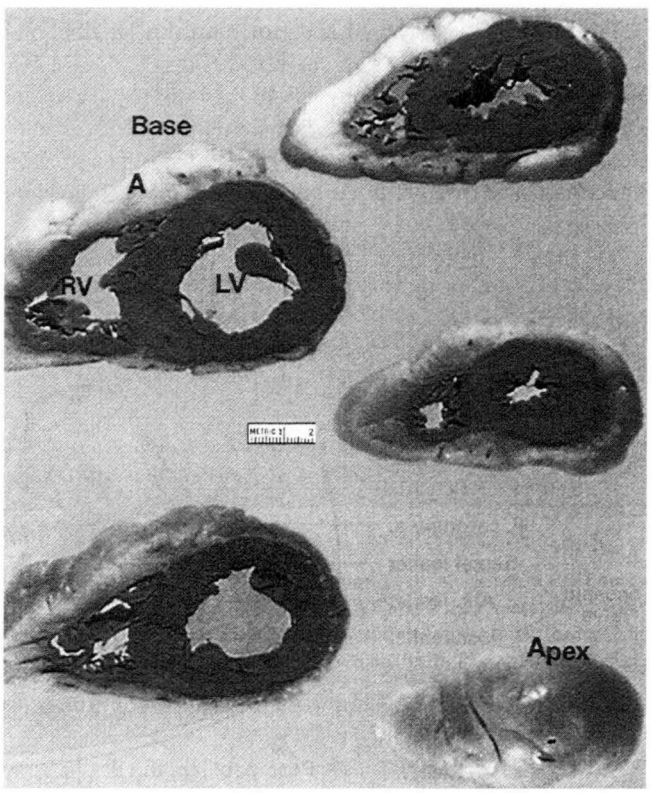

Figure 2.2.10: Short axis slices of the ventricles from apex bottom to base. [84]

Figure 2.2.11 shows a heart cut along the long axis of the heart to reveal the four chambers. Note the thicker wall of the left ventricle to the right ventricle, the thin walls of the atrium, and trabecularised (uneven) endocardium of the right ventricle and to a lesser extent trabecularised endocardium of the left ventricle.

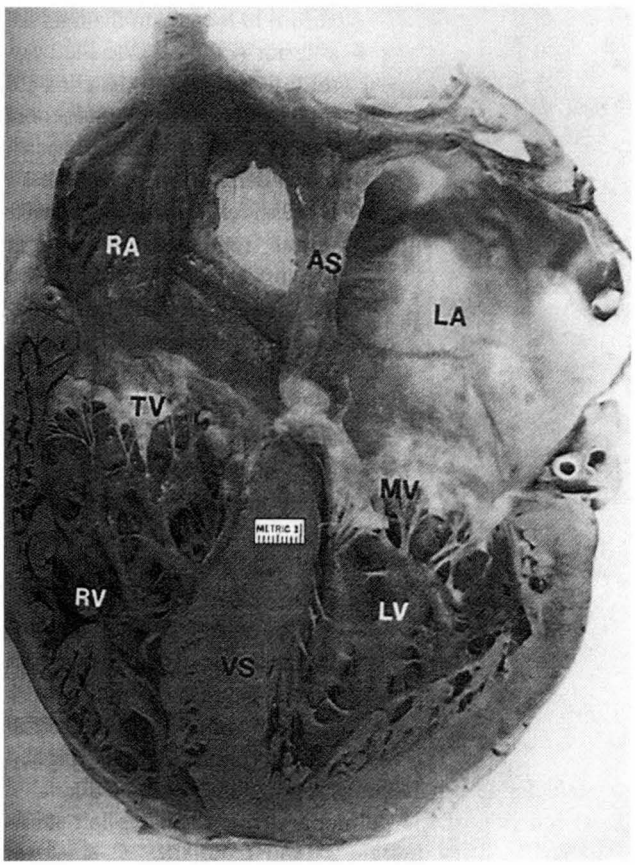

Figure 2.2.11: Long axis cut of the heart revealing the four chambers. [84]

Figure 2.2.12 shows a heart cut through the left ventricle and left atrium along the long axis of the heart approximately perpendicular to Figure 2.2.11.

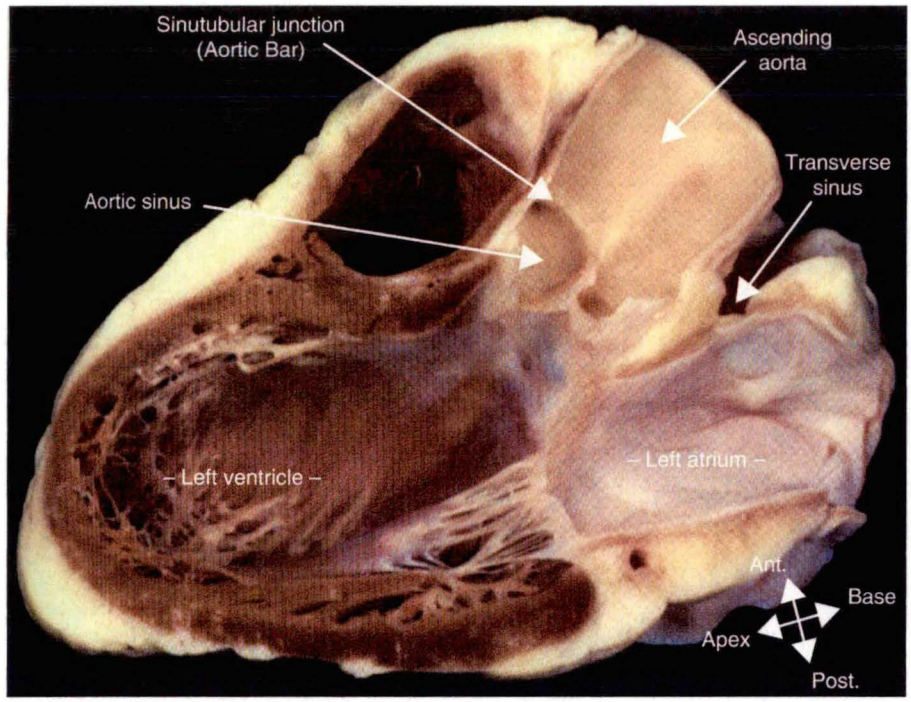

Figure 2.2.12: Long axis cut of the heart through the left atrium and ventricle. [82].

Figure 2.2.13 shows a dissection of the heart valve plane (perpendicular to the long axis of the heart). The valve plane separates the atria, aorta and pulmonary trunk from the ventricles. Note the aortic and pulmonary valves have three bucket leaflets, the mitral valve has two flat leaflets supported by cords and the tricuspid valve has three flat leaflets supported by cords.

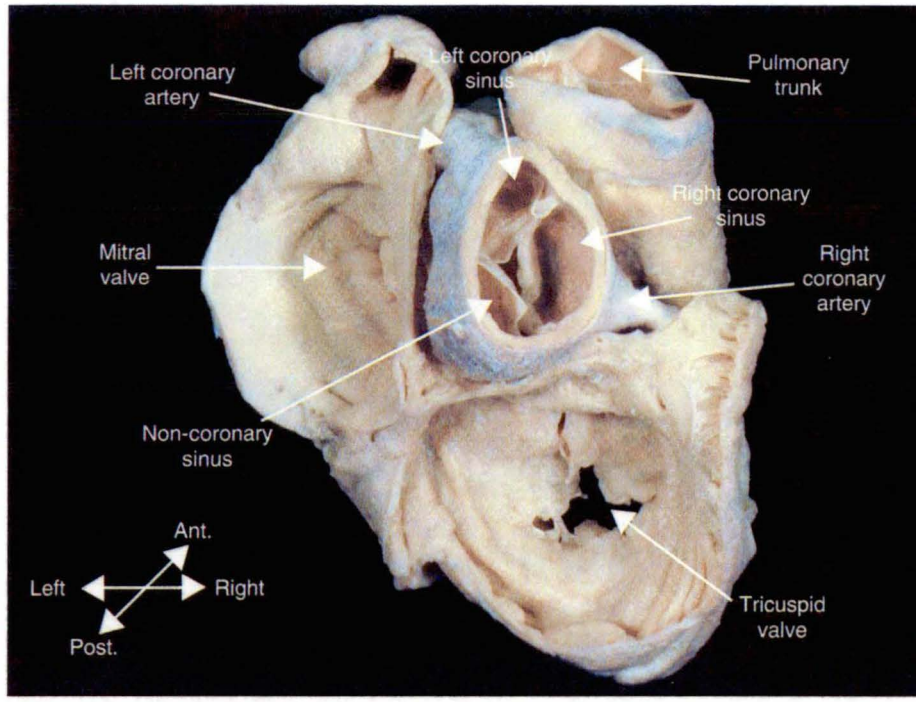

Figure 2.2.13: Dissection of the heart valve plane. [82].

Figure 2.2.14 shows a surgical view of the thin tricuspid valve from the right atrium side.

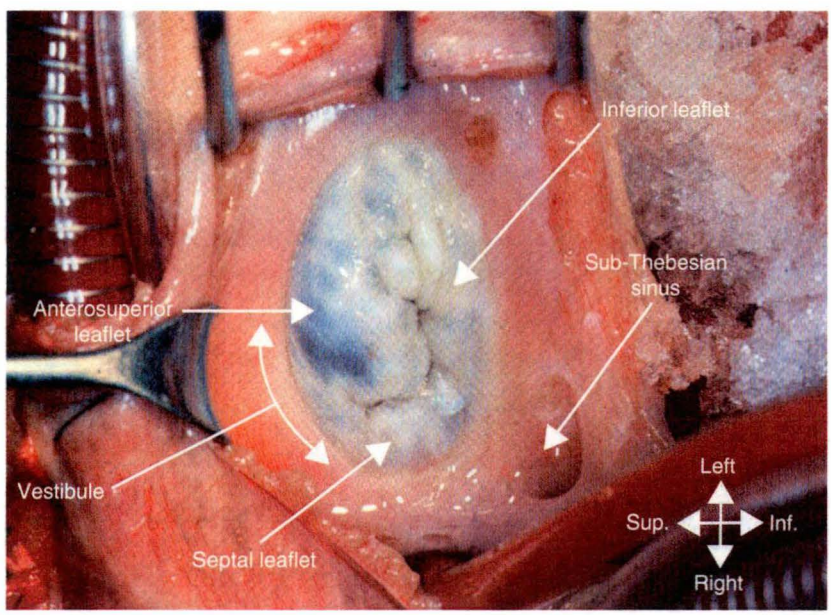

Figure 2.2.14: Surgical view of the tricuspid valve from the right atrium. [82].

A typical human heart measures 12-13cm from top to bottom, 7-8cm at its widest point and weighs 325 grams. The volumes of the four cardiac chambers are approximately: LA = 45ml, RA = 63ml, LV = 100ml, RV = 130ml. Typical length of the cardiac cycle is 750ms with 270ms systole (emptying of the ventricles) and 480ms diastole (filling the ventricles). Performance of the heart is given by the indices: heart rate in beats per minute (HR), stroke volume (SV), end diastolic volume (EDV), end systolic volume (ESV), ejection fraction and cardiac output (CO), where: SV = EDV – ESV and CO = HR × SV (assuming no valve leakage). EDV and ESV are different for each ventricle. Typical stroke volume is 70ml. Typical cardiac output is 5 l/min. Cardiac output increases during stress and exercise. Maximum heart rate is commonly estimated as (240 – age) bpm. EDV and EDS can increase and decrease respectively by about 50% to around 200ml and to around or less than 30-35ml respectively [85]. Respiration and posture have an effect on SV, CO, and HR. CO is 20% lower when standing than when lying down. HR is 5-10 beats per minute faster in erect than in supine and 10-28% greater when standing. CO also decreases with age [86]. Right ventricle stroke volume increases with inspiration (cyclic respiratory change = 20% p-p typical) while left ventricle stroke volume decreases (cyclic respiratory change = 20% p-p typical) and heart rate increases. The opposite changes occur with positive pressure ventilation.

2.3 Conductance catheter

The conductance catheter technique has been used to measure left and right ventricular volume. The technique has been applied in humans, sheep, dogs, pigs, rabbits and rats. The technique has also been used to determine atria volume and blood vessel volume (cross-sectional area). The technique exploits the contrast in electrical impedance between the blood and surrounding tissue.

The most commonly used technique uses an eight electrode catheter (with pigtail typically) placed in the left ventricle from the aorta as shown in Figure 2.3.1. Current is injected between an electrode near the apex and an electrode just outside the aortic valve. Electric potential differences are measured across $n-1$ segments between the n intermediate electrodes, where n is typically 6 but commonly varies between 3 and 6. Use of separate measurement and source electrodes eliminates artifacts due to polarisation and the effect of the local electric field of the source electrodes.

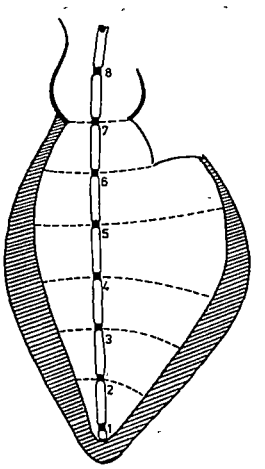

FIG 1 *Schematic representation of eight-electrode catheter placed along the long axis of the left ventricle. Dashed lines indicate equipotential surfaces defining blood segments.*

Figure 2.3.1: Conductance catheter in the left ventricle. [87].

Ventricle volume, V, is determined using the formula,

$$V(t)=\left(\frac{1}{\alpha}\right)\left(\frac{L^2}{\sigma_b}\right)\left(G(t)-G_p\right), \tag{2.3.1}$$

where: $G(t) = I\sum_{i=1}^{5}\frac{1}{E_t}$, σ_b = blood conductivity, L = electrode spacing, E_t = measured potential difference segment i, I = injected current, α = gain factor, G_p = parallel conductance.

The stroke volume is simply determined from the difference between end-diastolic and end-systolic volume.

Blood conductivity is most commonly determined using an external temperature regulated conductance cell with withdrawn blood. Calibrated impedance measurement using closely spaced electrodes on a customised catheter has also been used. Closely spaced electrodes reduce the effect of surrounding tissue on blood measurements.

Parallel conductance is sometimes not measured and is assumed zero. Using (2.3.1) parallel conductance cancels out when calculating stroke volume. The term accounts for current flow through tissue surrounding the blood volume being measured. The most commonly used method for determining parallel conductance involves an injection of saline. A small bolus of hypertonic saline is injected through a balloon floatation catheter in the pulmonary artery. The highly conductive saline transiently changes the conductivity of blood, practically without affecting parallel conductance. A plot of end diastolic G against end systolic G is made as the bolus passes through the left ventricle. The intersection of the line of best fit with the line: end diastolic G = end systolic G, gives the parallel conductance. This point represents the condition when the blood conductivity is zero and all current flows through the parallel conductance. Different frequencies give a different contrast between blood and tissue impedance, and this has also been used to determine a value for parallel conductance, however this approach is usually calibrated using the saline technique, and only accounts for dynamic changes in parallel conductance.

The gain factor in (2.3.1) is assumed one or is calculated by comparing the stroke volume predicted by (2.3.1) with another technique of stroke volume measurement such as angiography or thermodilution.

Typically an excitation current of around 30μA at 1-100kHz is used for measurements. This current is well below the value required to activate cardiac muscle. Continuous sinusoidal current is used and measurement voltages are filtered to remove cardiac (low frequency) and muscle activation artifacts. Conductance catheter systems are commercially available from a number of sources (e.g. CD Leycom/CardioDynamics BV, Inc., Zoetermeer, The Netherlands, and Millar Instruments, Inc., Houston, USA).

A dual field excitation configuration has been used to improve current density uniformity in the left ventricle [88]. The dual field excitation configuration uses an additional current source of opposite polarity and smaller magnitude placed outside each current source. This approach uses the same formula with the current as the sum of the two currents and a catheter with two more electrodes as shown in Figure 2.3.2. Typically four electrode miniature catheters, with only one segment are used in rats.

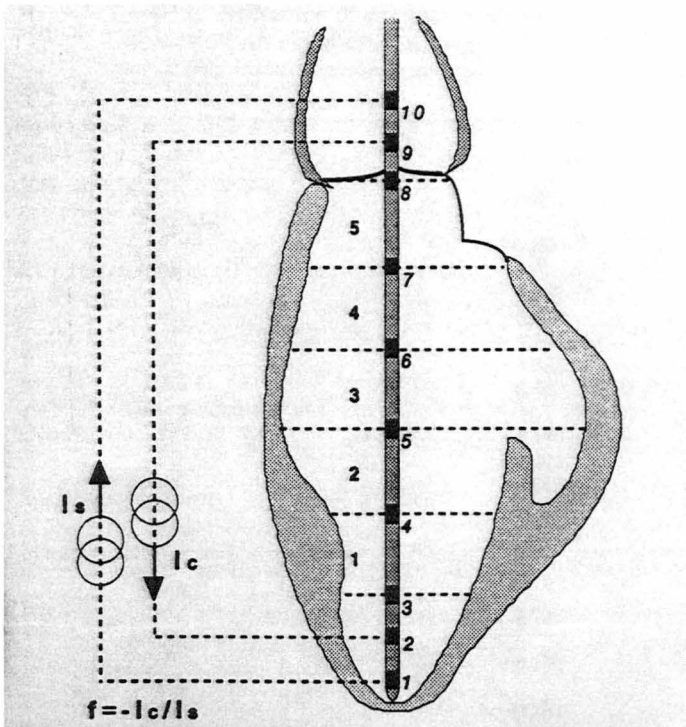

Fig. 1. Schematic representation of a conductance catheter positioned along long axis of left ventricle (LV). Conventional single-excitation field is generated by passing a current I_s via *electrodes 1* and *10*. Superposition of a 2nd current I_c via *electrodes 2* and *9* results in a "dual-excitation" field. Ratio of the 2 currents is $f = 0.3$. Dotted lines represent division of ventricle into 5 segments. Voltage over each segment is measured continuously and divided into total current to yield segmental conductances. Note that *1-10* and *2-9* currents are opposite in polarity.

Figure 2.3.2: Dual excitation conductance catheter in the left ventricle. [88].

Chapter 3. Literature Review

3.1 Introduction

The aim of this chapter is to assess different blood flow techniques for implantable use in humans (aim one of the thesis) and provide research data relevant to simulation of the conductance catheter (aim two of the thesis). The chapter will start by assessing a wide range of blood flow measurement techniques. Previous research in the area of conductance catheters will then be discussed (related to identifying major variables for aim 3 of the thesis and previous work in the area of aim four). Finally, topics important to the simulation of a conductance catheter will be discussed. Electrical properties of blood and tissue will be discussed followed by a discussion of heart anatomy and physiology research relevant to the thesis. Numerous raw figures and tables carefully selected from research literature are included in this chapter. Diagrammatic explanations have been included from other sources to more efficiently communicate the discussions for the reader. Raw tables have been included to eliminate any possibility of error or misinterpretation in reproduction. These have been referenced as required by copyright law (review and criticism purpose). Sufficient detail needed for good decisions is carefully included in the raw data for the curious reader, but the discussion is minimised to avoid over elaboration of detail.

3.2 Implantable Blood Flow Measurement Techniques for Humans

This section reviews current techniques for measuring blood flow in regard to measuring cardiac output with an implanted device. While blood flow is routinely obtained both in humans and animals using invasive nonimplantable sensors, the challenge is to develop reliable methods for implantable blood flow sensing in humans. Existing techniques, while effective in hospital or animal research settings, are generally undesirably invasive, making them unsuitable for use in humans.

Cardiac output (blood flow rate) was first measured in animals in the 1890's using a variety of indicator techniques. Cardiac output monitoring in humans originated in the 1940's with the advent of catheterisation. Flow measurements were obtained in animals in the 1960's using an implanted Doppler ultrasound device that transmitted flow signals to a nearby receiver [1]. Recently human implantable monitors, similar to pacemakers, have been developed that incorporate a mixed venous oxygen sensor [2]. These sensors are of limited use for blood flow monitoring since blood flow is also dependent on artery oxygen saturation and oxygen consumption.

Although a practical implantable blood flow sensor has not been developed, the technology for long term implantable monitors incorporating sensors on an attached catheter through the heart, is mature. Heart pacing devices are used routinely in humans. Implantable devices, similar to pacemakers, have been developed to continuously measure pulmonary artery and right ventricular pressures in humans. Catheter stabilization in the pulmonary artery was found to be a problem [3] and more recent devices [4] use a sensor fixed in the right ventricle to estimate pulmonary pressures. These devices are commercially available: Chronicle®, Medtronic, Inc., Minneapolis, USA. These devices use a titanium diaphragm and a polyurethane window to measure pressure [92].

Here we consider the specific advantages and disadvantages of various blood flow measurement techniques, including indicator methods and techniques to measure velocity and stroke volume. The intracardiac impedance method is considered in particular.

Blood Flow Measurement Techniques: Indicator Methods

Absolute flow has been determined from the change in concentration of an indicator in blood from either a steady state or transient injection of a measured quantity of indicator. These methods include Fick's method.

For steady state injection of indicator,

$$Q = \frac{dm/dt}{\Delta C}, \tag{3.2.1}$$

where: Q = flow, m = mass of indicator added, t = time, ΔC = concentration of indicator downstream of injection point – concentration of indicator upstream of injection point.

Fick observed in 1870 that (3.2.1) could be applied to oxygen transfer across the lungs. The method was not practical in humans until the 1940's, after the advent of cardiac catheterisation. Arterio-venous difference in oxygen concentration is obtained using central venous and arterial catheters. Venous oxygen concentration varies considerably. Central venous access provides a mixed estimate of venous oxygen concentration. Oxygen consumption is obtained by breathing through a flow-meter with oxygen sensor. Oxygen sensors have poor accuracy with high levels of inspired oxygen limiting the applicability of the method to certain patients [5].

Techniques using carbon dioxide transfer across the lungs instead of oxygen have been developed that do not require cardiac catheters. Recently, intermittent partial rebreathing has been used with a differential form of (3.2.1) to obtain semi-continuous cardiac output [5]. The technique still requires the patient to be under mechanical ventilation.

For transient injection of an indicator,

$$Q = \frac{m}{\int C(t)dt}, \tag{3.2.2}$$

where: Q = flow, m = mass of indicator added, t = time, $C(t)$ = concentration of indicator downstream of injection point – steady state concentration of indicator before injection. Methods employing (3.2.2) typically eliminate recirculation from the measured $C(t)$ using curve extrapolation before calculation.

The thermodilution technique, introduced in the 1970's, uses heat as the indicator in (3.2.2). Typically a small bolus of cold saline of known quantity and temperature is injected into the right atrium using a catheter. The cold saline mixes with the blood in the right ventricle. The temperature of the blood in the pulmonary artery is then measured using a thermistor mounted on a catheter. The technique can only be used intermittently due to the fluid loading it causes. More recently, semi-continuous thermodilution techniques have been developed where the blood is heated slightly with a heater rather than cooled with a bolus, preventing fluid overload [6]. These semi-continuous techniques typically suffer from lower signal to noise ratio.

Recently, a Lithium dilution technique has been developed that requires only a central venous catheter rather than the more invasive pulmonary artery catheter used in thermodilution [7]. Other indicators [8] that have been used in conjunction with (3.3.2) include dye (typically Indocyanine Green), saline with a different conductivity than blood, and radioactive substances.

Blood Flow Measurement Techniques: Velocity Measurement Techniques

Blood velocity has been measured with electromagnetic sensors, transit time ultrasound, Doppler ultrasound and laser Doppler systems. Less successful techniques include thermal transport (heat loss induced by flow), pressure gradient [9] and a bristle type meter (drag force induced by flow) [8].

Electromagnetic flow meters and transit time flow meters are commonly used in animal experiments. The sensors are incorporated into a unit that fits over a blood vessel. Due to the invasiveness of fitting the units over blood vessels, they are not used in humans.

Electromagnetic flow meters have been devised that setup a magnetic field perpendicular to the direction of blood flow in various ways [9]. As ions in the blood pass through this magnetic field they are acted upon by a force perpendicular to both the flow direction and the applied magnetic field. Electrodes measure the balancing electric potential. Mean flow velocity, V, is given by,

$$V = \frac{E}{Bd}, \tag{3.2.3}$$

where: E = measured potential between electrodes, d = electrode spacing, B = magnetic flux density.

Electromagnetic flow-meter techniques have overcome unstable voltages from electrode polarization and ECG interference by using a square or trapezoidal time-varying magnetic field. Induced EMF problems are associated with AC excitation. Coils used to create the field typically consume considerable power. In addition to external vessel units, catheter based electromagnetic flow-meters have been devised, but are highly sensitive to position.

Transit time flow-meters, using the difference between travel times of upstream and downstream ultrasonic waves transmitted between small piezoelectric transducers, have been constructed in various configurations [9]. Gel is used to ensure good signal conduction between external probes and tissue. Catheter mounted transit time devices have been constructed [91] but are highly sensitive to position. The mean flow velocity, V, is given by,

$$V = \frac{c^2 \Delta T}{2d \cos\theta}, \tag{3.2.4}$$

where: ΔT = difference between upstream and downstream travel times, c = speed of sound, d = travel distance of signal, θ = angle between flow direction and signal travel.

Phase detection rather than pulse timing, between upstream and downstream waveforms, is typically used to determine the typically extremely small time difference (of the order of 1 ns).

Pulsed Doppler systems, using frequency shifts in ultrasound signals scattered from red blood cells [10], offer the benefit of isolating velocity at different depths. Velocity, V, is given by,

$$V = \frac{c\Delta F}{2F \cos\theta}, \tag{3.2.5}$$

where: ΔF = frequency shift, c = speed of sound, F = signal frequency, θ = angle between flow direction and signal travel.

Continuous wave Doppler systems provide more extensive frequency information but cannot recover depth information. Modern ultrasound transducers use an array of piezoelectric crystals. Beam steering, by inserting time delay offsets between crystals in arrays, allows three-dimensional information to be recovered from a static probe. Handheld probes incorporating transducers are commonly used to measure blood flow in the ascending aorta. The probes are interfaced to the skin with gel to ensure good signal conduction. Recently, oesophageal Doppler, where a flexible probe is inserted orally into the oesophagus of an anaesthetized, mechanically ventilated patient, has been used to measure flow in the descending aorta [5]. More recently, intracardiac catheter mounted arrays have been used in the heart to aid heart surgery [11]. Doppler measurement is highly sensitive to probe positioning and signal processing can consume large amounts of power (especially for array transducers). Vessel wall motion artifacts can usually be removed successfully with a high pass filter.

Laser Doppler, using the frequency distribution of scattered light waves from red blood cells in flowing blood [12], is limited by laser penetration, on the order of only 1 mm, into blood and tissue. Laser Doppler has been used to determine blood perfusion in the microcirculation of tissues.

Blood Flow Measurement Techniques: Stroke Volume Measurement Techniques

Stroke volume methods are based on the difference between end-diastolic and end-systolic volume of a heart ventricle. Accuracy of these methods may be degraded if heart valve operation is abnormal. The left ventricle has a relatively simple geometry and methods have been developed, by using geometrical assumptions, to determine its volume relatively well from little dimensional information. However the right ventricle geometry is much more complex, and more data is needed to obtain its volume with the same accuracy. Various imaging techniques such as angiography, magnetic resonance imaging, CT and echocardiology have been used to obtain dimensional information for the determination of ventricular volume. However all these techniques are time consuming and manual digitization is needed to extract accurate dimensional information from the images. Other techniques used to obtain ventricular dimensions include intracardiac impedance, transcardiac conductance,

radionuclide ventriculography and sonomicrometry. Radionuclide ventriculography has poor accuracy and temporal resolution [13]. Sonomicrometry requires small ultrasonic piezoelectric transducers to be sewn onto the myocardium which is far too invasive for human use.

Intracardiac impedance has been used to assess the volume of the heart chambers. The technique exploits the contrast in impedance of blood and surrounding tissue. The technique involves measurements of electric potential from current source(s), using electrodes in the heart chambers.

Reference [14] describes the method most commonly used today for ventricular volume measurement using intracardiac impedance. The technique employs an eight electrode catheter that injects current (30 μA, 20 kHz) between an electrode near the apex and an electrode just outside the aortic valve of the left ventricle. Electric potential differences are measured across each segment between the six intermediate electrodes. The separation of measurement electrodes from source electrodes eliminates artifact due to polarization and the local electric field of source electrodes. Ventricular volume, V, is determined from these measurements using,

$$V(t)=\left(\frac{1}{\alpha}\right)\left(\frac{L^2}{\sigma_b}\right)\left(G(t)-G_p\right), \tag{3.2.6}$$

where: $G(t)=I\sum_{i=1}^{5}\frac{1}{E_i}$, σ_b = blood conductivity, L = electrode spacing, E_i = measured potential difference, I = injected current, G_p = parallel conductance, α = gain factor.

Parallel conductance is typically determined using a small bolus of hypertonic saline injected through a catheter [15]. The gain factor is calculated by comparing the stroke volume predicted by (3.2.6) with another technique of stroke volume measurement such as angiography or thermodilution.

A method for in vitro blood resistivity determination has been presented [16]. Formulae were provided to calculate blood resistivity from impedance between

closely spaced electrodes on two custom-made catheters positioned well away from heart tissue.

The intracardiac impedance technique has primarily been used in the left ventricle of animals. Current intracardiac impedance methods can give a reasonable relative volume measurement under certain conditions, however repeatability is poor and the relation to absolute volume is not well defined. The technique has been investigated for rate-adaption of pacemakers but it is not currently used [109-111].

A less invasive transcardiac conductance technique has been developed where current is applied between an electrode catheter in the superior vena cava and an external electrode. Potentials are measured from additional external electrodes [18]. The technique uses the same formula, (3.2.6), as the intracardiac impedance method.

Blood Flow Measurement Techniques: Other Methods

Other techniques developed to measure cardiac output include arterial pulse contour techniques and bioimpedance. The pulse contour method, using circulation models, is sensitive to compliance changes of vessels and needs to be regularly calibrated by another flow technique [5]. Bioimpedance, using impedance changes between upper and lower thorax (different principle from intracardiac impedance), while non-invasive has been reported to perform poorly [19].

Venous occlusion is used for regional flow assessment in humans [9]. Radioactive and dye microsphere indicators are used for regional blood flow evaluation in animal experiments [20]. Injected microspheres wedge in tissue and blood flow is determined from the concentration of microspheres in a volume of extracted tissue. Positron emission tomography, using radioactive tracers, is used to assess regional blood flow changes in neural science research [21].

Techniques for an Implantable Sensor

An implantable blood flow sensor must have characteristics that include small size, an output that is stable and reliable over extended periods (avoiding the need for recalibration), operation for extended periods using a small power source (besides other limitations, through-skin recharging is inconvenient for patients), avoidance of

left-side implantation (due to increased risk of stroke), minimal invasiveness and reasonable cost. Of great significance is the severe power limitation of the device, given the relatively large power requirements of some blood flow sensing methods.

Limited power eliminates the potential to use energy demanding, heater thermodilution techniques for regular flow. Implantable monitors cannot use indicator methods (except possibly for an indicator already in the blood) for measuring flow since indicator would have to be stored in the monitors. Velocity techniques are sensitive to position and blood flow distribution and these problems would have to be overcome for a reliable flow meter. Pulsed Doppler ultrasound from an array catheter could potentially be the best velocity technique in this regard, however signal processing requires bulky and power consuming electronics. In addition, for an array, a thin catheter may have to contain many transmission lines resistant to fatigue. The intracardiac impedance method in the right ventricle potentially provides very low power, continuous flow monitoring. However problems of sensitivity to parameters like blood and tissue impedance and catheter movement would have to be overcome. The right heart can significantly dilate in conditions such as advanced pulmonary hypertension and the algorithm used in such a case would have to be patient dependant. Valvular regurgitation or right heart failure could prevent the technique from providing an accurate flow assessment.

Conclusion

There is no single blood flow sensing technique that promises to be superior in every aspect for implantable use in humans. While ultrasound techniques hold significant potential, impedance electrode techniques may be preferred due to simplicity and low power requirements.

3.3 Conductance Catheter

The conductance catheter technique is a simple technique and research has not progressed much further than the commonly used method [14] discussed in Section 2.3. Most research literature simply repeats essentially the same experiment and adds negligible original work. Hundreds of papers have been published like this and there is little benefit in reviewing them all. Several authors have proposed methods to

improve the conductance catheter technique besides the use of an extra set of current source electrodes [88] to improve current uniformity in the left ventricle as discussed in Section 2.3. One author proposed a technique called field extrapolation to achieve a similar result [106-107]. Several authors have attempted to determine parallel conductance using frequency changes in myocardium conductivity instead of, or in conjunction with, the saline dilution method [93-97]. An alternative saline dilution method has been proposed, based on the integral of the conductivity change from saline injection; similar in concept to thermodilution but based on conservation of ions rather than conservation of energy. The method was demonstrated to be more accurate than the conventional technique but blood flow rate was needed in the calculation [98]. A method has also been proposed to correct for catheter curvature for a right ventricular catheter curved between tricuspid valve and pulmonary artery. The technique uses electrode spacing that is the projected distance between electrodes on the direct path between source electrodes. However the technique requires knowledge of the catheter curvature, or some way of calculating it [99]. The residual volume between source electrode at the apex of the left ventricle and the adjacent measuring electrode has been accounted for by multiplying the conductance in the next segment by 4/3 [15].

The effect of catheter position in the left ventricle has been assessed using a simplified model of the conductance catheter in the left ventricle. Typical error from off-center catheter was rated at 8-20% volume under estimation, with worst case 20-30% in systole and 35-40% in diastole [100]. Moving a catheter 5mm off-center in the left ventricle has been associated with approximately 5% volume under estimation [108]. The quality of conductance catheter signals from a wide range of catheter positions in the right ventricle has been assessed in animal experiments [17]. A free-breathing human right ventricular catheter study [101] indicated that "animal models where respiration is controlled by artificial ventilation thus give a false impression of the stability of data that can be obtained in the conscious human subject". The study reported "The effect of respiration on conductance derived volumes was variable and unpredictable, and this source of variability was minimised by selecting sections of data at held end expiration for all analyses". A three dimensional numerical model has been developed from MRI scans to simulate the conductance catheter in the ventricles [102]. The results aimed to investigate

error in saline dilution measurement of parallel conductance. The approach involved removal of surrounding tissue to estimate 'true' parallel conductance. However, true parallel conductance and gain are, by definition, essentially the coefficients of a linear equation fitting conductance catheter volume to real volume. They would therefore be better estimated by performing linear regression on the conductance measurements for a change in volume. This would give average coefficients over the change in volume. Determining the volume requires the numerical model to include the entire ventricle, including ventricle length changes.

3.4 Passive Electrical Properties of Blood and Tissue

In this section the bulk electrical properties of tissue and blood will be reviewed. The permeability of blood and tissue is equivalent to air, whereas dielectric properties, permittivity and conductivity, vary considerably and in complex ways. An excellent history and review of general dielectric properties of blood and tissue has been published [22]. Here multiple sources including such review articles will be integrated to provide the most appropriate property values for work in this thesis. The scope of this section will be limited to what is relevant to this thesis. The numerical modelling procedure used in Chapter 4 of this thesis allows specification of a single local material axis. Local bulk conductivity and permittivity tensors based on this single material axis can be defined. These tensors have the restriction that off-diagonal terms of the matrix are zero. Thus, in general, we can only model situations where the principal axes of these tensors match the local material axes.

Essentially all tissue except muscle can be approximated as being isotropic. Muscle is generally assumed to be isotropic perpendicular to fibre direction but different in the fibre direction. Cardiac muscle is often represented as a bidomain and care is taken here to present only bulk properties which are relevant for modelling passive electrical conduction.

There are several different terminologies used for stating dielectric properties in the literature. The most usual and most natural form is the conductivity and permittivity. Alternatively these properties can be stated in terms of complex impedance. Sometimes the resistivity, which is the inverse of conductivity, is stated. Some

tissues are electrically active, but at the low magnitudes of current and voltage in the application in this thesis only passive electrical properties are relevant (below stimulation threshold) and will be discussed here. The frequency dependency of conductivity and permittivity is governed by several dispersions (changes with frequency). At very low frequency around 100 Hz there is a very complex alpha dispersion below which permittivity is very high. In the high kilohertz/megahertz range, capacitive shorting of thin insulating cell membranes separating electrolyte compartments causes beta dispersion. Typically anisotropic properties become isotropic above this dispersion. Higher frequency dispersions are typically the result of relaxation effects (process limited in speed) at the macromolecule and water molecule level. In general, below the beta dispersion, cell death causes conductivity to increase (at constant temperature) and any anisotropy to decrease due to membrane failure. In general, little is known about the conductivity and variability of conductivity of living tissue, especially myocardium.

Electrical conductivity of blood and heart (myocardium) will be treated first followed by general tissue conductivity and permittivity. Detailed heart tissue fibre orientation will be discussed in Section 3.5.

Blood

Blood conductivity is a function of haematocrit (percentage of red blood cells by volume), temperature, velocity/shear rate (effect depends on many secondary variables including cell shape and frequency of shear rate), electrolyte/protein content and anticoagulant. Table 3.4.1 gives values for various combinations of variables.

Table 3.4.1: Conductivity of blood for different combinations of variables.

Ref.	σ (S/m)	F (Hz)	Source	T (°C)	Comments
[23]	.67	low	Human	37±.1	Haematocrit = 42% (normal), anticoagulant = ACD
[23]	.71	low	Human	37±.1	Haematocrit = 42% (normal), anticoagulant = SC
[23]	.67	low	Human	37±.1	Haematocrit = 42% (normal), anticoagulant = EDTA
[23]	.63	low	Human	37±.1	Haematocrit = 42% (normal), anticoagulant = SH
[23]	1.11	low	Human	37±.1	Haematocrit = 20%, anticoagulant = ACD
[23]	1.15	low	Human	37±.1	Haematocrit = 20%, anticoagulant = SC
[23]	1.17	low	Human	37±.1	Haematocrit = 20%, anticoagulant = EDTA
[23]	1.10	low	Human	37±.1	Haematocrit = 20%, anticoagulant = SH
[23]	.41	low	Human	37±.1	Haematocrit = 60%, anticoagulant = ACD
[23]	.44	low	Human	37±.1	Haematocrit = 60%, anticoagulant = SC
[23]	.40	low	Human	37±.1	Haematocrit = 60%, anticoagulant = EDTA
[23]	.37	low	Human	37±.1	Haematocrit = 60%, anticoagulant = SH
[24]	.338	1.6 k	Dog	25.0	Flow direction, steady flow, shear rate = low, 54%
[24]	.369	1.6 k	Dog	25.0	Flow direction, steady flow, shear rate = high, 54%
[24]	.330	1.6 k	Dog	25.0	Shear direction, steady flow, shear rate = low, 54%
[24]	.310	1.6 k	Dog	25.0	Shear direction, steady flow, shear rate = high, 54%
[24]	.348	1.6 k	Dog	25.0	Transverse direction, steady flow, shear rate = low, 54%
[24]	.366	1.6 k	Dog	25.0	Transverse direction, steady flow, shear rate = high, 54%
[25]	9%	10 k	-	22	Δσ p-p, sinusoidal flow, peak shear rate = 500 s^{-1}, 0.3 Hz, 35%
[25]	6%	10 k	-	22	Δσ p-p , sinusoidal flow, peak shear rate = 500 s^{-1}, 1 Hz, 35%
[25]	2.6%	10 k	-	22	Δσ p-p , sinusoidal flow, peak shear rate = 500 s^{-1}, 3 Hz, 35%
[25]	0.9%	10 k	-	22	Δσ p-p , sinusoidal flow, peak shear rate = 500 s^{-1}, 7 Hz, 35%
[26]	2%	low	-	-	%σ/°C, approximate temperature dependence
[27]	.51	100 k	Human	37	Normal adult, neonatal and placental blood, 42%
[27]	.74	-	Human	-	Reconstituted, time-expired bank blood, 42%
[27]	.81	25 k	Human	-	Haemodialysis patients, 42%

Blood conductivity is constant with frequency to several hundred kilohertz [28]. Further blood conductivity data and permittivity data is given under the section entitled General Tissue Conductivity and Permittivity.

Myocardium

Myocardium conductivity is a function of blood conductivity, cardiac phase, tissue ischemia/death, temperature and frequency. Table 3.4.2 gives bulk transverse and longitudinal values, or isotropic values for various combinations of variables.

Table 3.4.2: Myocardium conductivity for different combinations of variables. σ_l = conductivity in direction of muscle fibres, σ_t = conductivity in direction transverse to fibres. Numerical values of complex impedance are given in conductivity units.

Ref.	σ_l (S/m)	σ_t (S/m)	F (Hz)	Source	T (°C)	Comments
[29]	.317	.202	5 k	Dog	37	average over cardiac cycle, in vivo
[29]	.339	.211	10 k	Dog	37	average over cardiac cycle, in vivo
[29]	.356	.217	15 k	Dog	37	average over cardiac cycle, in vivo
[29]	.369	.223	20 k	Dog	37	average over cardiac cycle, in vivo
[29]	.395	.234	30 k	Dog	37	average over cardiac cycle, in vivo
[29]	.416	.242	40 k	Dog	37	average over cardiac cycle, in vivo
[29]	.438	.250	50 k	Dog	37	average over cardiac cycle, in vivo
[29]	.457	.248	60 k	Dog	37	average over cardiac cycle, in vivo
[29]	16%	10%	5 k	Dog	37	Standard deviation 4 dogs, in vivo
[29]	5%	3%	5 k	Dog	37	$\Delta\sigma$ p-p over cardiac cycle, in vivo
[30]	3%	$=\sigma_l$	5-60k	Dog	37	$\Delta\sigma$ peak, transient increase in blood σ, in vivo
[31]	.65	$=\sigma_l$	1 k	Sheep	37	normal, in vivo
[31]	.22	$=\sigma_l$	1 k	Sheep	37	60 min. after infarct, in vivo
[31]	1.11	$=\sigma_l$	1 k	Sheep	37	1 week after infarct, in vivo
[31]	.98	$=\sigma_l$	1 k	Sheep	37	2 weeks after infarct, in vivo
[31]	1.35	$=\sigma_l$	1 k	Sheep	37	6 weeks after infarct, in vivo
[32]	.14	$=\sigma_l$	1 k	Dog	35	40 min. of ischemia, freshly excised, σ=1/Re(Z)
[32]	.15	$=\sigma_l$	10 k	Dog	35	40 min. of ischemia, freshly excised, σ=1/Re(Z)
[32]	.22	$=\sigma_l$	100 k	Dog	35	40 min. of ischemia, freshly excised, σ=1/Re(Z)
[32]	-4.44	$=\sigma_l$	1 k	Dog	35	40 min. of ischemia, freshly excised, σ=1/Im(Z)
[32]	-1.31	$=\sigma_l$	10 k	Dog	35	40 min. of ischemia, freshly excised, σ=1/Im(Z)
[32]	-.69	$=\sigma_l$	100 k	Dog	35	40 min. of ischemia, freshly excised, σ=1/Im(Z)
[32]	.06	$=\sigma_l$	1 k	Dog	35	90 min. of ischemia, freshly excised, σ=1/Re(Z)
[32]	.10	$=\sigma_l$	10 k	Dog	35	90 min. of ischemia, freshly excised, σ=1/Re(Z)
[32]	.20	$=\sigma_l$	100 k	Dog	35	90 min. of ischemia, freshly excised, σ=1/Re(Z)
[32]	-.42	$=\sigma_l$	1 k	Dog	35	90 min. of ischemia, freshly excised, σ=1/Im(Z)
[32]	-.25	$=\sigma_l$	10 k	Dog	35	90 min. of ischemia, freshly excised, σ=1/Im(Z)
[32]	-.37	$=\sigma_l$	100 k	Dog	35	90 min. of ischemia, freshly excised, σ=1/Im(Z)

General Tissue Conductivity and Permittivity

Table 3.4.3 and Table 3.4.4 are extensive tables of conductivity and permittivity values respectively for a wide variety of tissues including fat, liver, lung and bone. The effect of permittivity is considered as negligible in this thesis. Other reviews of multiple tissues have been compiled [33-38]. Other detailed studies of single tissues have been compiled for instance for blood [39,40] and skeletal muscle [41].

Table 3.4.3: Conductivity data for a wide variety of tissues. [22].

		Conductivity (S/m)										
	Frequency	A Skeletal muscle parallel (nonoriented)	B Skeletal muscle perpendicular (nonoriented)	C Liver	D Lung	E Spleen	F Kidney	G Brain white matter	H Brain gray matter	I Bone	J Whole blood	K Fat
1	10 Hz	0.52	0.076	0.12	0.089							
4	100 Hz	0.52	0.076	0.13	0.092					0.0126	0.60	
7	1 kHz	0.52	0.08	0 13	0.096					0.0129		0.02—0.07
8											0.68	
10	10 kHz	0.55	0.085	0.15	0.11					0.0133		
11						0.24 ± 0.03					0.68	
12				0.14		0.10	0.073					
13	100 kHz	0.65	0.40	0.15		0.62	0.24—0.25	0.12—0.15	0.17	0.0144	0.55	
14			0.56—0.59	0.16							0.68	
15			0.38—0.44	0.18		0.15	0.14					
16	1 MHz			0.27		0.63	0.37—0.39	0.14—0.19	0.21	0.0173		
17			0.83—0.85	0.30							0.71	
18			0.58—0.63	0.27		0.24	0.25					
19	10 MHz		0.86—0.87	0.47		0.84	0.64—0.68	0.21—0.28	0.35	0.0237		
20			0.92—0.96	0.46		0.55—0.53	0 50—0.57	0.30	0.38		1.11	
21			0.69—0.75	0 42—0.46		0.41	0.46	0.29—0.31	0.45—0.63			
22	100 MHz		0.95—0.99	0.72		1.05	0.94—1.05	0.36—0.48	0.69	0.0574	1.0	0.02—0.07
23			0.9 ± 0.08	0.70	0.53	0.73—0.76	0.66—0.72	0.45	0.7			
24			0.75—0.82	0.60—0.71		0.80 ± 0.02	0.75 ± 0.02	0.48—0.51	0.52—0.85		0.7—0.8	
25	1 GHz		1.38—1.45	0.98		1.2		0.89—0.94		0.05	1.4—1.6	
26			1.3	1.2	0.73	1.09—1.13	0.95—0.97	0.80	1.1		1.3	0.03—0.09
27			1.5	0.95—1.0		2.0	1.0	0.81—0.82	0.89—1.17			
28	3 GHz			2.0		2.5 ± 0.03		1.8—2.1		0.16	2 5—3.1	
29			2.7 ± 0.07	2.4				1.5	2.0			
30			2.8	2.8		2.7	2.3 ± 0.05					
31	10 GHz		8.3	5 8—6.7		6.5				0.5—1.7	9 1	0.3—0.4
32			7.7	10.0					10		10.5	
33			8.8			10.0	4 5—7.4	8				
34	35 GHz	39.9 ± 3.5					28.0 ± 2.5	38.9 ± 1.6		49.8 ± 0.4	2.7 — 0.8	

Table 3.4.4: Relative Permittivity data for a wide variety of tissues. [22].

	Relative Permittivity											
	Frequency	A Skeletal muscle parallel (nonoriented)	B Skeletal muscle perpendicular (nonoriented)	C Liver	D Lung	E Spleen	F Kidney	G Brain white matter	H Brain gray matter	I Bone	J Whole blood	K Fat
1	10 Hz	10^7	10^6	5×10^7	2.5×10^7							
4	100 Hz	1.1×10^6	3.2×10^5	8.5×10^5	4.5×10^5					3800		1.5×10^5
7	1 kHz	2.2×10^5	1.2×10^5	1.3×10^5	8.5×10^4					1000		5×104
8											2900	
10	10 kHz	8×10^4	7×10^4	5.5×10^4	2.5×10^5					640		2×10^4
11						1.4×10^4						
12				1.8×10^4		3.4×10^4	4.8×10^4				2810	
13	100 kHz	1.5×10^4	3×10^4	9760		3260	1.09×10^4—1.25×10^4	1960—3400	3800	280	4000	
14			2.5×10^4—2.7×10^4	1.4×10^4							2740	
15			1.4—1.6×10^4	6700		6300	8300					
16	1 MHz			1970		1450	2390—2690	543—827	1250	87		
17			2460—2530	1970							2040	
18			1900—2150	1000		1300	1500					
19	10 MHz		170—190	338		321	431—499	163—209	352	37		
20			187—204	300		352—410	190—204	200	380		200	
21			162—181	251—265		300	308	190—191	237—289			
22	100 MHz		67—72	77		83	89—95	57—66	90	23		4.5—7.5
23			68 ± 2	79	35	71—76	56—62	65	90		67	
24			64—70	65—68		81 ± 3	85 ± 1	58—64	65—80		72—74	
25	1 GHz		57—59	46		54		40—44		8	58—62	4.3—7.5
26			58	55	35	50—51	43	5	45		63—67	3—6
27			48	47—49		50	46	38—39	47—51		63	
28	3 GHz			42		52 ± 0.6		35—41		7.5	55—56	4—7
29			52.5 ± 0.7	53				33	44			
30			46	42—43		46	47.5 ± 1					
31	10 GHz		40—42	34—38		42			8	50—52	3.5—4.0	
32			37	37				25	40		45	
33			35			38	38—37					
34	35 GHz		19.1 ± 1.5					17.8 ± 1.7	21.3 ± 0.9		23.6 ± 0.3	3.6 ± 0.3

3.5 Heart Anatomy and Physiology

This section will focus on humans with and without pulmonary hypertension. The section will start with a discussion of myocardium fibre orientation, fat distribution and respiration. Finally blood flow and more general relevant anatomy and physiology will be presented. This section, together with Section 3.4 is the most critical in the entire literature review. The typical investigator may totally neglect such content, making ad hoc assumptions, with no one questioning such an approach or actually praising it. All methods in the investigation chapters of this thesis are based on numerical modelling. Knowledge of variables and their variability between patients is crucial if numerical modelling is based on imaging of a limited patient population under limited conditions. It allows assumptions used in numerical modelling to be objectively assessed, as little information is generally included in models, due to lack of readily available information on relevant aspects of heart anatomy and physiology. An investigation into a small aspect involves many years of research. More questions are raised in this section than are answered in this thesis. The importance of this data to the thesis and the complexity in conveying the information warrant the length of this section. The approach used in this thesis is therefore significantly different from previous conductance catheter techniques.

Myocardium Fibre Orientation

Fibre orientation effects both how the heart pumps blood and how electric current interacts within the thorax. Figure 3.5.1 shows the general muscular structure of the heart. The fibre direction is relatively uniform across the heart, but varies significantly with depth. The ventricle muscle longitudinal direction is circumferential in the short axis plane at approximately halfway between endocardium and epicardium. The angle of fibres increases relative to the short axis plane to become around 60-90 (90 degrees at the trabeculation) degrees at the epicardium and endocardium. The direction towards the endocardium is in a left to right direction from the apex to the base, whereas the direction towards the epicardium is in a right to left direction from apex to base. The fibre angle from histological dissections of dogs is shown in Figures 3.5.2. Such findings are in accordance with diffusion tensor MRI studies, Figure 3.5.3. The fibres of the heart muscle have been found to be arranged in sheets 4-6 cells thick, separated by

collagen matrix as shown in Figure 3.5.4. The normal angles of these sheets can also be measured using the above techniques as shown in Figure 3.5.5. Therefore properties of heart tissue are expected to be different in three mutually orthogonal rather than the two transverse directions orthogonal to the fibre direction being equal. To the best of my knowledge the inter-animal and inter-species variability of the fibre direction has not been assessed in detail as yet.

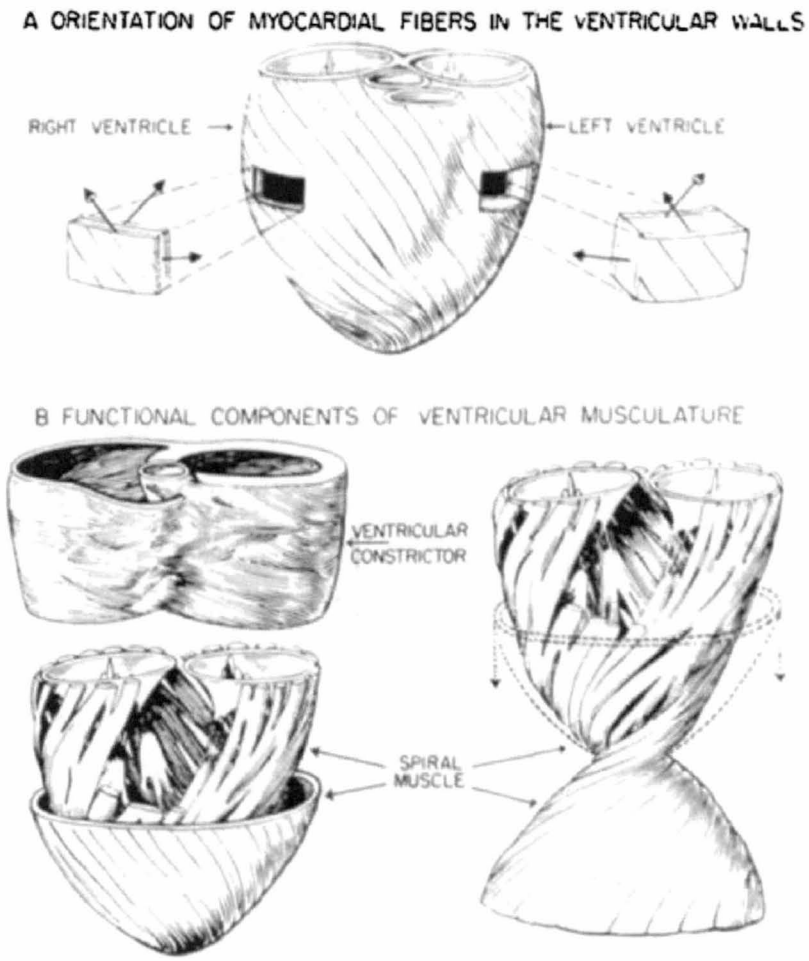

Figure 3.5.1: Muscle architecture of the heart. [42].

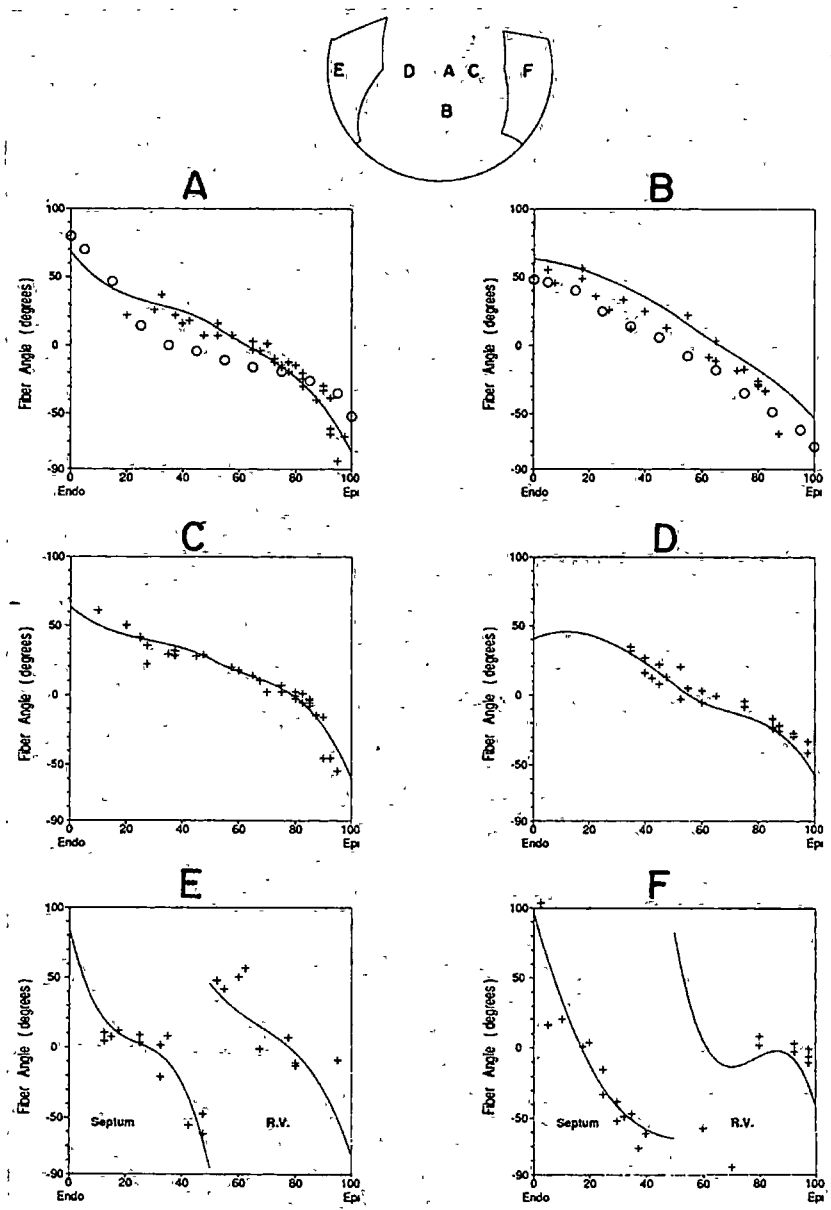

FIG. 12. Transmural distributions of myocardial fiber orientation as function of normalized wall thickness. Each graph shows fitted fiber orientation (continuous line) and measured fiber angles through the wall. Epicardial locations of sites *A–F* are shown at *top*. *E* and *F* show distributions through right ventricular free wall and septum. Discontinuity at 50% wall thickness is due to separation of adjacent elements by right ventricular lumen. Circles plotted on *A* and *B* represent comparable data from Streeter et al. (29).

Figure 3.5.2: Transmural distribution of fibre orientation from histological studies. [43].

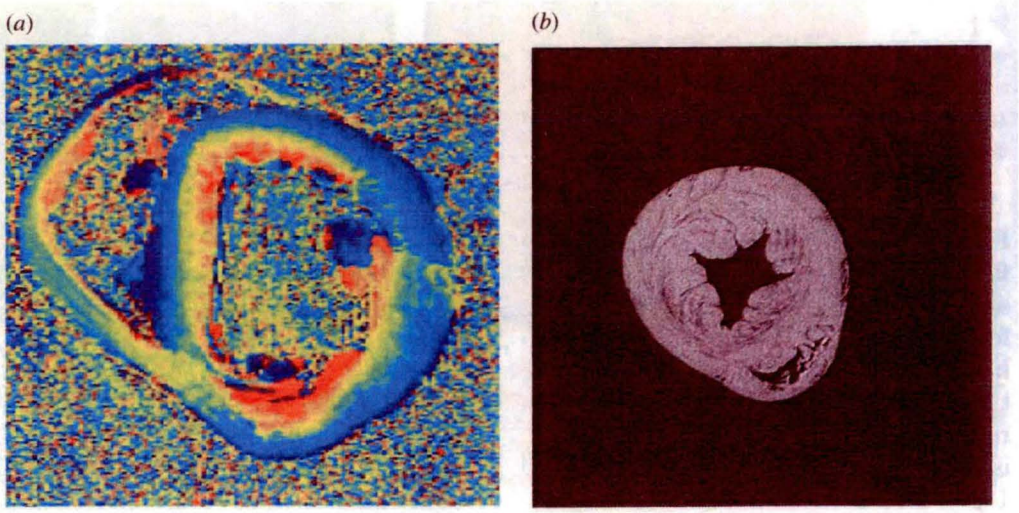

Figure 8. (*a*) A colour map representing the fibre angle in the myocardium as determined from high-resolution 3D diffusion tensor imaging with fast spin-echo. The blue represents a fibre angle of $-60°$ off the circumferential and red a $90°$ angle. The transmural gradient in fibre angle is clearly seen. (Data courtesy of David Scollan and Rai Winslow.) (*b*) A single slice from a high-resolution 3D T1 weighted image of a dog heart *in vitro*. Fine vascular and fibre structures are visible.

Figure 3.5.3: Fibre direction from diffusion tensor MRI. [44].

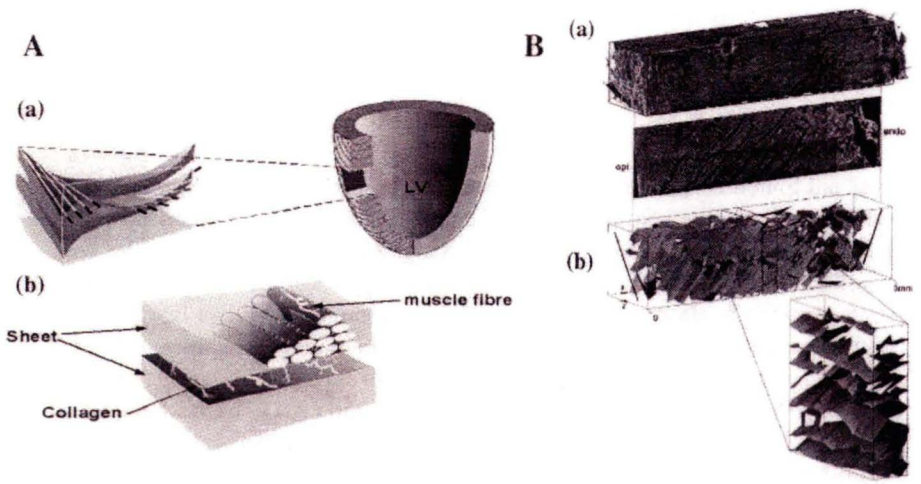

Figure 2 (*A*) Schematic showing (*a*) the variation in muscle fiber direction across the wall in a segment removed from the left ventricle, and (*b*) the branching laminar structure of myocardium in which the sheets are composed of myocytes bound in layers, 3–4-cells thick, by endomysial collagen and surrounded by perimysial collagen, which also links to the adjacent sheet. This "fibrous-sheet" architecture allows for shearing to occur between the layers and aids the process of wall thickening at end-systole. (*B*) (*a*) A composite 3-D confocal image of a transmural block of myocardial tissue from the rat heart with a single image slice shown below; (*b*) a finite element model of the cleavage planes from the transmural tissue block used to study the flow of current and propagation of the tissue activation wave front around the myocardial sheet structures. The spatial variation of tissue properties, such as the density of collagen, gap junctions, and ion channels, is defined by the markup language FieldML (http://www.bioeng.auckland.ac.nz/physiome/physiome.php). Note: *A* and *B* from Hooks et al. (75) by permission.

Fig 3.5.4: Fibres arranged in sheets separated by collagen. [45].

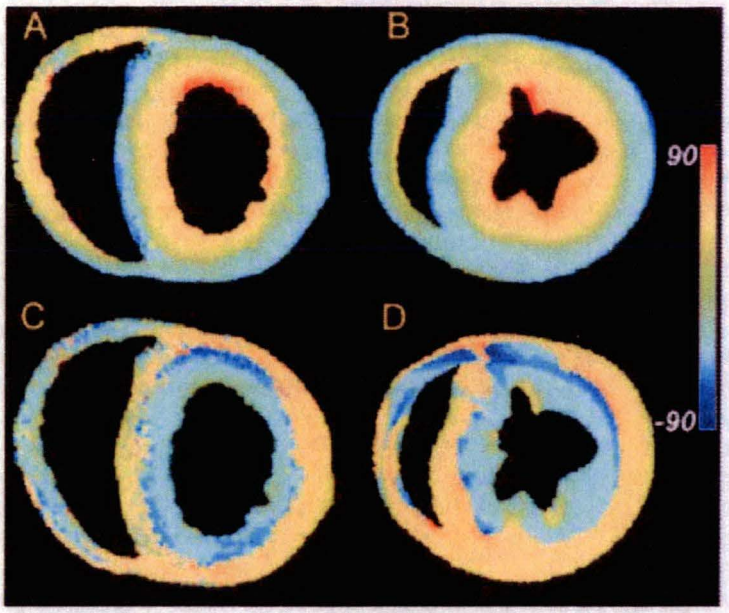

Figure 10 (*A*) Map of primary eigenvector inclination angle obtained from DTMRI for one slice in a fixed rabbit heart. (*B*) Fiber inclination angle map obtained from the histological reconstruction of Nielsen et al (77) for one section of a dog heart. (*C*) Map of tertiary eigenvector inclination angle obtained from DTMRI for the same slice as in A. (*D*) Map of the inclination angles of the laminae normals obtained from the Nielsen et al reconstruction for the same slice as in B.

Figure 3.5.5. Fibre direction (top) and fibre sheet direction (bottom) from diffusion tensor MRI (left) and histological studies (right). [46].

Fat Distribution

As well as affecting the dynamics of the heart, fat (or more precisely adipose tissue) surrounding the heart affects how electric current interacts between heart and thorax. We are specifically interested in the distribution and variability of the distribution between subjects. There are three main types of fat considered here, epicardial (attached to surface of the heart), intramyocardial (infiltrating myocardium) and pericardial.

Figure 3.5.6 shows the epicardial fat distribution across the normal right ventricle. The measurements are the mean epicardial fat thickness in mm at the ten different sites from a study of 200 autopsy patients, mostly males over the age of 40. Epicardial fat spreads inwards from the base of the heart and the coronary artery/sinus areas. There is decreasing level of fat from base to apex, relatively thick fat on the anterior wall of the right ventricle and relatively non-existent fat on the diaphragmatic/posterior surface of the ventricle. Table 3.5.1 gives the corresponding standard deviation and variance at the ten sites on Figure 3.5.6. Significant variability between patients is indicated. The thickness distribution of the 2000 (200×10) measurements taken is shown in Figure 3.5.7. Figure 3.5.8 shows findings from a different study at position equivalent to 5 and 8 in Figure 3.5.6. A significant increase in fat with age is shown but other studies don't support this [89] The epicardial fat in women has been found to be significantly greater than that in men, in those aged over 20 [48]. Patients with hypertrophied hearts have been found to have more epicardial fat, however the ratio of fat to myocardial mass in each ventricle has been found to be relatively constant even in hypertrophied hearts [89]. The amount of epicardial fat seems to be more related to the amount of visceral fat than total fat [89]. Little has been published on the distribution of fat on the left ventricle [90], however it has been reported to be about one third of the right ventricle per gram of myocardium [89].

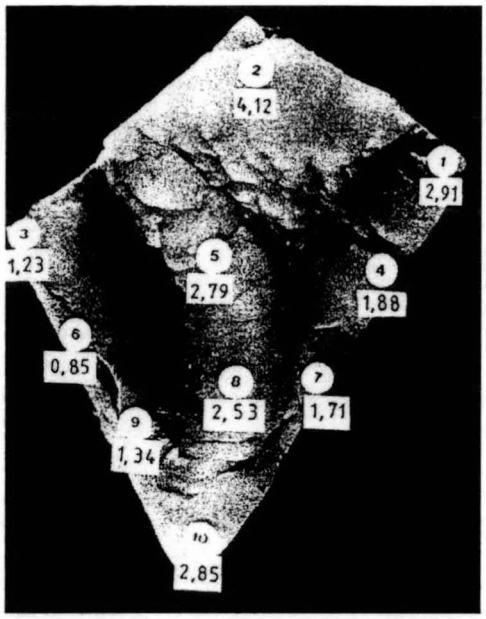

Figure 3.5.6: Typical epicardial fat distribution over the right ventricle free wall. Base (top), apex (bottom), surface adjacent liver (left), surface adjacent sternum (right), pulmonary artery (top right). Measurements are mean thickness in mm. [47].

Table 3.5.1: Mean ($\bar{x}$), and standard deviation (s) of epicardial fat thickness (mm) at the sites (1-10) marked in Figure 3.5.6. [47].

Tab. 2 Durchschnittswerte der epikardialen Fettschichthöhe an den 10 Standardmeßstellen, berechnet von je 200 Einzelwerten

Meßstelle	$\bar{x}$	s	s^2
1	2,913	2,498	6,242
2	4,12	2,598	6,751
3	1,234	1,668	2,783
4	1,882	1,518	2,305
5	2,788	2,069	4,279
6	0,851	1,393	1,94
7	1,71	1,44	2,073
8	2,529	2,006	4,025
9	1,34	1,838	3,38
10	2,852	2,058	4,236

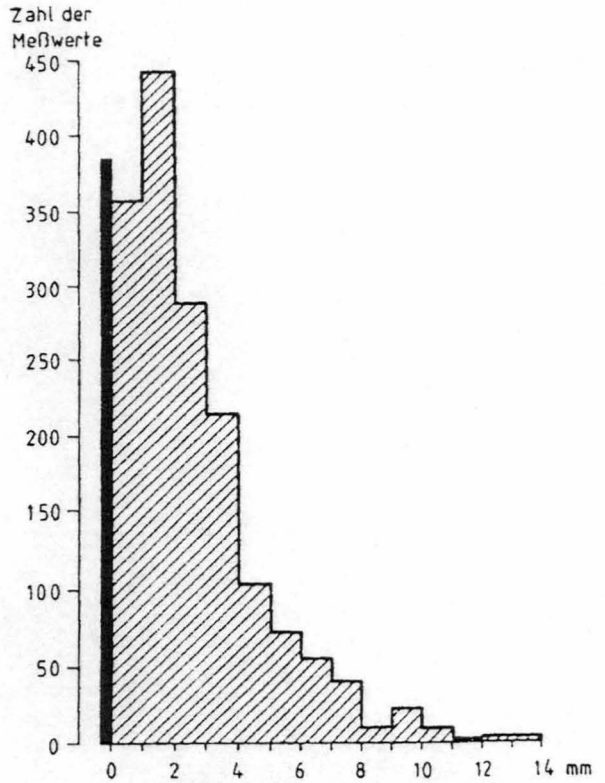

Abb. 4 Höhe des epikardialen Fettgewebes: Verteilung der 2.000 Einzelwerte von 200 Obduktionsherzen, abgerundet auf ganze Millimeterwerte.

Figure 3.5.7: Thickness distribution showing number of measurements from all ten measurement sites within a certain mm out of a total of 2000 measurements. [47].

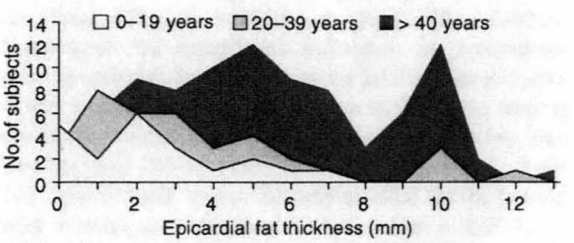

Figure 2. Thickness of epicardial fat in lateral right ventricle wall by age. The amount of epicardial fat in the right ventricle increased with age. Infants had little or no epicardial fat; the greatest amount of fat was seen in subjects over 40 years of age.

Figure 3.5.8: Epicardial fat thickness with age. [48].

The border between epicardial fat and myocardium can be well defined or ill-defined. Ill-defined borders are usually associated with intramyocardial fat. In most cases intramyocardial fat is located in the outer one half of the myocardium. It's distribution is similar to the epicardial fat distribution [48]. Figure 3.5.9 shows the

proportion of right ventricle myocardium that is fat in the normal heart. There is a significant increase with age and in females aged over 40 [48].

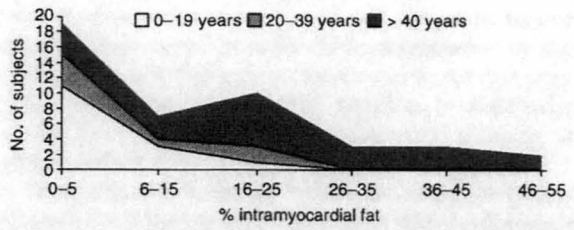

Figure 6. Males: % intramyocardial fat in lateral right ventricle wall by age. In male subjects the amount of intramyocardial fat in the lateral right ventricle increased with age, with the largest amounts of intramyocardial fat seen in the over 40s.

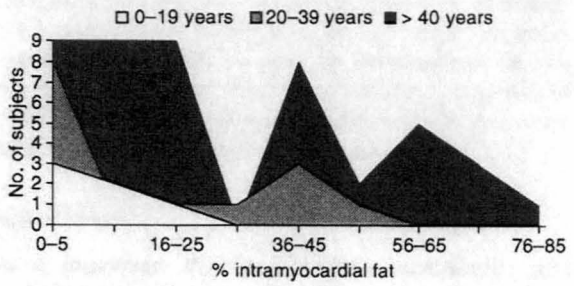

Figure 7. Females: % intramyocardial fat in lateral right ventricle wall by age. Female subjects generally had more intramyocardial fat than males. The amount of fat in the lateral right ventricle wall increased with age; in one-third of females over 40 years of age over 50% of the lateral wall was replaced by fat.

Figure 3.5.9: Percentage of myocardium that is intramyocardial fat. Males (top) and females (bottom). [48].

The inner surface of the parietal pericardium has no fat and is in direct contact with the heart, however fat exists on the epipericardium. Epipericardial fat is usually most prominent adjacent the right ventricular free wall [49]. The amount of epipericardial fat varies significantly between subjects, approximately half with an insignificant quantity. A collection of epipericardial fat typically exists around the anteroinferior portion of the heart pericardium [50]. Presence of epipericardial and epicardial fat allow identification of the pericardium on CT and MRI scans over the right ventricle [51]. There is typically little fat between base of the pericardium and liver. The anterior surfaces of the lungs are in direct contact with the chest wall, with no fat in between [50]. However they may be restricted from extending around the anterior of the heart by epicardial fat.

Respiration

As well as translating, the heart undergoes deformation and rotation due to respiration [52-58] that is unrelated to respiratory changes in stroke volume. (Mechanical attachment of the pericardium and heart in humans and stroke volume changes were discussed in Section 2.2). Studies have shown significant inter-subject variation in heart deformation due to respiration. Typical values for heart landmark movement between deep inspiration and expiration are shown in Table 3.5.2. The approximately linear proportionality between diaphragm movement and the landmarks is given in Table 3.5.3. The largest movement is in the inferior direction with increasing inspiration. As can be seen, inferior points move a greater amount than superior points of the heart.

Table 3.5.2: Heart landmark movement with respiration. [52].

Table 1
SI Displacements Compared with AP Displacements

Anatomic Landmark	Coordinate Type	Range (mm)	SI/AP Range Ratio
Heart	SI (inferior margin)	18.1 ± 9.1	10.3 ± 9.1
	AP (anterior margin)	2.4 ± 1.5	
Apex	SI	16.0 ± 7.1	10.6 ± 7.7
	AP	3.0 ± 2.8	
RCA root	SI	10 5 ± 4.8	6.2 ± 3.6
	AP	2 3 ± 1.4	
LAD	SI	13.1 ± 4.1	8.2 ± 4.1
	AP	2.0 ± 0.7	

Motion range is taken to be the range of the measured coordinates. (Notation. mean ± standard deviation over 10 subjects.)

Table 3.5.3: Relation between landmark movement and diaphragm movement. [52].

Table 2
Linear Regression with Respect to the SI Position of the Diaphragm

Anatomic Landmark	Regression Slope *k*	Correlation Coefficient *r*
Cardiac superior margin (1,5)	0.62 ± 0.19	0.96 ± 0.04
Cardiac inferior margin (1,5)	0.92 ± 0 21	0.98 ± 0.01
RCA root (1,5)	0.57 ± 0 26	0.97 ± 0.03
Apex (2,6)	0.81 ± 0 23	0.97 ± 0.02
LAD (2,6)	0.70 ± 0.18	0.98 ± 0 02

(Notation: mean ± standard deviation over 10 subjects; the numbers in parenthesis in the first column reference to figures)

Mechanical ventilation and posture have been found to significantly affect diaphragm and rib motion [104]. Posture also affects static diaphragm position. These variables would therefore be expected to cause deformation of the heart.

Blood Flow

The main cardiac performance indices (cardiac output, stroke volume, heart rate and ejection fraction) give little information about the temporal dynamics and distribution of blood flow around the heart. In this section, results from MRI phase velocity imaging studies are presented to give greater insight into blood flow around the heart. This technique is often used to validate heart fluid dynamics modelling [59]. MRI velocity provides accurate flow integrals [60, 61].

Figure 3.5.10 shows the flow curves (integrated from MRI velocity normal to planes) for various vessels close to the heart. The data is from a normal person at rest and during upright cycling exercise. The heart rate increased by 54% between rest and exercise. Note the more steady flow in the inferior (E) and superior (D) vena-cava compared to the main (A), left (C) and right (B) pulmonary artery.

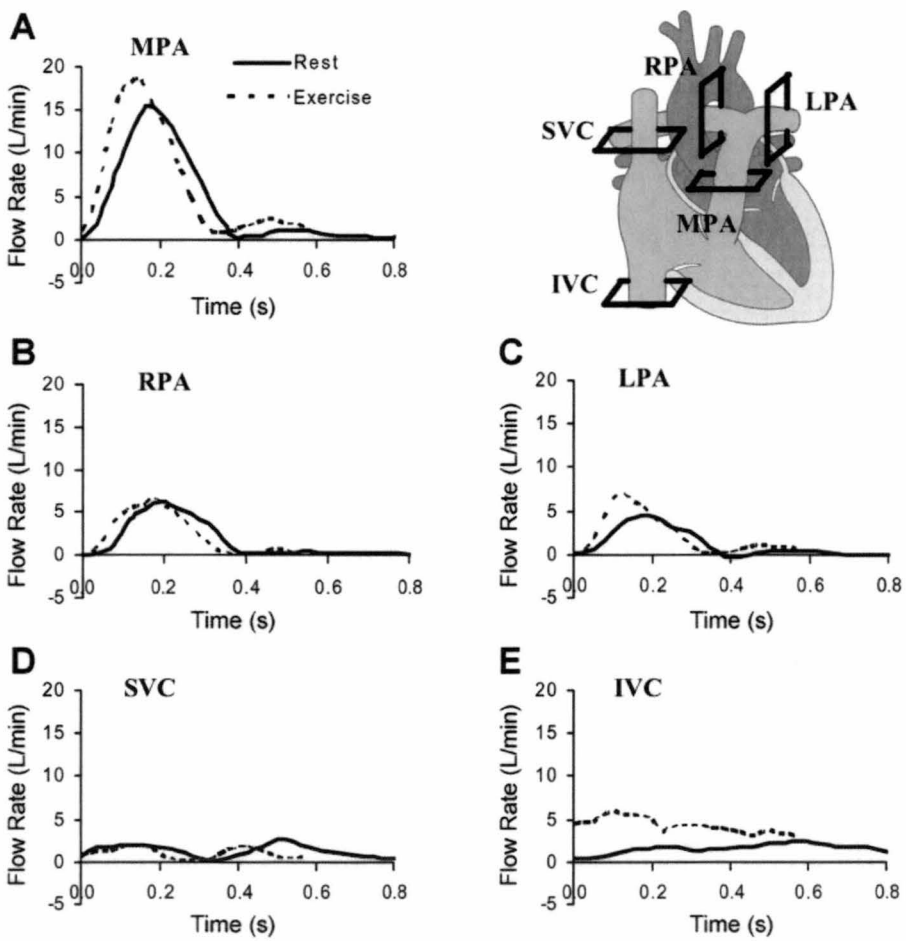

Figure 3.5.10: Pulmonary and Cava Flow in Normal Person. [62].

In Pulmonary hypertension there is a significant change in the flow curves in the pulmonary artery. Figure 3.5.11 separates forward flow from reverse flow, forward flow and net forward flow (forward flow minus reverse flow). As can be seen there is negligible reverse flow (mainly around the time 400ms at pulmonary valve closure) in normal patients (A) but significant reverse flow in pulmonary hypertension (B). The reverse flow is suggestive of strong velocity profile differences across the pulmonary artery, in the case of pulmonary hypertension. This reverse flow results in a double peak waveform of net flow.

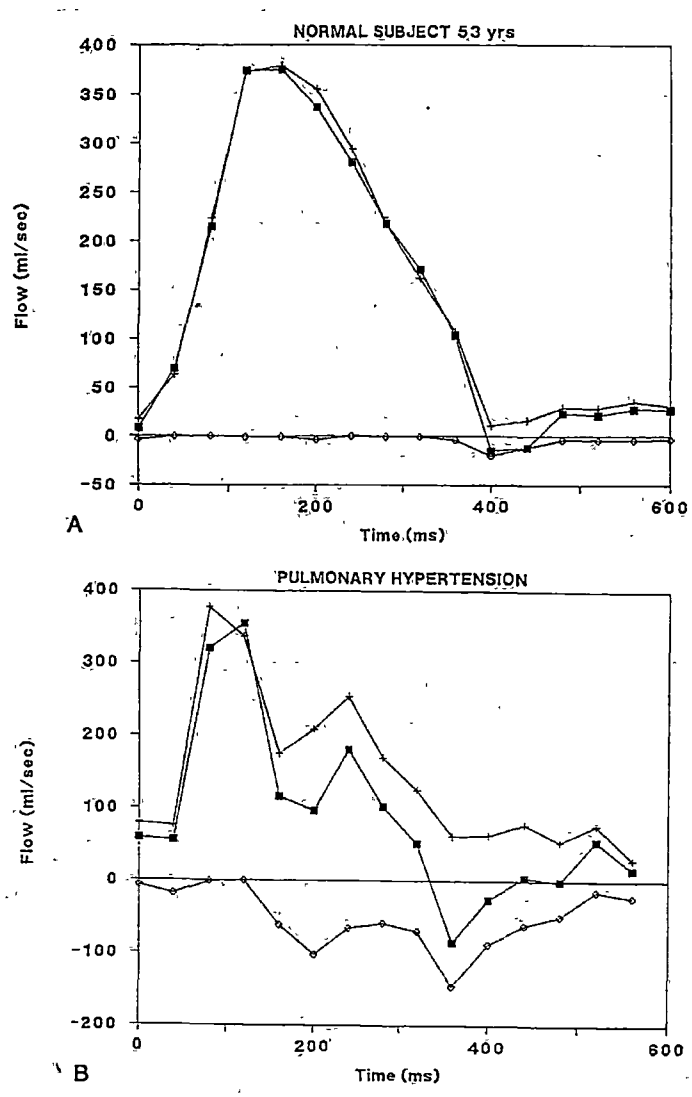

Fig. 5. Mid pulmonary artery flow in a normal subject (A) and in a patient with pulmonary arterial hypertension (B).

Figure 3.5.11 Normal (A) and Pulmonary Hypertension (B) Flow Waveforms in the Pulmonary Artery. Solid square = net forward flow, diamond = reverse flow, cross = forward flow. [63].

Figure 3.5.12 shows the velocity profile in the normal pulmonary artery. It has a consistently skewed mean temporal velocity profile (not shown) with a well-defined low flow region located to the inferior right.

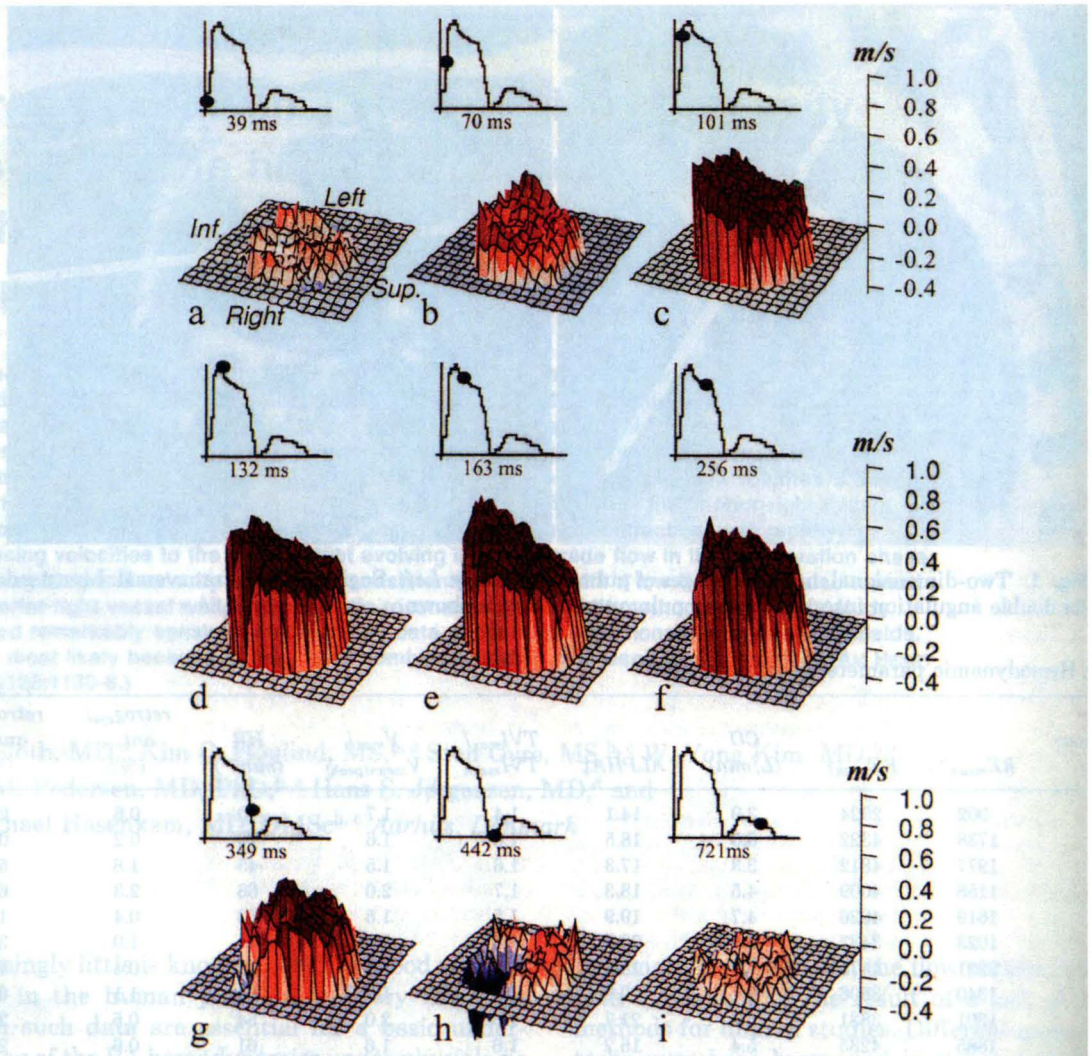

Fig. 2. Typical example (volunteer 1) of three-dimensional visualization of temporal and spatial development of velocity profile viewed from downstream position. *Top left*, time in cardiac cycle is indicated on mean velocity curve with time interval relative to R wave in recorded electrocardiogram (milliseconds). Anatomic orientation shown in *velocity profile a* is used in successive plots. **a,** Beginning of cycle; **b** and **c,** acceleration phase; **d** and **e,** peak systole; **f, g,** and **h,** deceleration phase; **i,** diastole.

Figure 3.5.12: Normal pulmonary artery velocity profile throughout the cardiac cycle. [64].

Figure 3.5.12 gives no indication of the distensibility of the pulmonary artery. (change is cross sectional area of flow with cardiac phase). Figure 3.5.13 shows both the cross sectional area and velocity distribution in the pulmonary artery. The white circle represents the perimeter of the pulmonary artery. As can be seen in (A) the

cross sectional area of the pulmonary artery changes significantly during the cardiac cycle of a normal individual. As in Figure 3.5.12 and Figure 3.5.11 the flow profile is relatively uniform forward flow throughout the main part of the cardiac cycle (white-blue), with little reverse flow (red). While the larger cross sectional area appears relatively constant in (B) pulmonary hypertension, a highly heterogeneous reverse flow (red) is present as suggested by Figure 3.5.11. Numerical data is given in Table 3.5.4.

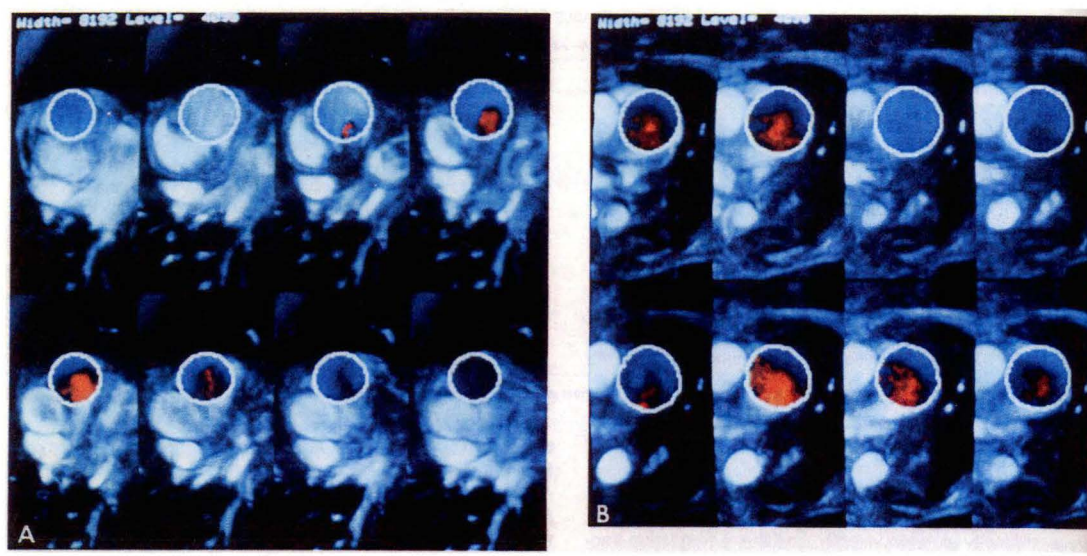

Figure 3.5.13: Normal (A) and pulmonary hypertension (B) velocity profiles in pulmonary artery throughout cardiac cycle. White circle = perimeter of pulmonary artery. Blue = forward flow, Red = reverse flow. [65].

Table 3.5.4: Normal and pulmonary hypertension pulmonary artery velocity and cross sectional area data. [65].

TABLE 2

DIFFERENCES IN MAGNETIC RESONANCE PARAMETERS BETWEEN PATIENTS WITH PRIMARY PULMONARY HYPERTENSION AND HEALTHY SUBJECTS*

Main Pulmonary Artery	Patients	Volunteers	p Value
Maximal antegrade velocity, cm/s	60 ± 20	79 ± 18.4	< 0.005
Maximal mean velocity, cm/s	34.8 ± 13.06	55 ± 15.2	< 0.005
Maximal surface, cm^2	10.5 ± 2.8	8.2 ± 0.9	< 0.05
Minimal surface, cm^2	9.5 ± 2.6	6.5 ± 0.8	< 0.005
Mean surface, cm^2	10.1 ± 2.7	7.3 ± 1	< 0.005
Pulmonary distensibility, %	13 ± 7.07	23.8 ± 6.1	< 0.0005
Acceleration time, ms	93.46 ± 22.5	153.2 ± 19.2	< 0.0005
Maximal retrograde velocity, cm/s	35 ± 14.3	24 ± 5.4	< 0.05
Regurgitation fraction, %	22.9 ± 10	7.46 ± 4	< 0.0005
Maximal velocity/mean velocity	1.84 ± 0.56	1.45 ± 0.16	< 0.05

* Results are expressed as mean ± SE.

One of the main methods for evaluating pulmonary hypertension is assessment of tricuspid regurgitation using ultasound. Figure 3.5.14 shows the difference between flow measured by integrating MRI velocity and flow measured by MRI ventricular volume changes. Even considering error it seems reasonable to conclude that measurement of flow based on ventricle volume is overestimated in pulmonary hypertension.

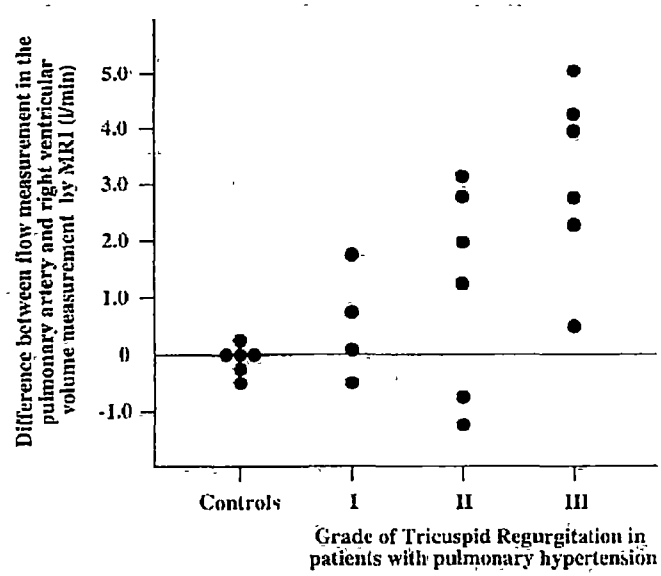

FIGURE 2. Differences between estimation of cardiac output by flow measurements in the pulmonary artery and right ventricular volume measurements (SV as determined by the difference between end-diastolic and end-systolic chamber volume times heart rate) in relation to the severity of tricuspid regurgitation See text for the grading of tricuspid regurgitation

Figure 3.5.14: Difference between flow measured by integrating MRI velocity and flow measured by MRI ventricular volume changes. Controls are normal. [66].

For the same pulmonary hypertension patients, Figure 3.5.15 shows the difference between thermodilution derived flow and MRI velocity derived flow showing reasonable agreement between the two (within the known error of the thermodilution method).

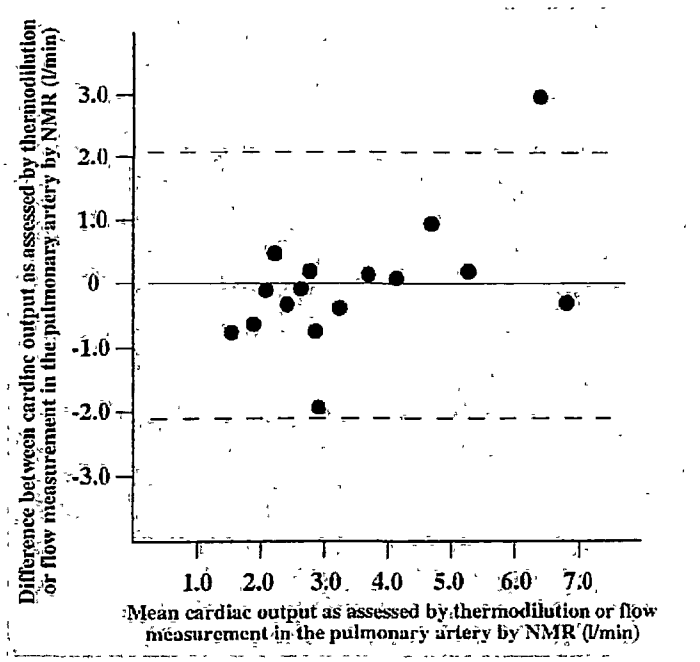

Figure 3.5.15: Difference between flow derived from thermodilution and flow derived from MRI velocity integration for the same pulmonary hypertension patients in Figure 3.5.14. [66].

General

Figure 3.5.16 shows the change in cross sectional area inside the pericardium between systole and diastole. As can be seen, the largest change in cross sectional area occurs at the base end of the ventricles. There is relatively little change at the apex.

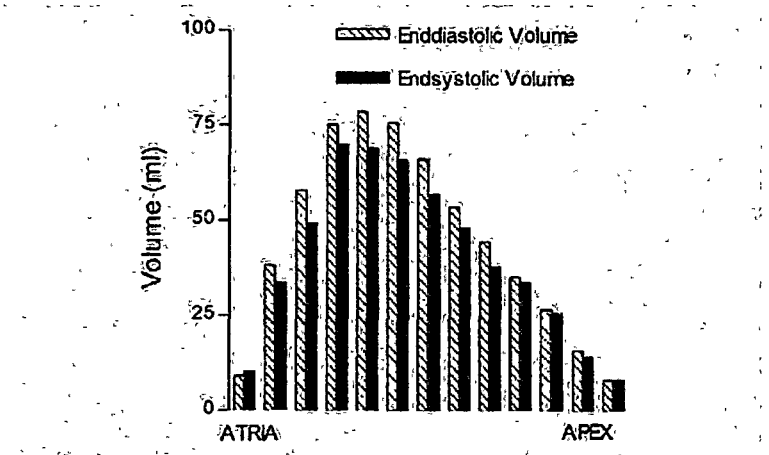

Fig. 6. Anatomic location of change in total heart volume in a typical subject. The main part of the change in volume between diastole and systole was located at the base of the ventricles i.e., where the diameter of the heart is largest. A typical finding was a decrease in volume in all slices of the heart during ventricular systole. The largest slices, and the largest contribution to total heart volume change, were found at the midcardiac level, at the region of the AV plane movement.

Figure 3.5.16: Cross sectional area inside the pericardium at end diastole/end systole. [67].

The difference between end systole and end diastole pericardium volume is due to more outflow of blood than inflow over the period of time from end-diastole to end-systole. Instantaneous and cumulative blood inflow and outflow is shown in Figure 3.5.17. As can be seen, the total heart volume difference between end systole and end diastole is around 100ml.

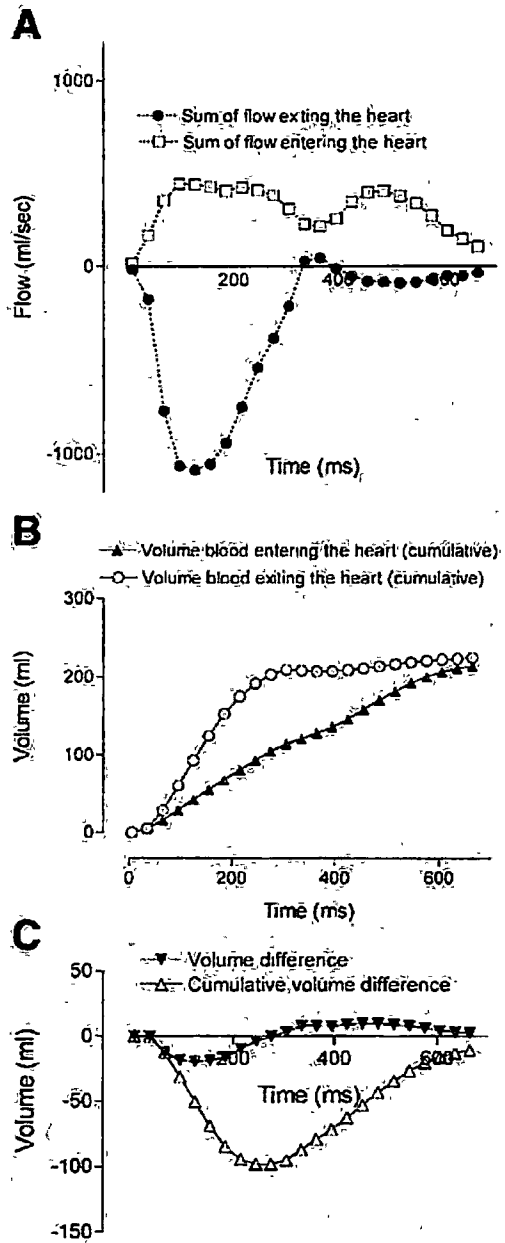

Fig. 5. Temporal difference of cardiac inflow and outflow by flow measurements in one subject. Change in total heart volume was calculated as cumulative volume difference (*C*; Δ). This was done by mapping inflow and outflow (*A*) and calculating the cumulative volume (*B*) as the sum of inflow and outflow at each phase of the cardiac cycle. *A*: total flow leaving the heart (the sum of the flows of the aorta and the pulmonary artery) is pulsatile and the total flow entering the heart (the sum of the flows of the cava and pulmonary veins) is more continuous. Positive values are inflow and negative values outflow. *B*: there is a discrepancy in time of the cumulative values of the volume entering and leaving the heart due to the difference in flow patterns described in *A*. The cumulative curves diverge during systole and converge during diastole. This results in a decrease in total volume in systole that returns to the presystolic volume during diastole. *C*: volume difference (▼) is negative during systole, meaning that total heart volume (Δ) decreases. When the volume difference changes from negative to positive values the total heart volume regains its original value.

Figure 3.5.17: Volume flow into and out of heart during the cardiac cycle. [67].

Figure 3.5.18 shows the changes in ventricle blood cavity dimensions during the cardiac cycle. The slopes of these graphs indicate how volume change through the cardiac cycle of the left ventricle is mainly due to cross sectional area change of the blood pool, whereas volume change of the right ventricle is more due to length changes in the blood pool.

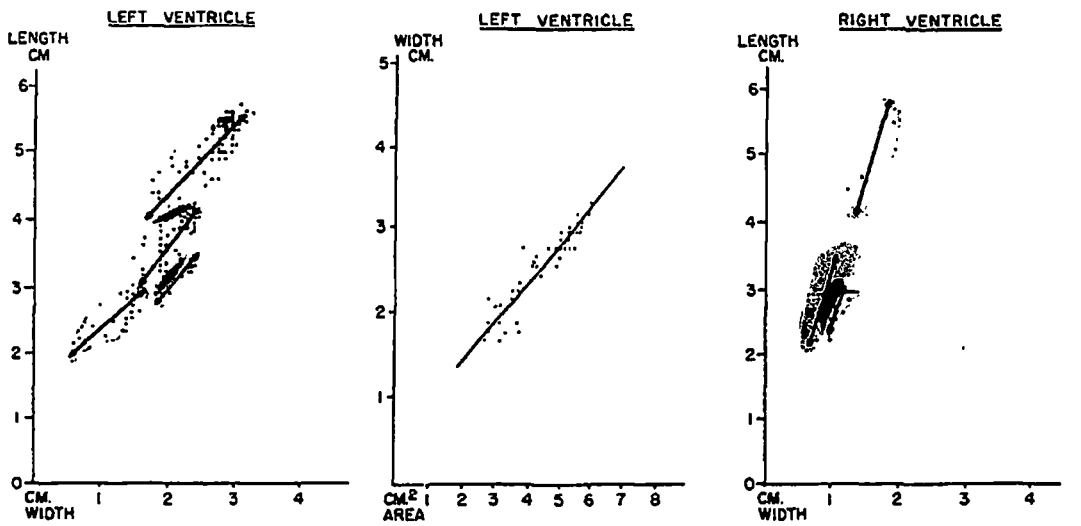

Figure 3.5.18: Changes in ventricluar blood pool dimensions through cardiac cycle. [42].

Normal end systolic and end diastolic ventricular volumes in rest and supine exercise from very high speed MRI are given in Table 3.5.5. The figure shows relatively constant end-diastole ventricle volumes between rest and exercise, but the relatively large decrease in end-systolic volumes with exercise. Also the left ventricle has a higher ejection fraction than the right ventricle.

Table 3.5.5: Ventricular volume at end systole and end diastole during rest and exercise. [68].

TABLE 4 LV and RV Changes from Rest to Stress

	Left Ventricle			Right Ventricle		
	Rest	Exercise	Change (%)	Rest	Exercise	Change (%)
End-diastolic volume (ml)	143 ± 29	138 ± 27	−3.3 ± 5	144 ± 27	144 ± 24	−0.6 ± 8
End-diastolic volume index (ml/min²)	79 ± 9	75 ± 9		79 ± 9	79 ± 7	
End-systolic volume (ml)	54 ± 17	36 ± 12*	−32.6 ± 12	58 ± 17	43 ± 13*	−25.3 ± 12
End-systolic volume index (ml/min²)	29 ± 7	20 ± 5*		32 ± 7	24 ± 6*	
Stroke volume (ml)	89 ± 14	102 ± 19*	+14.3 ± 8	88 ± 14	101 ± 16*	−15.4 ± 8
Stroke volume index (ml/min²)	49 ± 6	56 ± 6*		49 ± 6	56 ± 5*	
Ejection fraction (%)	63 ± 6	74 ± 6*	+18.3 ± 7	61 ± 6	70 ± 6*	+16.6 ± 8
Cardiac output (L/min)	6.3 ± 1.0	12.3 ± 2.3*	+97.5 ± 14	6.2 ± 1.0	12.0 ± 2.1*	+99.4 ± 13
Cardiac index (L/min/m²)	3.5 ± 0.4	6.8 ± 0.8*		3.4 ± 0.4	6.7 ± 0.6*	

*Significant change from rest to stress, $p < 0.05$.

Typical movement of the normal (no right ventricular overload) heart base between atria and ventricles from M mode ultrasound is shown in Table 3.5.6. The mitral annulus shows significantly less displacement than the tricuspid annulus. There is a significant change in displacement across the septum.

Table 3.5.6: Heart base displacement. [69].

Table 1 Total excursion and that attributable to atrial contraction-relaxation *(a)* are listed for tricuspid and mitral annular motion in 10 normal subjects and 29 patients with no signs of right-sided heart disease

	Normal subjects		Patients	
	Total excursion	Atrial contraction-relaxation	Total	Atrial contraction-relaxation
Tricuspid anulus				
Lateral point	24.9 ± 3 5	7.3 ± 1.9	21.9 ± 2.7	8.6 ± 2.8
Septal point	20.1 ± 2.5	6.3 ± 2.1	15.8 ± 3.6	6.7 ± 2.8
Anterior point	21.6 ± 3 8	7.7 ± 2.7	18.6 ± 4.8	8.0 ± 2.8
Posterior point	22.3 ± 2.3	6.8 ± 1.9	19.1 ± 3.6	8.2 ± 2.6
Mitral anulus				
Lateral point	17.8 ± 4.0	5.7 ± 1.6	12.6 ± 2.8	5.3 ± 1.7
Septal point	14.6 ± 2.7	5.9 ± 1.2	11.4 ± 2.5	4.9 ± 1.4
Anterior point	15.7 ± 2 7	5.2 ± 1.4	12.2 ± 3.2	4.9 ± 1.4
Posterior point	16.8 ± 2.6	5.7 ± 1.3	12.5 ± 3.0	5.1 ± 1.6

Numbers are expressed in millimeters ± 1 standard deviation.

The normal size of the aortic and pulmonary valves are given in Table 3.5.7 and the normal and abnormal sizes of the tricuspid and mitral valves are given in Table 3.5.8.

Table 3.5.7: Normal aortic and pulmonary valve size at autopsy. [70].

TABLE II Mean Values for Aortic and Pulmonary Valve Dimensions

	Aortic	Pulmonary
Circumference (cm)*		
Overall	7.28 ± 0.92	7.63 ± 0.93
Male	7.50 ± 1.04	7.77 ± 0.98
Female	6.80 ± 0.89	7.32 ± 0.86
Area (cm^2)		
Overall	4.56 ± 1.12	4.71 ± 1.16
Male	4.81 ± 1.30	4.88 ± 1.25
Female	3.73 ± 0.98	4.32 ± 1.03
Diameter (mm)		
Overall	23.20 ± 3.3	24.30 ± 3.0
Male	23.80 ± 3.3	24.70 ± 3.1
Female	21.60 ± 2.8	23.30 ± 2.7

* Primary valve measurement. Area and diameter derived by calculation.
Values are mean ± standard deviation.

Table 3.5.8: Normal tricuspid and mitral valve size at autopsy. [70].

TABLE I Mean Values for Mitral and Tricuspid Dimensions with and without Congestive Heart Failure (CHF)

	Without CHF		With CHF		Overall	
	Mitral	Tricuspid	Mitral	Tricuspid	Mitral	Tricuspid
Circumference (cm)*						
Overall	9.79 ± 1.23	11.63 ± 1.39	10.46 ± 1.26	12.22 ± 1.43	10.05 ± 1.28	11.74 ± 1.45
Male	10.15 ± 1.24	11.95 ± 1.26	10.68 ± 1.26	12.48 ± 1.44	10.38 ± 1.27	12 12 ± 1.36
Female	9.11 ± 0.86	10.40 ± 1.06	9.71 ± 1.00	11.46 ± 1.14	9.29 ± 0.94	10.77 ± 1.18
Area (cm^2)						
Overall	7.76 ± 1.93	10.56 ± 2.59	8.83 ± 2.12	12.05 ± 2.87	8 17 ± 2.07	11.14 ± 2.79
Male	8.33 ± 1.98	11.50 ± 2.46	9.21 ± 2.13	12.56 ± 2.94	8.70 ± 2.08	11.90 ± 2.72
Female	6.66 ± 1.26	8.75 ± 1.74	7.58 ± 1.55	10.54 ± 2.07	6.94 ± 1.41	9.33 ± 2.02
Diameter (mm)						
Overall	31.1 ± 3.9	36.4 ± 4.4	33.3 ± 4.0	38.9 ± 4.6	32.0 ± 4.0	37.3 ± 4.6
Male	32.3 ± 3.9	38.0 ± 4.0	34.0 ± 4.0	39.7 ± 4.6	33.0 ± 4.0	38.8 ± 4.3
Female	29.0 ± 2.7	33.2 ± 3.3	30.9 ± 3.1	36.4 ± 3.6	29.6 ± 3.0	34.3 ± 3.6

* Primary valve measurement. Area and diameter derived by calculation.
Values are mean ± standard deviation.

Autopsy (fresh) results show increased valve dimensions relative to maximum echocardiography dimensions [105]. Larger tricuspid valve dimensions are associated with tricuspid regurgitation [105]. The tricuspid valve changes circumference and area during the cardiac cycle with a reduction in area of approximately 33% (±4%SD) in normals and 18% (±4%SD) in tricuspid regurgitation [105].

Figure 3.5.19 shows the distribution of longitudinal displacement of the left ventricle between base and apex for both normal and right ventricle pressure overload. The longitudinal shortening is approximately constant from apex to base. Right ventricular overload is associated with significantly less longitudinal shortening.

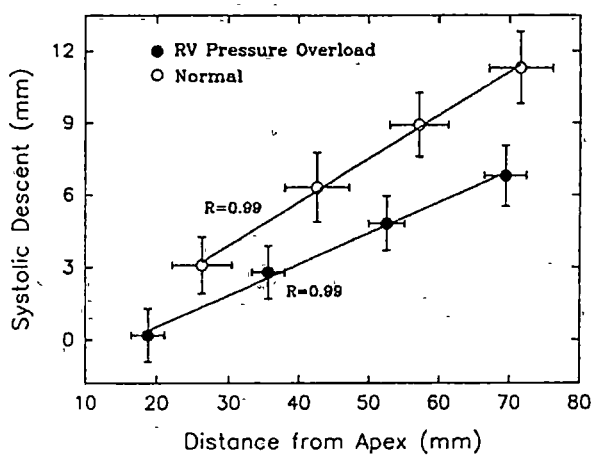

FIG 3. Graph showing relations between the longitudinal systolic descent of the tags and their end-diastolic distance from the epicardial apex for healthy subjects and for patients with chronic right ventricular pressure overload (RVPO) (averaged data of four different circumferential regions). Note that there were very good linear descent–distance relations for both sets of data and that the slope of the relation in the patient group was significantly less than that in healthy subjects (0.13 vs 0.18, $P<.005$), indicating that the longitudinal shortening in patients with RVPO was less than that in healthy subjects.

Figure 3.5.19. Longitudinal displacement of the left ventricle towards apex during systole. [71].

As shown in Figure 3.5.20, the left ventricle circumferential shortening in the epicardium is small in both normal and right ventricular overload, compared to endocardium shortening. Right ventricular overload is associated with less circumferential shortening than normal.

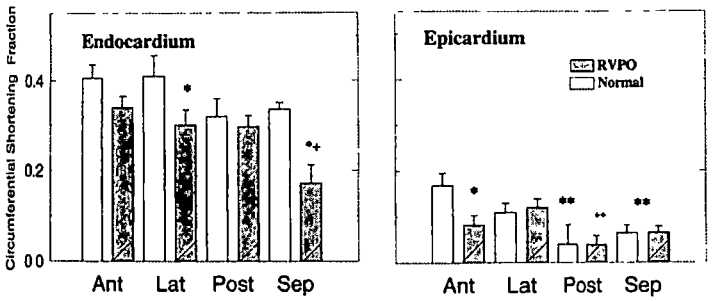

FIG 8. Bar plots showing the averaged endocardial (left) and epicardial (right) circumferential shortening fraction in different regions. Compared with the values of healthy control subjects, the endocardial shortening fraction of the septum and lateral wall decreased significantly in patients with chronic right ventricular pressure overload (RVPO), whereas no significant differences were seen in the anterior and posterior regions between the two groups. *$P \leq .05$, endocardial or epicardial shortening of RVPO patients vs those of the healthy subjects; +$P < .05$, endocardial shortening of the septum vs the other three regions in RVPO patient; **$P < .05$, shortening of epicardium at posterior wall and right surface of the septum vs the anterior region in healthy subjects; and ++$P < .05$, epicardial shortening of the posterior wall vs the lateral region in RVPO patients. Ant indicates anterior; Lat, lateral; Post, posterior; and Sep, septal regions of left ventricle.

Figure 3.5.20. Left ventricle circumferential shortening fraction during systole. For different positions around the ventricle. [71].

As shown in Figure 3.5.21, the thickness of the left ventricle myocardium in right ventricular overload is greater than normal. However, the absolute and fractional thickening is reduced. The large value of the fraction thickening is due to the fibre structure of the myocardium [72]. As discussed previously, the myocardium fibre direction is in every direction, but primarily tangent to the wall, not in a normal direction. Conservation of volume means that if muscle contracts in one direction it must expand in another. Due to fibre architecture it cannot expand in a tangent direction and therefore thickness changes occur in the radial direction.

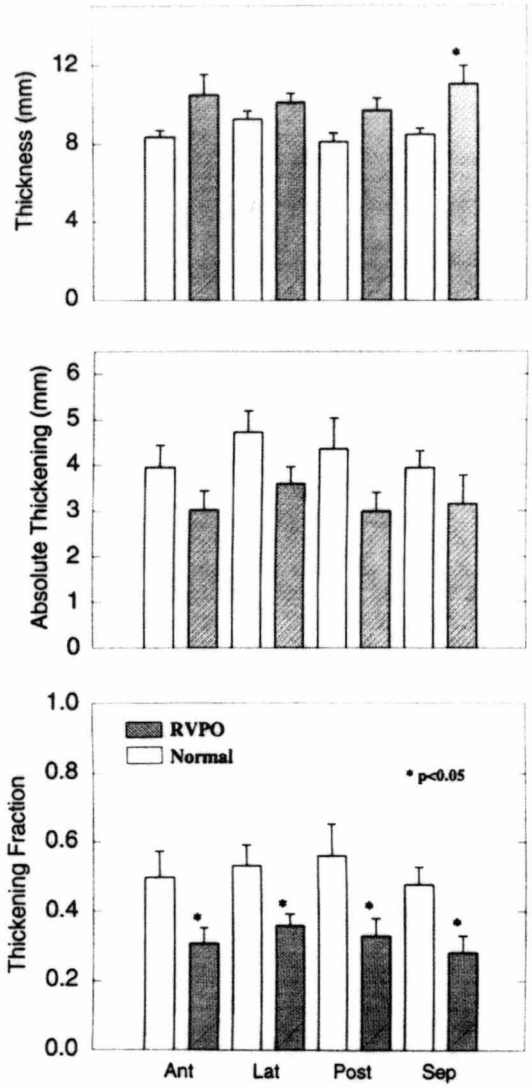

FIG 6. Bar plots showing the average end-diastolic thickness, absolute thickening, and thickening fraction of patients with chronic right ventricular pressure overload (RVPO) (shaded bars) and healthy subjects (open bars) at anterior (Ant), lateral (Lat), posterior (Post), and septal (Sep) regions of the left ventricle. The thickness was greater in RVPO patients than in healthy subjects, but the difference was significant only in the septal region. However, the thickening fraction in patients with RVPO was significantly less than that in the healthy subjects at each region, whereas there was no difference in absolute thickening between healthy subjects and RVPO.

Figure 3.5.21: Left ventricle myocardium thickness and thickening. [71].

As can be seen in Table 3.5.9 the wall curvature is uniform around the normal left ventricle. However in right ventricle overload the curvature is reduced in the septum relative to other locations around the wall.

Table 3.5.9: Wall curvature of left ventricle. [71].

TABLE 3. Changes in Regional Curvatures of the Left Ventricle in Patients With RVPO Compared With Those in the Normal Subjects

	Normal Subjects		RVPO Patients	
	End Diastole	End Systole	End Diastole	End Systole
Circumferential curvature				
Anterior	0.038±0.001	0.049±0.003	0.043±0.003†	0.057±0.005†
Lateral	0.040±0.002	0.056±0.003	0.036±0.002	0.041±0.003*
Posterior	0.038±0.001	0.049±0.002	0.040±0.002‡	0.050±0.003‡
Septal	0.040±0.002	0.049±0.003	0.030±0.001*	0.029±0.006*
	P=NS	*P*=NS	*P*< 005	*P*<.001
Meridional curvature				
Anterior	0 011±0.005	0.014±0.005	0.014±0.002	0.013±0.002
Lateral	0.012±0.002	0.017±0.008	0.013±0.002	0.010±0.002
Posterior	0.013±0.003	0.014±0.004	0.007±0.002§	0.011±0.003
Septal	0.011±0.003	0.010±0.003	0.009±0.002	0.013±0.004
	P=NS	*P*=NS	*P*<.05	*P*=NS

RVPO indicates right ventricular pressure overload. Values are mm^{-1}.
*P<.005 compared with the normal subjects. †P<.05 compared with lateral and septal regions and ‡P<.005 compared with septal region in the circumferential curvature in the RVPO patients. §P<.05 compared with the anterior and lateral regions in the meridional curvature in the RVPO patients.

So far only left ventricle dynamics have been discussed. Normal right ventricular displacement towards apex during systole is shown in Figure 3.5.22. Considerable longitudinal basal displacement of the free wall decreasing smoothly towards the apex is indicated.

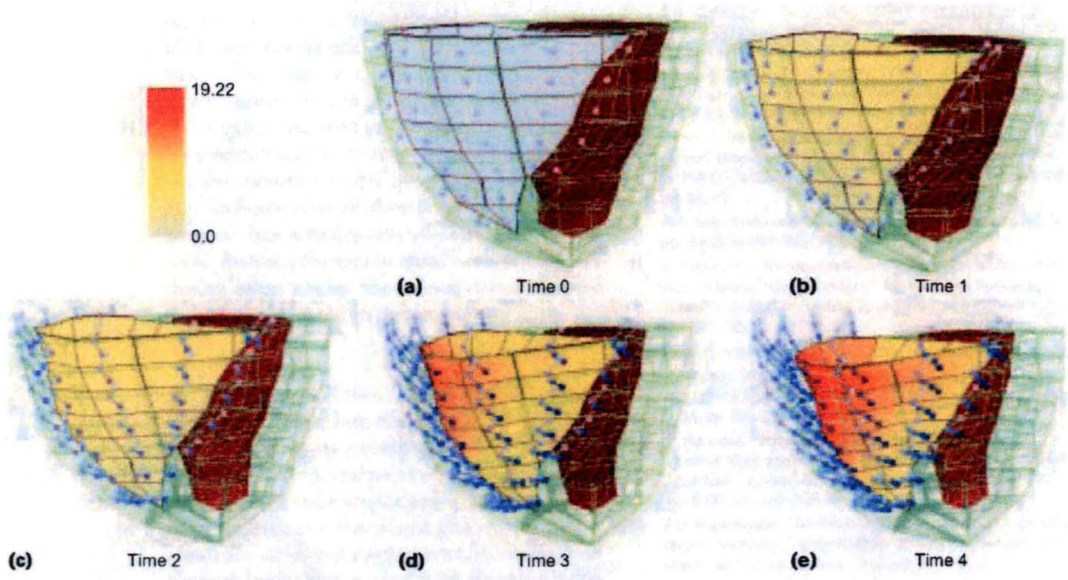

Figure 13. Normal heart displacement through systole shown as a color plot on the RV endocardial free wall. The paths of points located in the centers of the elements are shown from end diastole (white) to end systole (blue).

Figure 3.5.22: Right ventricle longitudinal displacement. [73].

The heart undergoes slight torsion relative to the base. Average torsion about the left ventricle long axis is shown during systole for base, midsection and apex, of the right ventricle, septum and left ventricle, in Figure 3.5.23. Rotation is negligible at the relatively fixed base. Rotation increases from base to apex.

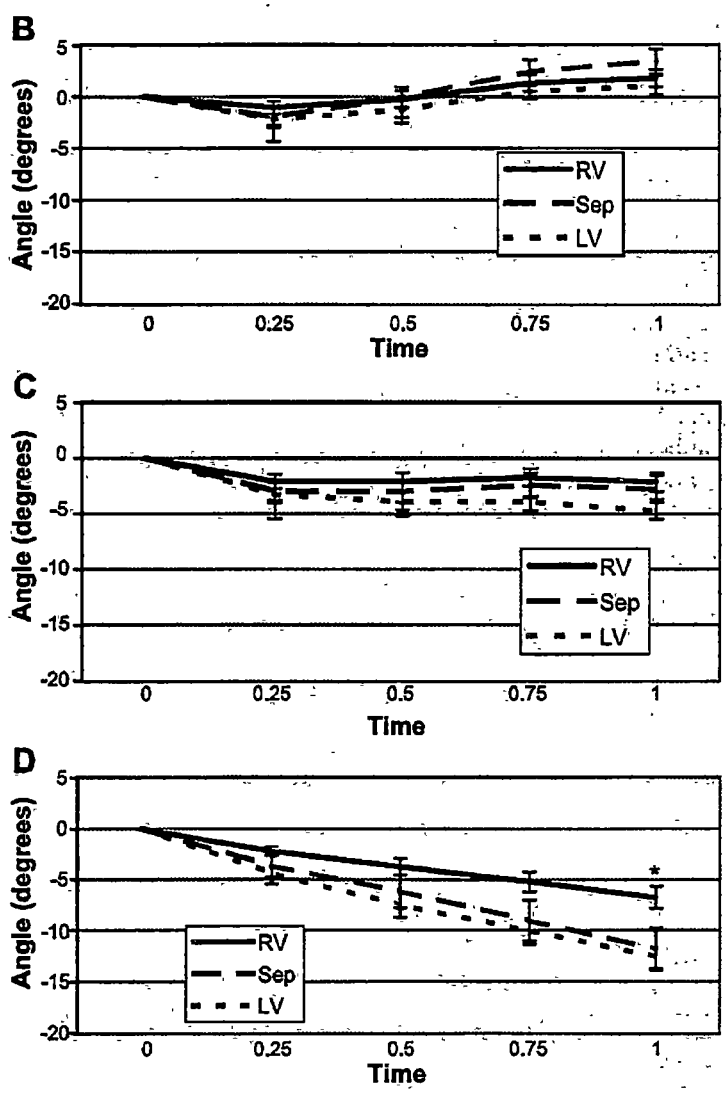

Fig. 7. Angular motion about LV long axis in three cross sections [reference (*A*), base (*B*), midsection (*C*), and apex (*D*)] of RV (solid line), septum (sep, dashed line), and LV (dotted line). Angular position is plotted as function of normalized systolic time with counterclockwise positive. End-systolic angular displacement of RV apex was significantly less than that of LV (*$P < 0.05$).

Figure 3.5.23: Average rotation of the heart. [74].

The previous figure gives no indication of torsion across the ventricular wall thickness. Figure 3.5.24 shows rotation at the left ventricle epicardium and endocardium. There is greater rotation at endocardium than epicardium.

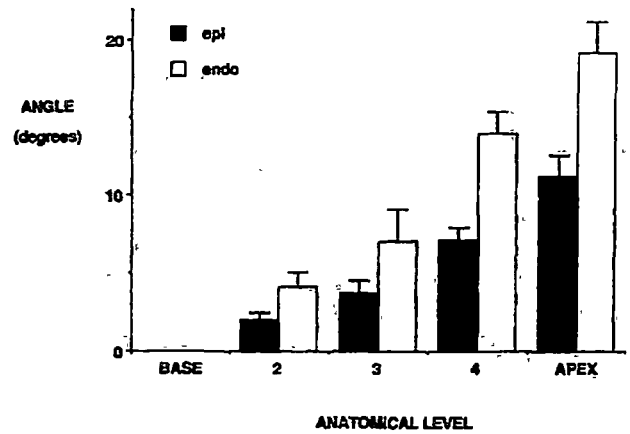

FIGURE 5. *Bar graph showing mean torsion angles of epicardium and endocardium of five left ventricular slices (±SEM). Difference in torsion angles between slices is significant for both epicardium ($p<0.001$) and endocardium ($p<0.001$). Endocardial torsion angles are greater than epicardial ($p<0.001$).*

Figure 3.5.24: Left ventricle epicardium and endocardium rotation. [75].

Ventricular rotation is thought to help evenly distribute stress in the myocardium [76]. Figure 3.5.25 shows strong correlation between left ventricular torsion and endocardium radius in systole.

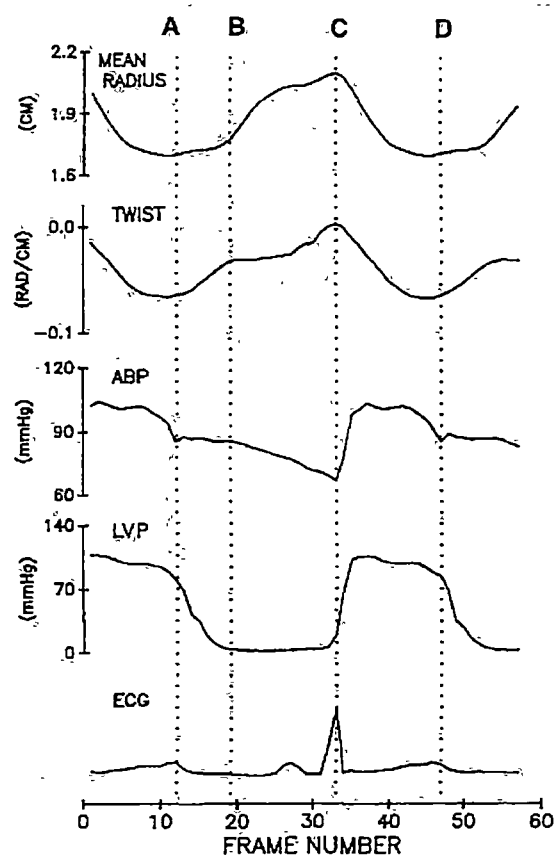

FIGURE 1. A–B is the isovolumic relaxation phase and C–D is the ejection phase. Note that during ejection, twist and shortening (change in mean radius) are linear; during isovolumic relaxation, rapid twist recoil happens before lengthening. ABP: aortic blood pressure; LVP: left ventricular pressure. Reproduced with permission from Beyar *et al.*[26]

Figure 3.5.25: Correlation between left ventricle torsion and mean left ventricular radius in systole. [76].

Table 3.5.10 shows general anatomic changes in the heart with pulmonary hypertension. As can be seen the right ventricular free wall thickens considerably and the septum also thickens slightly, with enlargement of the pulmonary artery in primary pulmonary hypertension.

Table 3.5.10 Changes in heart dimensions associated with pulmonary hypertension. [77].

TABLE II Pulmonary Artery and Right Ventricular Dimensions as Measured by Magnetic Resonance Imaging

	Normals	1° PAH	2° PAH (LD)	2° PAH (Eisenmenger)	p Value
Main PAD (cm)	2.5 ± 0.4	3.9 ± 0.5*	3.6 ± 0.5*	3.7 ± 0.5*	0.05
Main PA/asc. aorta	0.9 ± 0.2	1.4 ± 0.2*	1.1 ± 0.1	1.4 ± 0.3*	0.05
Desc. LPA/desc. aorta	0.4 ± 0.1	1.1 ± 0.3*	0.8 ± 0.1*	1.0 ± 0.2*	0.01
RVWT (cm)	0.3 ± 0.1	1.2 ± 0.4*	0.6 ± 0.1	1.3 ± 0.3*	0.01
SWT (cm)	1.0 ± 0.1	1.2 ± 0.3*	1.2 ± 0.3	1.3 ± 0.5	0.05
PWT (cm)	1.0 ± 0.1	1.1 ± 0.2	0.9 ± 0.1	1.0 ± 0.3	NS

* Significant difference compared with values in normal subjects.
Values are mean ± standard deviation.
Asc. = ascending; Desc. = descending; Desc. LPA = descending left pulmonary artery; NS = not significant; PA = pulmonary artery; PAD = PA diameter; 1° and 2° PAH = primary and secondary pulmonary hypertension; PWT = posterior wall thickness of the left ventricle; RVWT = right ventricular wall thickness; SWT = septal wall thickness.

The wall thickness correlation with pulmonary artery pressure is shown in Figure 3.5.26

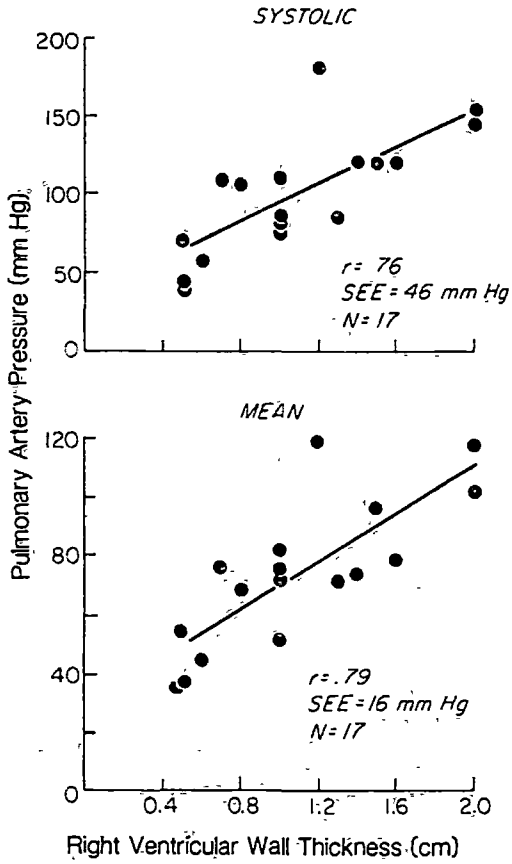

FIGURE 4. Top, relation between systolic pulmonary artery pressure and right ventricular wall thickness. **Bottom,** relation between mean pulmonary artery pressure and diastolic right ventricular wall thickness.

Figure 3.5.26: Wall thickness correlation with pulmonary artery pressure. [77].

In pulmonary hypertension, the right ventricle also typically shows an increase in right ventricle end-diastolic and end-systolic volume. This results in a significantly reduced ejection fraction. This is shown in Table 3.5.11. Left ventricle end-systolic volume remains relatively constant, however stroke volume is reduced. The short axis MRI series in Figure 3.5.27 shows septum curvature in pulmonary hypertension at various stages through the cardiac cycle. At the start of systole, the septum is curved towards the right ventricle. Right ventricular systole is typically longer than left ventricle systole. As a result, the high right ventricle pressure typically causes the septum to straighten or bow towards the left ventricle in early left ventricular diastole [51]. The relation between pulmonary artery pressure and septum curvature is further

shown in Figure 3.5.28. Higher pulmonary artery pressures are associated with septum straightening or bowing into the left ventricle.

Table 3.5.11: Performance of the ventricles in pulmonary hypertension. [78].

Table 1—*MRI-Derived Parameters and PAP Pressures as Obtained by Catheterization**

Variables	Patients	Control Subjects	p Value
RV EDV, mL	163 ± 44	119 ± 17	0.01
RV ESV, mL	111 ± 45	38 ± 10	< 0.0001
RV SV, mL	52 ± 12	82 ± 11	< 0.0001
RV EF, %	34 ± 11	69 ± 6	< 0.0001
LV EDV, mL	81 ± 23	117 ± 19	0.001
LV ESV, mL	32 ± 14	33 ± 10	NS
LV SV, mL	49 ± 15	83 ± 13	< 0.0001
LV EF, %	60 ± 14	75 ± 6	0.014
Peak LV-filling rate, EDV/s	2.2 ± 0.7	3.3 ± 0.5	0.001
Septal curvature, cm^{-1}	−0.14 ± 0.07†	+0.30 ± 0.05	< 0.0001
LV free-wall curvature, cm^{-1}	+0.34 ± 0.05	+0.36 ± 0.03	NS
Septal/free-wall curvature ratio	−0.42 ± 0.21†	+0.84 ± 0.11	< 0.0001
AT/ET ratio	0.29 ± 0.04	0.38 ± 0.05	0.03
Heart rate, beats/min	78 ± 14	57 ± 11	0.01
PAP systolic, mm Hg	83 ± 13		
PAP diastolic, mm Hg	35 ± 8		
PAP mean, mm Hg	56 ± 8		

*Values are presented as mean ± SD. EF = ejection fraction.
†Negative septal curvature value indicates leftward septal bowing.

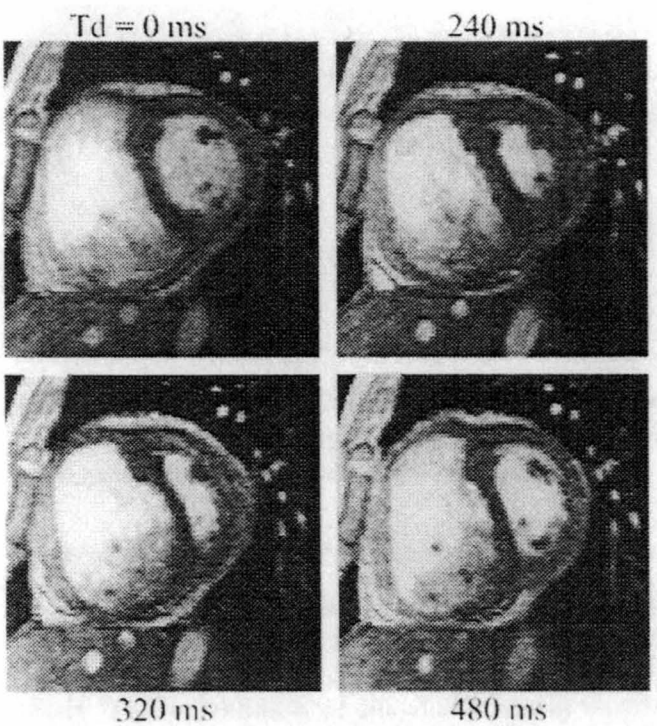

FIGURE 1. Short-axis cine frames at different trigger delays (Td) during the cardiac cycle in a patient with PPH. In early diastole (Td = 320), the ventricular septum bows to the left.

Figure 3.5.27: Ventriclar septum curvature in pulmonary hypertension. [78].

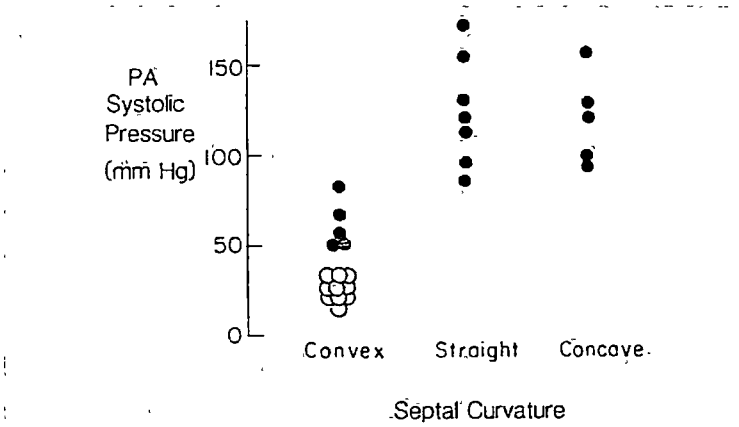

FIGURE 5. Relation between systolic pulmonary artery (PA) pressure and septal curvature. Patients with pressure greater than 90 mm Hg had either a straight or concave septum. **Open circles** represent values from normal volunteers, where pressures were not measured but assumed to be normal on the basis of physical examination.

Figure 3.5.28: Correlation between septum curvature and pulomonary artery pressure. [77].

3.6 Conclusion

As was concluded in Section 3.2, the conductance catheter promises to be one of the most suitable techniques for an implantable blood flow sensor. Previous research identified in Section 3.3 indicated that the effects of catheter position and respiration in free breathing, need further investigation. Also, Section 3.5 concluded that since volume change in the right ventricle is primarily due to length change, rather than change in cross-section area as in the left ventricle, then standard left ventricle methods may be grossly inaccurate when applied to finding stroke volumes and absolute volumes in the right ventricle. The effects of catheter position and myocardium conductivity will be further investigated in the next chapter using numerical models. Numerical models provide a controlled experimental environment, unparalleled with experimental techniques.

In the next chapter, models of the heart will be developed from medical imaging information to enable simulation of the conductance catheter. The electric field will be determined based on finite element analysis. This analysis requires conductivity information of various tissues. The geometry will be simplified along with the conductivity of tissues. From the detailed information contained in Section 3.4 and Section 3.5 (and Section 2.2) the limitations of these models can be put into perspective. Little is know about catheter movement during the cardiac cycle.

The modelling will be limited to the extent of the myocardium of the ventricles. This assumes no current leaks into the relatively low conductivity (Section 3.4) of the adjacent liver, lungs and through the fat present around the heart. The model also assumes that both the blood and myocardium are isotropic conductors. Blood at low shear rates appears to be isotropic (Section 3.4). However, as discussed, myocardium conductivity is somewhat anisotropic. The myocardium fibre direction changes considerably over a small distance through the ventricle wall as discussed in Section 3.5. The models assume a normal heart. The effect of pulmonary hypertension on the shape and dynamics of the ventricles was discussed in Section 3.5. Myocardium motion information allows one to see how the presence of fat can affect the dynamics of the ventricles.

The material on blood flow in Section 3.5 shows how determining blood flow from volume changes may lead to error in pulmonary hypertension (due to tricuspid regurgitation), but also how other techniques such as ultrasound may be affected by the heterogeneous velocity profile. Deformation of the heart due to respiration was presented in Section 3.5. The evidence suggests deformation may be modelled in future work by applying an affine transformation.

Chapter 4. Investigation 1

4.1 Introduction

This chapter concentrates on three-dimensional finite element simulation of the conductance catheter in the heart. In the last chapter the conductance catheter was proposed as one of the most promising techniques for an implantable blood flow sensor. Among the most prominent error sources suggested was catheter position. Myocardium conductivity may affect both the gain factor and parallel conductance in (2.3.1)/(3.2.6). The aim of this chapter is to identify the magnitude of effect of these two variables. The primary results from the simulation will be five segmental voltages at end-diastole and end-systole for an eight-electrode catheter with current applied between outer electrodes. The effect of catheter position and myocardium conductivity will be assessed for both left and right ventricular catheters. Surfaces of the right ventricle, left ventricle and outside of the heart will be modelled based on MRI and Tagged MRI images. Each region will be allocated a particular value of conductivity. The volumes enclosed by the surfaces will be then meshed into finite elements and the electric field for a catheter will be solved. A further aim of this chapter is to show it is feasible to develop a realistic three-dimensional model to implement the methods detailed in chapters 5 and 6.

4.2 Methods

Two geometry models of the heart were used for the conductance catheter simulations. Each was based on a different patient, different imaging technique and different reconstruction technique. Two models based on an entirely different construction process and different patients somewhat verify each other if the results are similar. One of the models was based on MRI images and the other was based on Tagged MRI images. A model based on Tagged images was used in addition to one based on normal MRI as a lead in to future work, such as modelling fibre orientation that would move to a new position as the heart beats. This could be useful for modelling heart tissue conductivity that is related to fibre direction. Geometry construction related to the MRI model is detailed first under the methods section entitled MRI Heart Geometry. Geometry construction related to the Tagged MRI model is detailed under the methods section entitled Tagged MRI Heart Geometry. The geometry construction process results in volumes representing the heart myocardium, left ventricle blood pool and right ventricle blood pool in ANSYS 10.0 (ANSYS Inc., Canonsburg, USA) with adjoining volumes using the same areas. Details of the simulation including incorporation of catheter, conductivity assignment, meshing, applying boundary conditions and solving are detailed in the methods section entitled Simulation of Conductance Catheter.

MRI Heart Geometry

MRI short axis scans through the left and right ventricles of a normal patient were obtained from Wendy Strugnell from the Cardiovascular MRI Research Centre at The Prince Charles Hospital in Queensland. These images were in the form of DICOM format files representing consecutive two-dimensional short axis image slices through the patients heart.

The individual files representing the different slices at end-diastole were imported into Amira 4.1.0 (Mercury Computer Systems, Inc., Massachusetts, USA) as an image stack. Another image stack was created of the end-systole images (which were in the same scanner planes as the end-diastole images). Each image stack was opened in Amiras image segmentation editor where points were marked around each of the images representing heart myocardium/epicardium border, left ventricle

endocardium and right ventricle endocardium. The marked points are shown overlaid on the images for end-diastole in Figure 4.2.1

Figure 4.2.1: MRI short axis images (256 x 256 pixels, viewed from below) at end-diastole with marked points (coloured) overlaid. Outer ring of points is the outer surface of the myocardium. The crescent shaped inner ring of dots on the left of the images is the right ventricle endocardium. The circular shaped inner ring on the right of the images is the left ventricle endocardium. From apex (upper left image) to base (lower right).

A three-dimensional array for each image stack with array addresses representing pixels of each image stack was then exported from Amira to MATLAB 7.3.0 (The MathWorks, Inc., Natick, USA). Assigned to each pixel was a number representing the point assigned to it (a different number was assigned to pixels without assigned points). A list of points and their array addresses were then generated in MATLAB. DICOM header information was then used to convert each array address into absolute patient coordinates. The header tags used were image position (0020-0032), image orientation (0020-0037) and pixel spacing (0028-0030). The image position tag specified the coordinate of the centre of one particular pixel in each two-dimensional image slice. The other two tags were then used to identify the coordinate of every pixel in each two-dimensional image slice. Due to the imaging procedure performed the image orientation and pixel spacing tags were the same for every image slice. The image position varied between slices with a constant distance between slices.

Cubic B spline curves were fitted to the points representing the outside of the myocardium, left ventricle endocardium and right ventricle endocardium in each image slice plane. In addition to the points, the only information required to specify the splines was the derivatives of the spline segments meeting at each point. The derivatives were found by solving a set of simultaneous equations for the derivatives. A matrix was formulated for this process. It incorporated desired spline boundary/continuity conditions. Cubic B spline curves were then fitted between adjacent points on adjacent slices using a similar process. The curve generation procedure was written from scratch as available add-ons were not purchased. This allowed curve boundary/continuity conditions to be precisely specified to represent the geometry best (for instance, cusps were used to represent the septum/right ventricular freewall junctions near the apex of the heart and a continuous curve was used around the pulmonary artery at the base).

End point positions and end point derivatives for segments of the fitted splines were then used to specify lines in ANSYS finite element software. ANSYS commands were then used to fit Coons patches (non-rational B spline or NURBS surfaces) to close the wireframe surfaces representing the outside of the myocardium, left ventricle endocardium and right ventricular endocardium. These closed surfaces

were then converted to volumes. The volumes created from the right ventricle endocardium and left ventricle endocardium surfaces represented the two blood pools. Boolean operations were used to subtract these two volumes from the volume representing the outside of the myocardium. This produced a volume representing the myocardium. This volume shared the same areas with the left and right ventricle blood pools allowing coupling between the two for later simulation purposes. The result of this process was three volumes for end-systole and three volumes for end-diastole in ANSYS. The three end-diastole volumes in ANSYS are shown in Figure 4.2.3

Tagged MRI Heart Geometry

NURBS surfaces representing the outside of the myocardium of the two ventricles and the endocardium of the two ventricles at end-diastole and end-systole were obtained from William P. Segars from the Johns Hopkins Outpatient Center in Baltimore. These surfaces were generated from Tagged MRI images of a normal patient [103]. The four surfaces for each of end-diastole and end-systole were continuous with no cusps, each formed out of a single closed NURBS hull.

The eight surfaces were converted from their custom NURBS geometry description into the standard file format IGES using software written from scratch. ANSYS and external CAD software was used to convert the two surfaces representing the outside of the left and right myocardium into a single surface representing the outside of the myocardium. The geometry was too complex for high level ANSYS and external CAD commands (they failed) and the combination required use of lowest level external CAD commands. The surfaces representing the outside of the myocardium and left and right endocardium were converted into volumes in ANSYS. An attempt was made to create the myocardium by subtracting the two endocardium/blood pool volumes from the outside of myocardium volume using Boolean commands, but this failed. Low level commands were used to construct the myocardium volume from the same areas as the left and right blood pools (to enable coupling for later simulation purposes). The result of this process was three volumes for end-systole and three volumes for end-diastole in ANSYS. The three end-diastole volumes in ANSYS are shown in Figure 4.2.2. The Tagged MRI end diastole geometry was identical in size and wall thickness to the MRI end diastole geometry.

Simulation of Conductance Catheter

The catheter geometry detailed in Figure 4.2.4 was generated in ANSYS in the desired location within the desired ventricular blood pool. The catheter volumes representing the electrodes and the catheter shaft were then subtracted from the surrounding blood pool volume. Desired conductivities were assigned to the various volumes. The new blood pool volume, myocardium and other ventricle blood pool volume were then meshed to the desired mesh size/distribution using quadratic ten node tetrahedral electric solid elements (ANSYS element type: SOLID232). Selection of element type was rather arbitrary. A tetrahedral rather than hexahedral element was used so that the complex geometry could be meshed efficiently. The ANSYS user manual suggested that, in general, quadratic elements (like that used) are more efficient than linear elements. After meshing, nodes on the areas representing the catheter electrodes were coupled in the VOLT degree of freedom. A source current of 1 AMP was applied to one of the end electrodes of the catheter and a voltage of zero was applied to the electrode on the other end. The solution for electric potential, based on the governing equation:

$$\nabla \cdot (k \nabla u) = 0 , \qquad 4.2.1$$

where: k = conductivity tensor, u = potential,

was solved by formulating a matrix for the node voltages and solving using the ANSYS sparse matrix solver. The voltage differences across the five segments between the middle six electrodes of the catheter were calculated by subtracting electrode node voltages and recorded.

Two types of studies were performed. In the first, the catheter was moved and conductivity remained constant. In the second, the catheter was fixed and conductivity ratios were varied. The models were solved for the variety of catheter positions and blood/myocardium conductivity ratios detailed in Table 4.2.1. The procedure was fully automated by parameterising the catheter position and conductivity ratio. A blood/myocardium conductivity ratio of 2.75 was used for catheter position studies and comparison of the MRI and Tagged MRI based models. The catheter was moved between five positions in two planes, approximately perpendicular to each other. The maximum movement range was between 10mm and

20mm at the base (15mm left ventricle, 10mm right ventricle in septum-free wall direction, and 20mm right ventricle in pulmonary artery-liver direction). This was the practical range of movement for a straight catheter, without penetrating the myocardium. The range was approximately centred in the ventricles. In the second type of study the blood/myocardium conductivity ratio was varied between 1 and 4.5. This range represents possible blood/myocardium conductivity ratio.

Table 4.2.1: Different studies (end diastole and end systole). PA-L: pulmonary artery to liver direction, FW-S: ventricle free wall to ventricle septum direction.

Investigation	Ventricle	Model	$\sigma_{blood}/\sigma_{tissue}$	Catheter Position
A	Left	Tagged MRI	2.75	centre
B	Right	Tagged MRI	2.75	centre
C	Left	MRI	2.75	centre
D	Right	MRI	2.75	centre
E	Left	Tagged MRI	2.75	4 positions PA-L
F	Left	Tagged MRI	2.75	4 positions FW-S
G	Right	Tagged MRI	2.75	4 positions PA-L
H	Right	Tagged MRI	2.75	4 positions S-FW
I	Left	Tagged MRI	1, 1.875, 3.625, 4.5	centre
J	Right	Tagged MRI	1, 1.875, 3.625, 4.5	centre

From the segment voltages four different values were calculated. These were:

1. Percentage change in $Ves = 100\frac{Ves - Vesc}{Vesc}$, (4.2.2)

where: Ves = segment voltage for end-systole, $Vesc$ = segment voltage for end-systole of either investigation A or B.

2. $(Ves - Ved) / Ves$, (4.2.3)

where: Ved = segment voltage for end-diastole.

3. Percentage change in (Ves – Ved) $= 100\frac{(Ves - Ved) - (Vesc - Vedc)}{Vesc - Vedc}$, (4.2.4)

where: $Vedc$ = segment voltage for end-diastole of either investigation A or B.

4. Percentage change in $(Ves - Ved) / Ves = 100\dfrac{\dfrac{Ves - Ved}{Ves} - \dfrac{Vesc - Vedc}{Vesc}}{\dfrac{Vesc - Vedc}{Vesc}}$. (4.2.5)

Equation (4.2.2) is the change in actual voltage, as a percent, due to a change in variables. The end systolic voltage will in general have a greater percent change than the end diastole voltage.

Equation (4.2.3) is the percent of the end systole voltage minus end diastole voltage relative to the end systole voltage. Comparison of (4.2.2) with (4.2.3) gives an idea of the error in stroke volume (using the standard conductance catheter technique) due to a change in variables that only occurs during one part of the cardiac cycle. For instance rapid variable changes like a change in catheter position. Similar magnitude of (4.2.3) and (4.2.2) indicate 100% error.

Equation (4.2.4) is the percentage change in end systole voltage minus end diastole voltage, as a percent, due to a change in variables. Equation (4.2.4) gives an idea of the error in stroke volume (using the standard conductance catheter technique) due to a change in variables that remains through the whole cardiac cycle. For instance slow variable changes like a normal change in blood/tissue conductivity. A value of 1% would indicate 1% error.

Equation (4.2.5) is the percentage change in (4.2.3) due to a change in variables. Equation (4.2.5) gives an idea of whether a change in end systole voltage minus end diastole voltage can be cancelled out by the change in end systole voltage. For small values of (4.2.3), (4.2.5) also gives an idea of whether a change in end systole voltage minus end diastole voltage can be cancelled out by the change in end diastole voltage.

Note that the stroke volume calculated using the standard conductance catheter technique is based on the inverse of the absolute voltages (the conductances). However subtraction of two voltages (divided by a voltage) will give the same magnitude as subtraction of the corresponding two conductances (divided by a conductance) provided the difference is small. This is further discussed in Section

4.4. Voltages were used instead of conductances in calculation of (4.2.2), (4.2.3), (4.2.4) and (4.2.5) to be consistent with inverse mapping inputs in Chapter 5 and Chapter 6. However, for a paper that was primarily assessing error in the standard conductance catheter technique, use of conductances would be more appropriate than voltages. This would give exact error rather than approximate error.

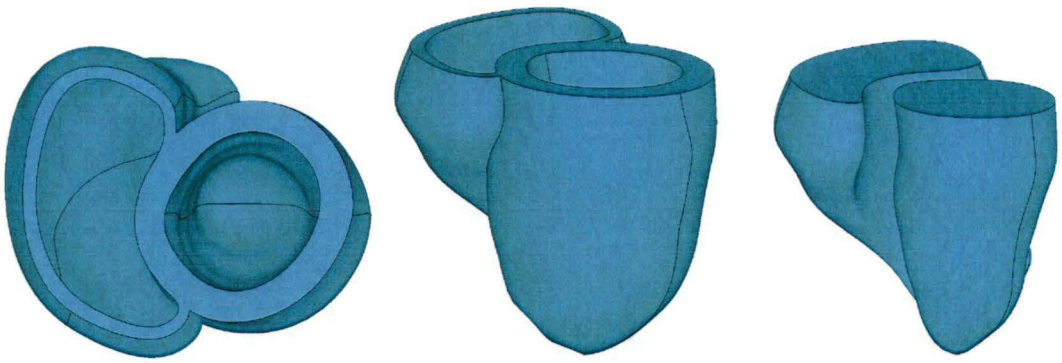

Figure 4.2.2: Tagged MRI based end diastole geometry. From left: view from base of heart myocardium, heart myocardium, left and right ventricles.

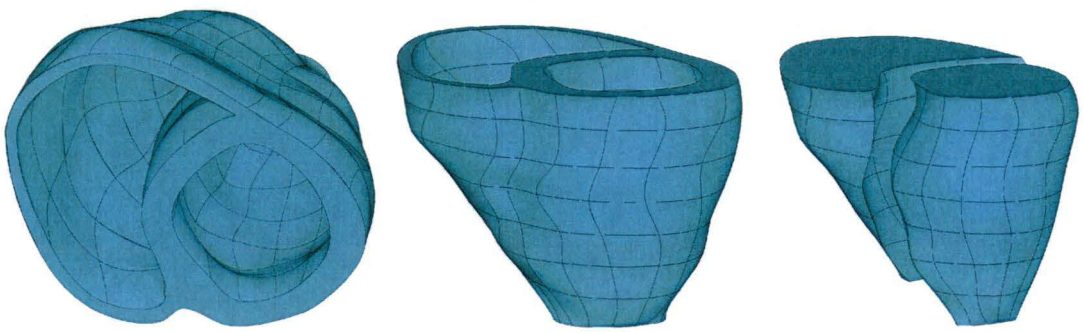

Figure 4.2.3: MRI based end diastole geometry. From left: view from base of heart myocardium, heart myocardium, left ventricle and right ventricle.

Figure 4.2.4: Simulated eight electrode catheter. Electrode spacing = 7mm, electrode width = 1mm, total length of catheter = 62mm, diameter of catheter = 2.4mm.

4.3 Results

Investigation A, B, C and D are compared in Figures 4.3.1 and Figure 4.3.2. These figures show the absolute segment voltages for a catheter in a central position in the left and right ventricles respectively for both the MRI and Tagged MRI geometry. Note: the similarity between tagged MRI and MRI model; the increase in segment voltages towards the source electrodes; the smaller difference between end systole and end diastole voltages in the right ventricle, relative to the left ventricle. The remainder of the results presented pertain to tagged MRI geometry only.

Investigation A contour plots are given in Figures 4.3.3 and 4.3.4. These figures show contour plots of voltage potential (with a constant voltage difference between the contours) at end-systole and end-diastole respectively for a catheter in the centre of the left ventricle. Note: the similarity between the end systole and end diastole figures; that the contours are perpendicular to the external surfaces of the model. Lines perpendicular to the contours indicate current flow direction. Closely spaced contours indicate relatively high potential gradient and high current density (or low conductivity). Contours indicate most current flow is through the left ventricle. Investigation B contour plots are given in Figures 4.3.5 and 4.3.6. These figures are equivalent but for a catheter in the centre of the right ventricle. Contours for the right ventricle catheter indicate relatively more current flow through the opposite ventricle.

Investigation E and F contour plots are shown in Figures 4.3.7 to 4.3.10. These figures show contour plots for catheters off centre in two approximately orthogonal planes in the left ventricle. Only the catheter positions furthest from the centre are shown. Note: the range of the offset catheters and their position relative to the myocardium in the end systole and end diastole cross sections; the blood/myocardium border marked on the top surface of the heart and its continuation through the cross sections defined by a slight abrupt change in direction of the contours. Investigation E, F and A segment voltages were transformed into the four values detailed in Section 4.2. The values for each segment in all five positions in the two planes of catheter movement are shown in Figures 4.3.11 to 4.3.14. Each figure presents one of the four values calculated from end-diastole and end-systole segment

voltages. Note: the minimum percentage change in Ves is towards the centre in Figure 4.3.11; the relative magnitude between percentage change in Ves in Figure 4.3.11 and (Ves – Ved)/Ves in Figure 4.3.12; that the minimum percentage change in (Ves – Ved) is towards the centre in Figure 4.3.13; that the minimum percentage change in (Ves – Ved)/Ves is towards the centre in Figure 4.3.14.

Investigation G and H contour plots are shown in Figures 4.3.15 to 4.3.18. These figures show contour plots for catheters off centre in two approximately orthogonal planes in the right ventricle. Only the catheter positions furthest from the centre are shown. Investigation G, H and B segment voltages were transformed into the four values detailed in Section 4.2. The values for each segment in all five positions in the two planes of catheter movement are shown in Figures 4.3.19 to 4.3.22. Each figure presents one of the four values calculated from end-diastole and end-systole segment voltages. Note similar features in these figures as Figures 4.3.11 to 4.3.14.

Investigation I contour plots are shown in Figures 4.3.23 and 4.3.24. These figures show contour plots for a centralised catheter in the left ventricle with different blood/myocardium conductivity ratios. Contours are shown for voltages in the middle third of the voltage between source electrodes. Note: the abrupt change in contour direction at the blood/myocardium borders in the lower figures representing a ratio of 4.5 and no change in contour direction in the top figures, representing a ratio of 1; the flatter contours in the lower figures indicating less current flow into the right ventricle. Investigation I and A segment voltages were transformed into the four values detailed in Section 4.2. The values for each segment for all five blood/myocardium conductivity ratios are plotted in Figures 4.3.25 to 4.3.28. Each figure presents one of the four values calculated from end-diastole and end-systole segment voltages. Note: the moderate increase in percentage change in Ves with ratio in Figure 4.3.25; the change is minimum for segments closest to the source electrodes; (Ves – Ved)/Ves increases and converges with increasing ratio in Figure 4.3.26; lower values for the segments closest to the source electrodes; the strong increase in percentage change in (Ves – Ved) with ratio in Figure 4.3.27; that change is minimum for segments closest to the base; that the percentage change in (Ves – Ved)/Ves with ratio in Figure 4.3.28 is similar to the percentage change in (Ves – Ved) with ratio in Figure 4.3.27.

Investigation J contour plots are shown in Figures 4.3.29 and 4.3.30. These figures show contour plots for a centralised catheter in the right ventricle with different blood/myocardium conductivity ratios. Contours are shown for voltages in the middle third of the voltage between source electrodes. Investigation J and B segment voltages were transformed into the four values detailed in Section 4.2. The values for each segment for all five blood/myocardium conductivity ratios are plotted in Figures 4.3.31 to 4.3.34. Each figure presents one of the four values calculated from end-diastole and end-systole segment voltages. Note similar features in these figures as Figures 4.3.25 to 4.3.28.

The different results presented are summarised in Table 4.3.1. Data generated from models with typically 250,000 to 275,000 degrees of freedom (nodes). Studies of convergence by increased refinement of mesh indicated error on the order of 0.1% or less.

Table 4.3.1: Results Summary.

Figure	Investigation(s) (from Table 4.2.1)	Description
4.3.1	A, C	Segment voltages: bar plot of Ves and Ved
4.3.2	B, D	Segment voltages: bar plot of Ves and Ved
4.3.3	A	Distributed voltage contour plots (end systole)
4.3.4	A	Distributed voltage contour plots (end diastole)
4.3.5	B	Distributed voltage contour plots (end systole)
4.3.6	B	Distributed voltage contour plots (end diastole)
4.3.7	E	Distributed voltage contour plots (end systole)
4.3.8	E	Distributed voltage contour plots (end diastole)
4.3.9	F	Distributed voltage contour plots (end systole)
4.3.10	F	Distributed voltage contour plots (end diastole)
4.3.11	E, F, A	Segment voltages: % change in Ves
4.3.12	E, F, A	Segment voltages: (Ves – Ved) / Ves
4.3.13	E, F, A	Segment voltages: % change in (Ves – Ved)
4.3.14	E, F, A	Segment voltages: % change in (Ves – Ved) / Ves
4.3.15	G	Distributed voltage contour plots (end systole)
4.3.16	G	Distributed voltage contour plots (end diastole)
4.3.17	H	Distributed voltage contour plots (end systole)
4.3.18	H	Distributed voltage contour plots (end diastole)
4.3.19	G, H, B	Segment voltages: % change in Ves
4.3.20	G, H, B	Segment voltages: (Ves – Ved) / Ves
4.3.21	G, H, B	Segment voltages: % change in (Ves – Ved)
4.3.22	G, H, B	Segment voltages: % change in (Ves – Ved) / Ves
4.3.23	I	Distributed voltage contour plots (end systole)
4.3.24	I	Distributed voltage contour plots (end diastole)
4.3.25	I, A	Segment voltages: % change in Ves
4.3.26	I, A	Segment voltages: (Ves – Ved) / Ves
4.3.27	I, A	Segment voltages: % change in (Ves – Ved)
4.3.28	I, A	Segment voltages: % change in (Ves – Ved) / Ves
4.3.29	J	Distributed voltage contour plots (end systole)
4.3.30	J	Distributed voltage contour plots (end diastole)
4.3.31	J, B	Segment voltages: % change in Ves
4.3.32	J, B	Segment voltages: (Ves – Ved) / Ves
4.3.33	J, B	Segment voltages: % change in (Ves – Ved)
4.3.34	J, B	Segment voltages: % change in (Ves – Ved) / Ves

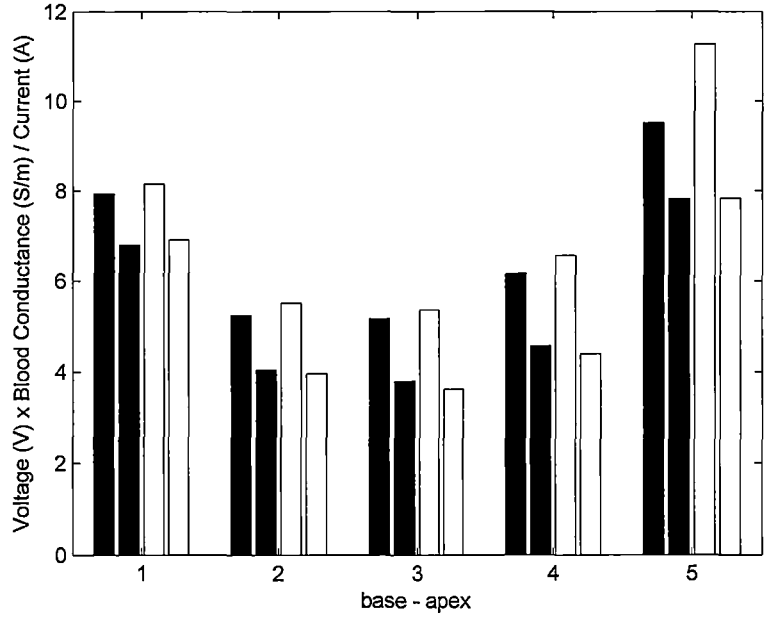

Figure 4.3.1: Absolute segment voltages in tagged MRI model (black) and MRI model (white) for catheter in left ventricle. Larger voltages are end systole, smaller voltages are end diastole. See Figure 4.3.3 and Figure 4.3.4 for position of catheter. Blood conductivity/myocardium conductivity = 2.75.

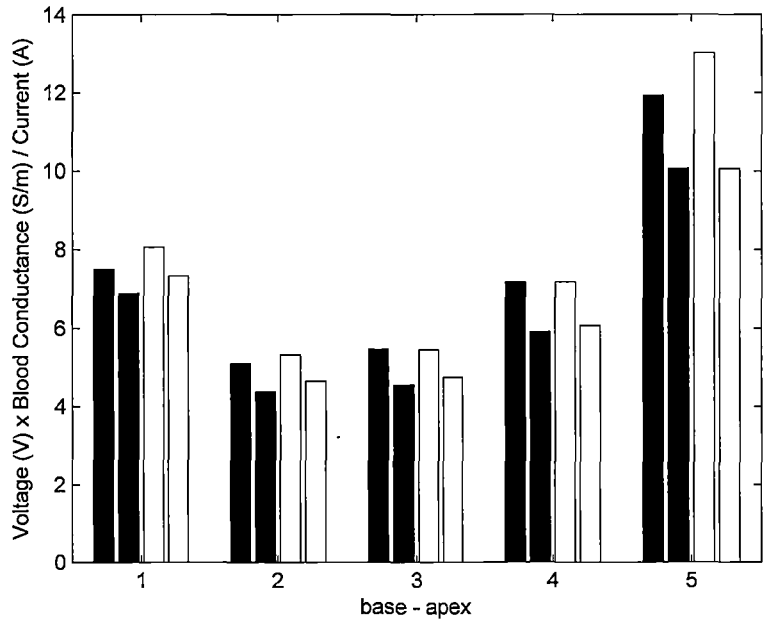

Figure 4.3.2: Absolute segment voltages in tagged MRI model (black) and MRI model (white) for catheter in right ventricle. Larger voltages are end systole, smaller voltages are end diastole. See Figure 4.3.5 and Figure 4.3.6 for position of catheter. Blood conductivity/myocardium conductivity = 2.75.

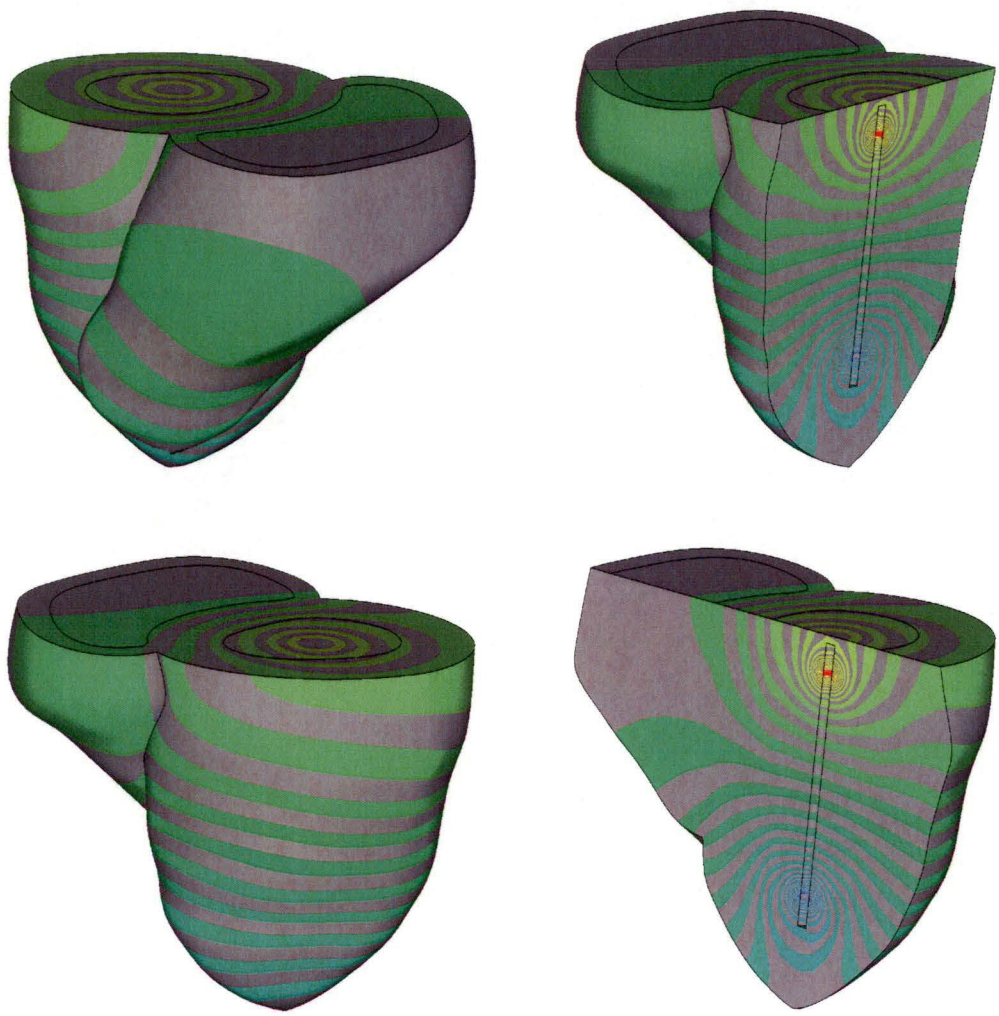

Figure 4.3.3: Left ventricle catheter voltage contours in tagged MRI model at end systole for blood conductivity/myocardium conductivity = 2.75.

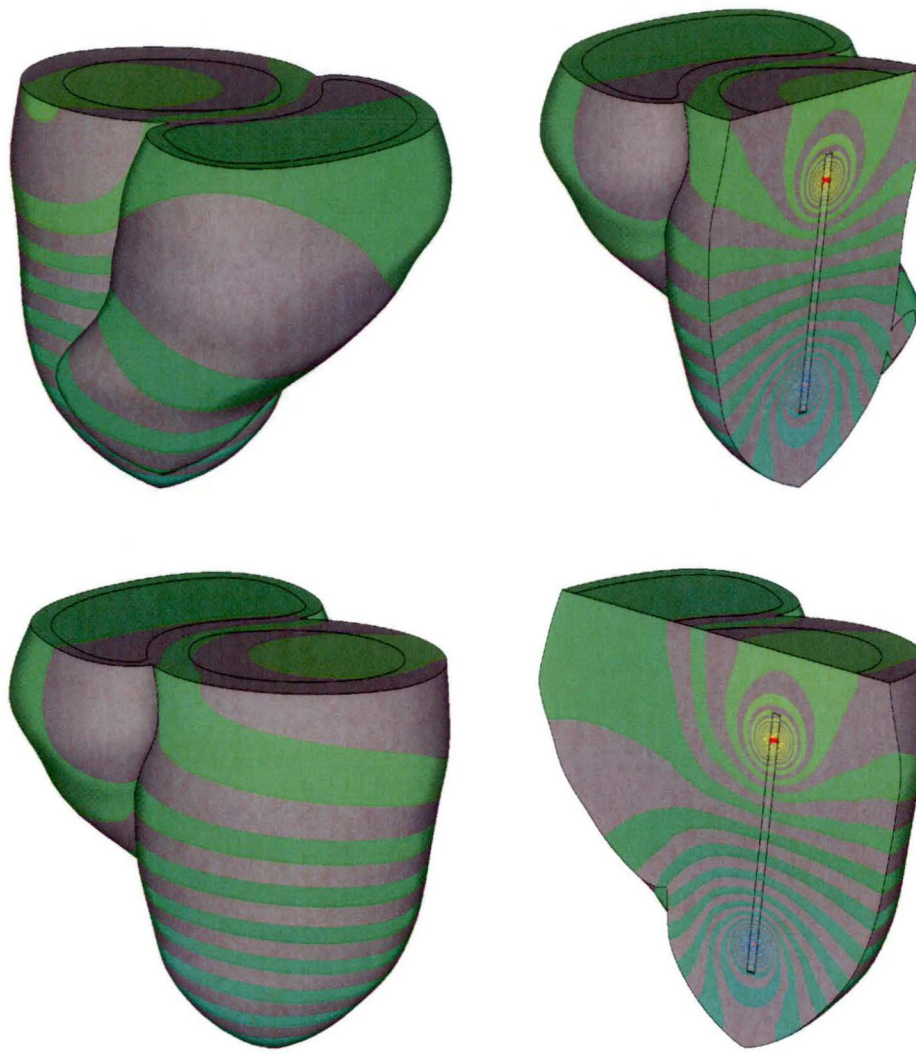

Figure 4.3.4: Left ventricle catheter voltage contours in tagged MRI model at end diastole for blood conductivity/myocardium conductivity = 2.75.

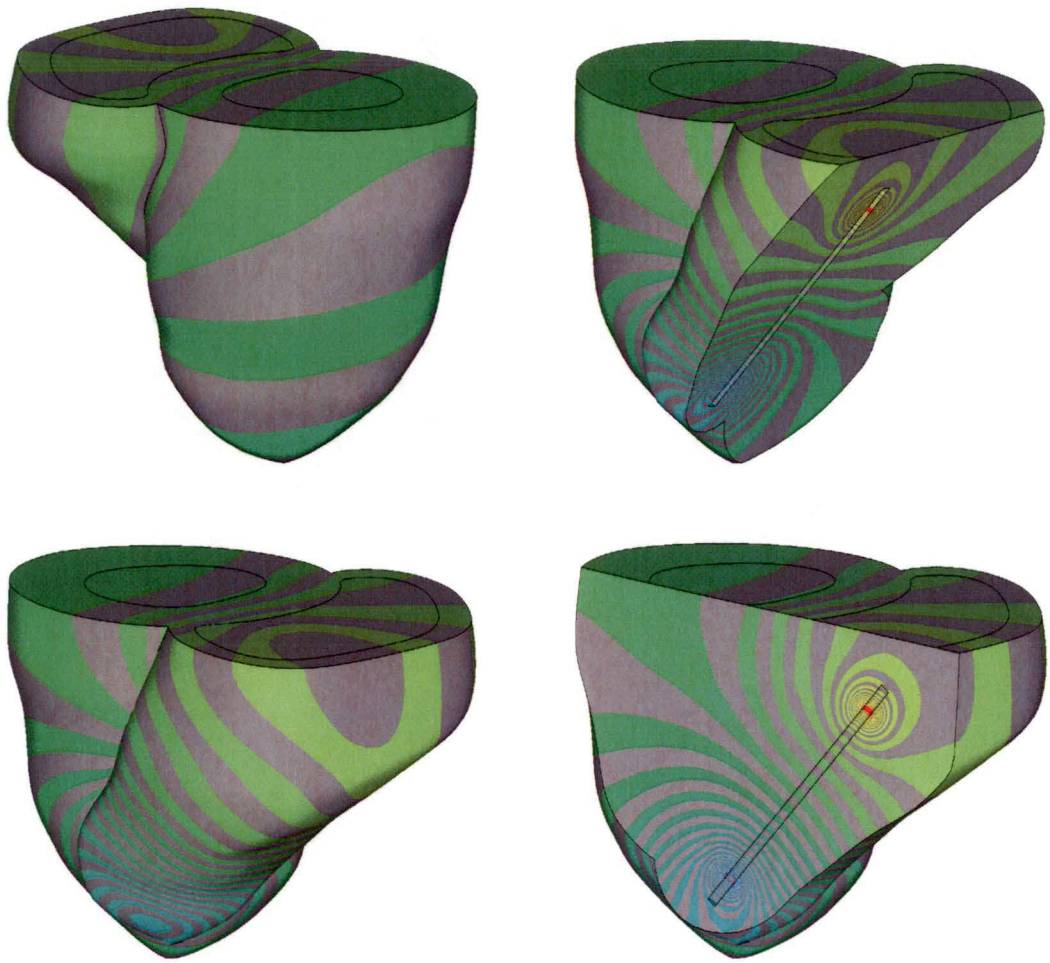

Figure 4.3.5: Right ventricle catheter voltage contours in tagged MRI model at end systole for blood conductivity/myocardium conductivity = 2.75.

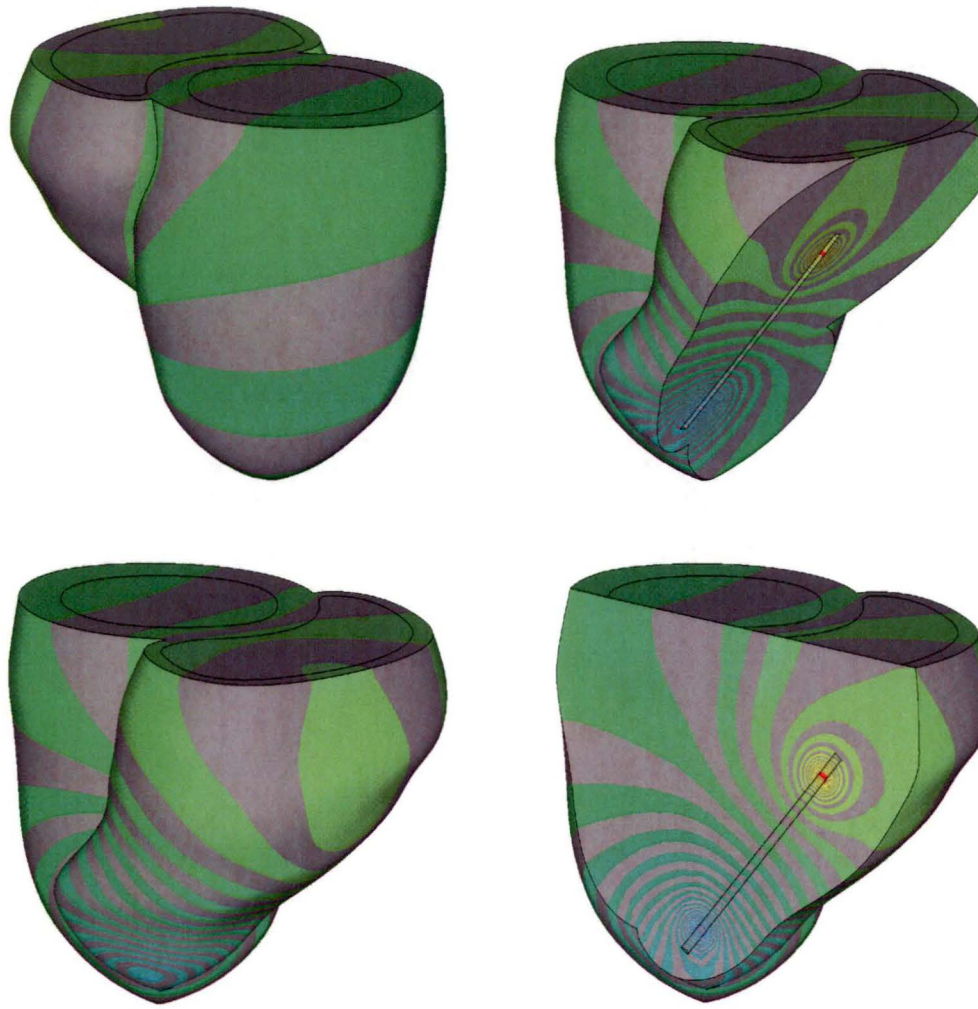

Figure 4.3.6: Right ventricle catheter voltage contours in tagged MRI model at end diastole for blood conductivity/myocardium conductivity = 2.75.

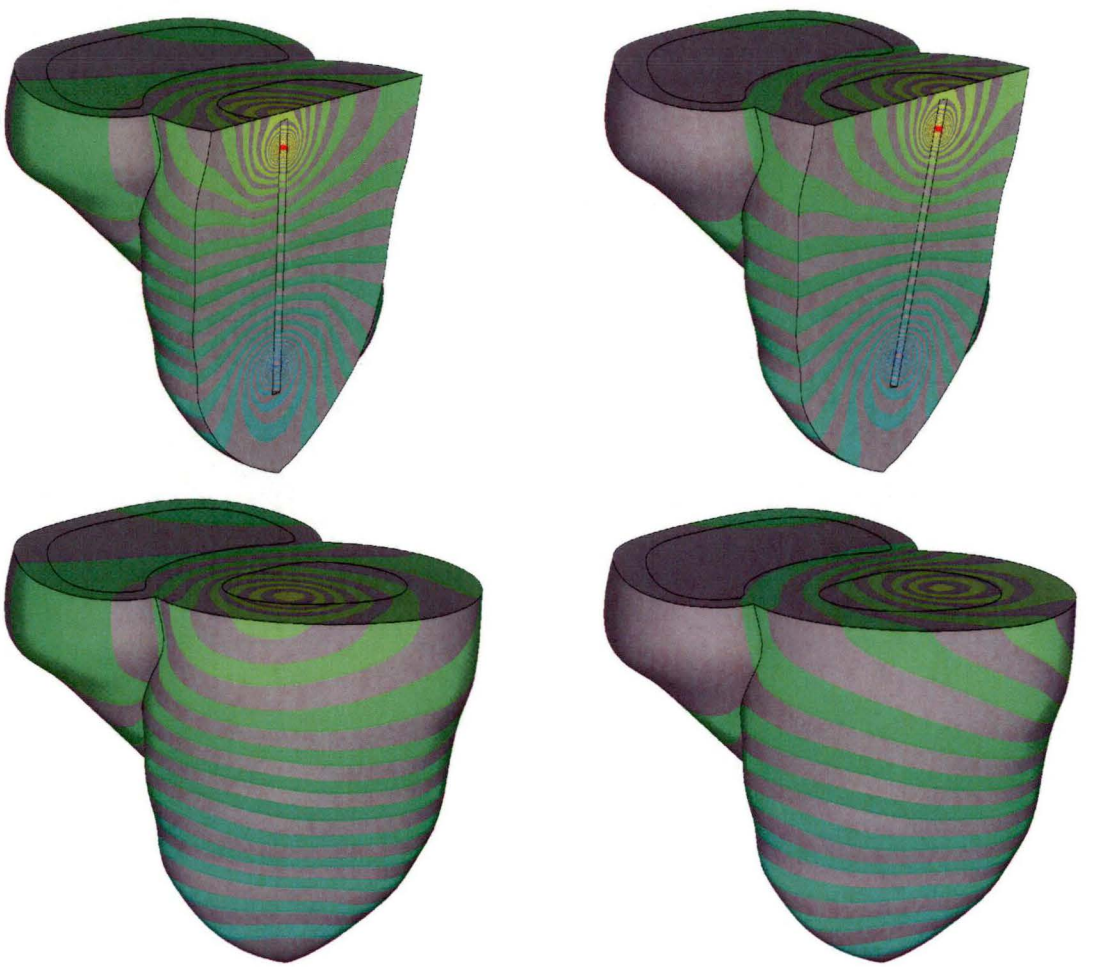

Figure 4.3.7: Off centre (pulmonary artery - liver direction) left ventricle catheter voltage contours in tagged MRI model at end systole for blood conductivity/myocardium conductivity = 2.75.

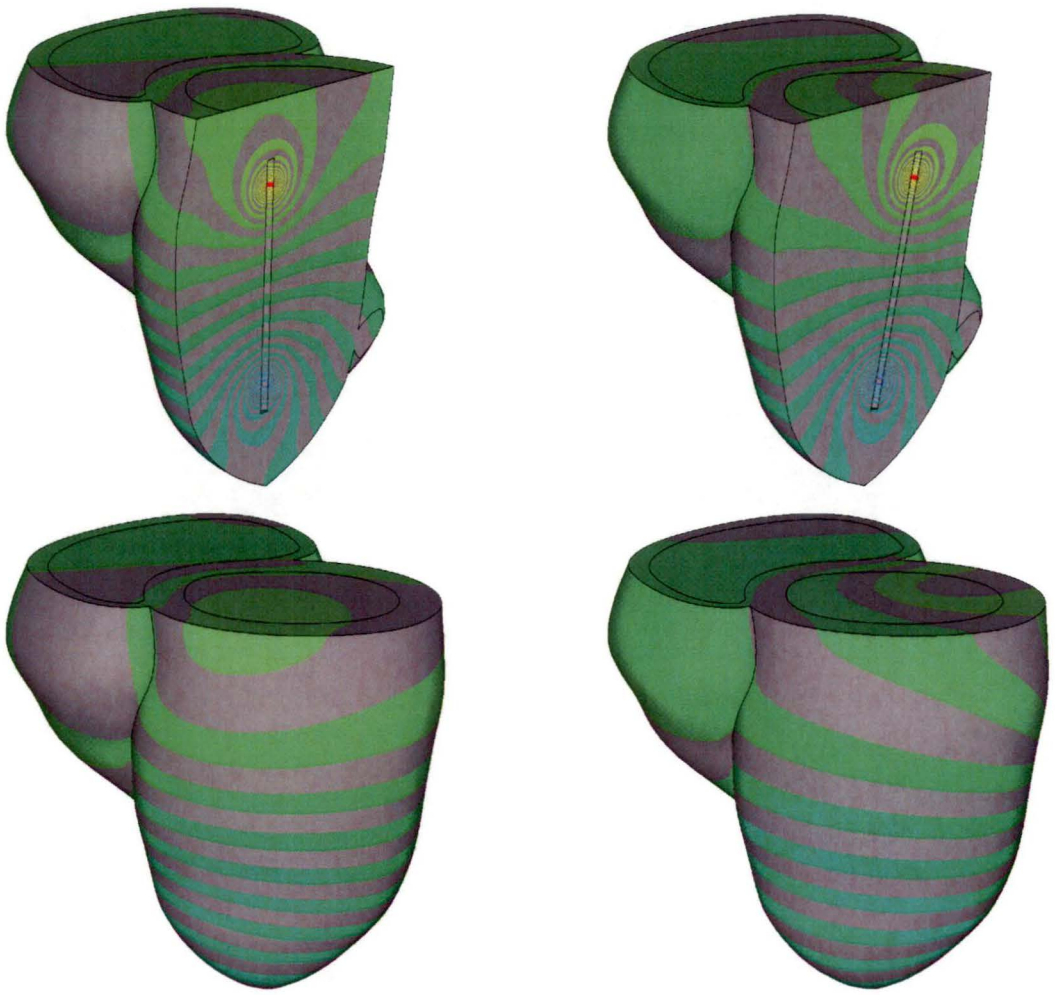

Figure 4.3.8: Off centre (pulmonary artery - liver direction) left ventricle catheter voltage contours in tagged MRI model at end diastole for blood conductivity/myocardium conductivity = 2.75.

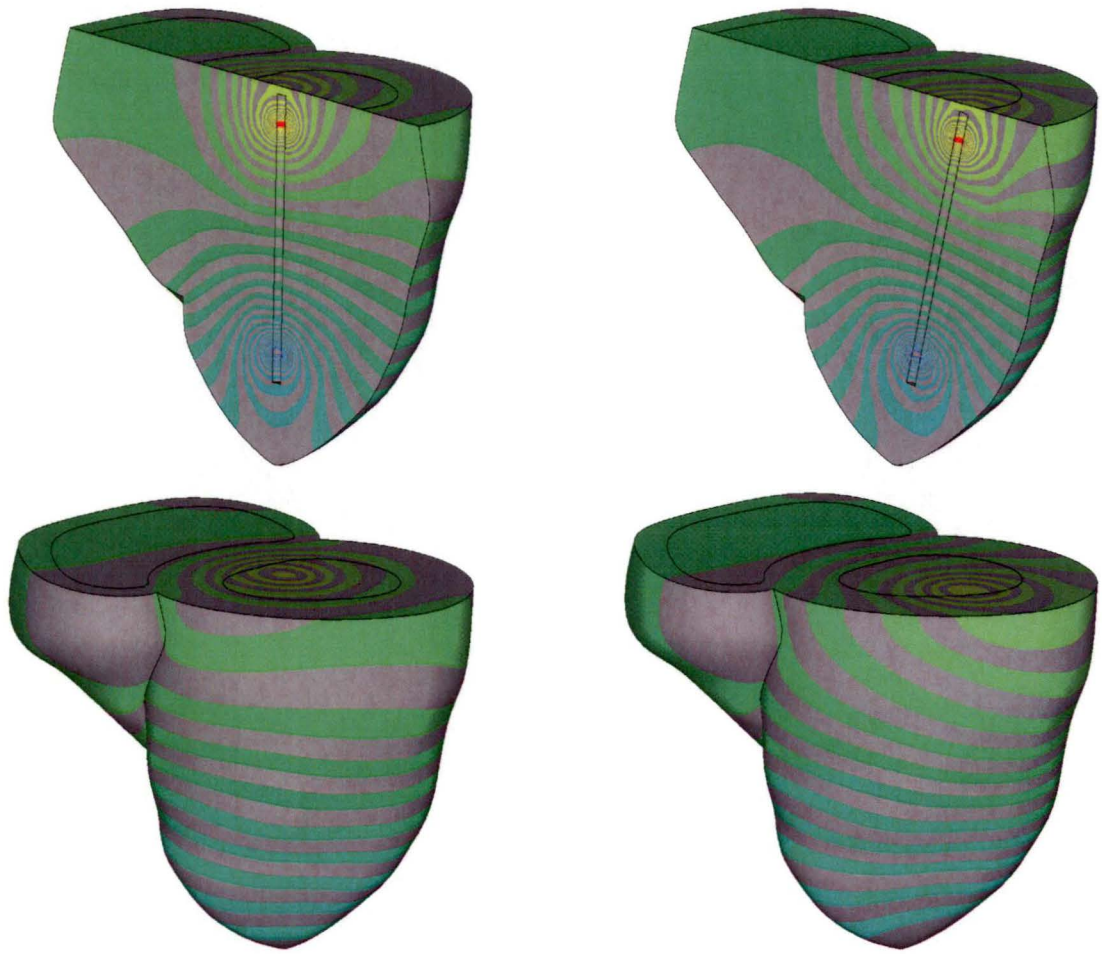

Figure 4.3.9: Off centre (septum - free wall direction) left ventricle catheter voltage contours in tagged MRI model at end systole for blood conductivity/myocardium conductivity = 2.75.

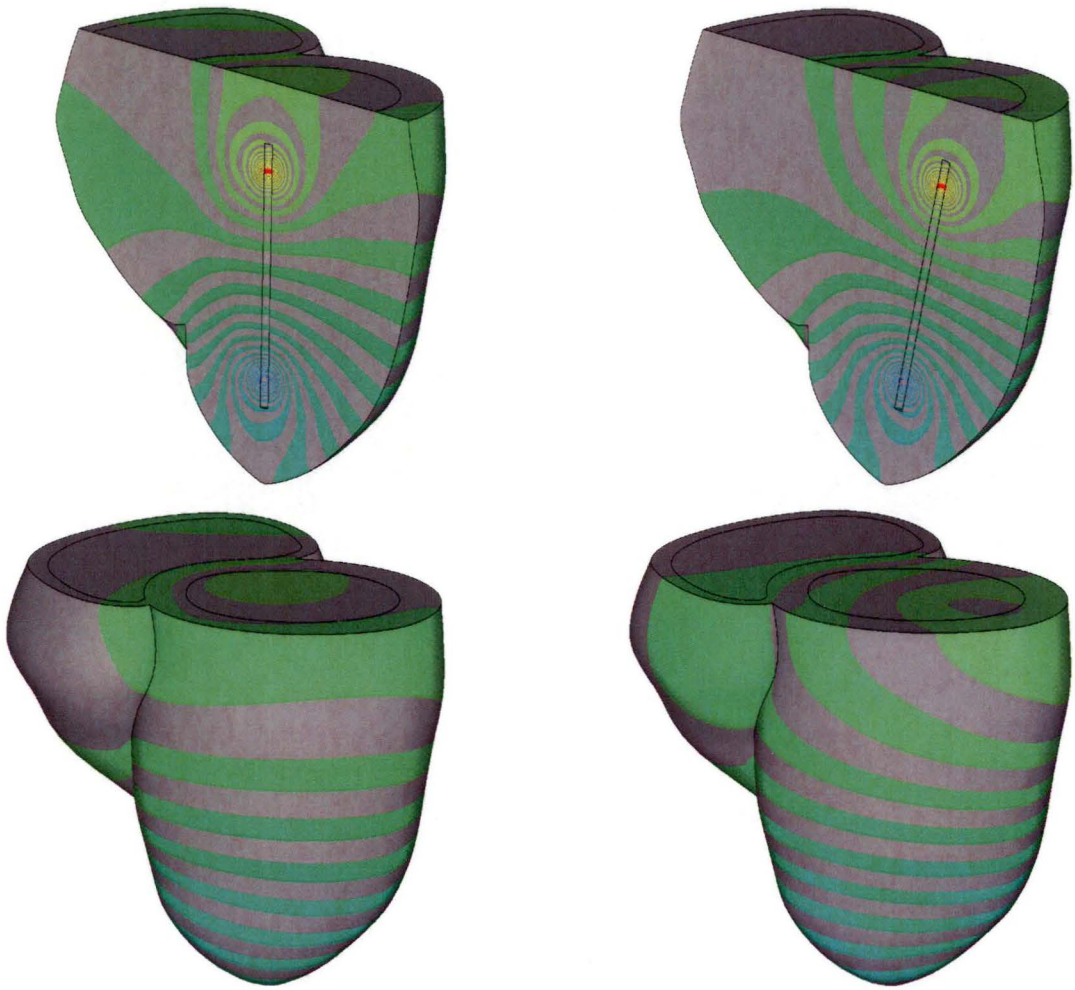

Figure 4.3.10: Off centre (septum - free wall direction) left ventricle catheter voltage contours in tagged MRI model at end diastole for blood conductivity/myocardium conductivity = 2.75.

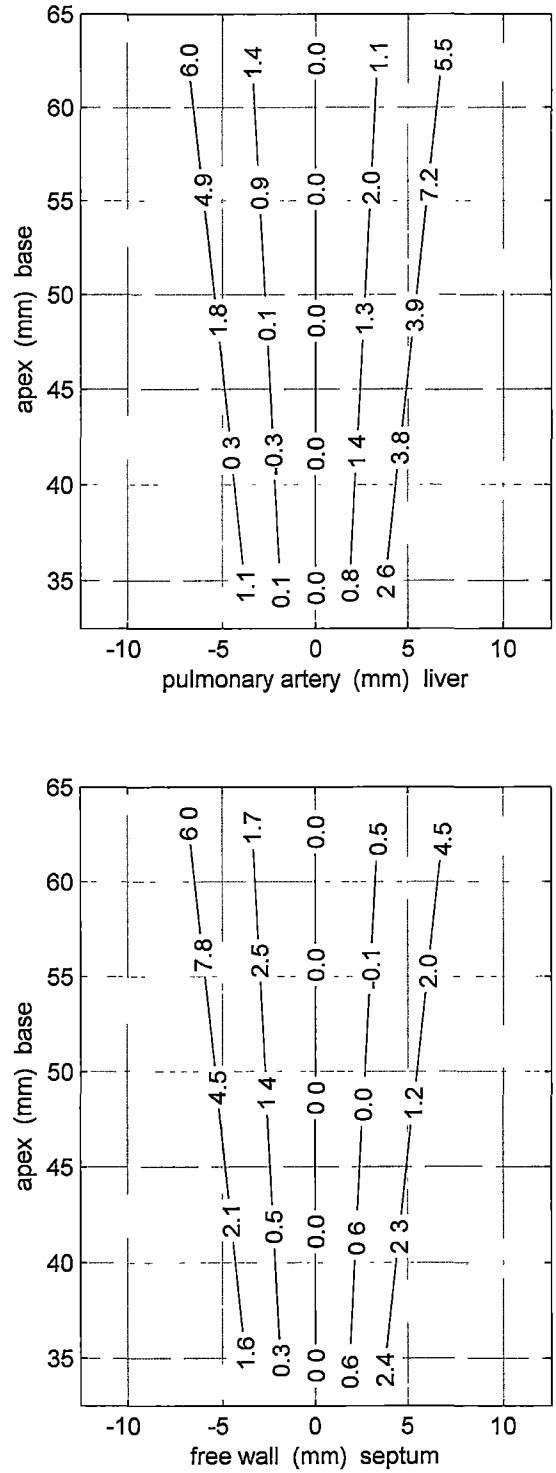

Figure 4.3.11: Percentage change in segment end systole voltage (Ves) for off centre left ventricle catheter in tagged MRI model for blood conductivity / myocardium conductivity = 2.75. Lines represent catheter axes. Centre of numbers are positioned at centre of segments. Origin of coordinate system is catheter rotation point.

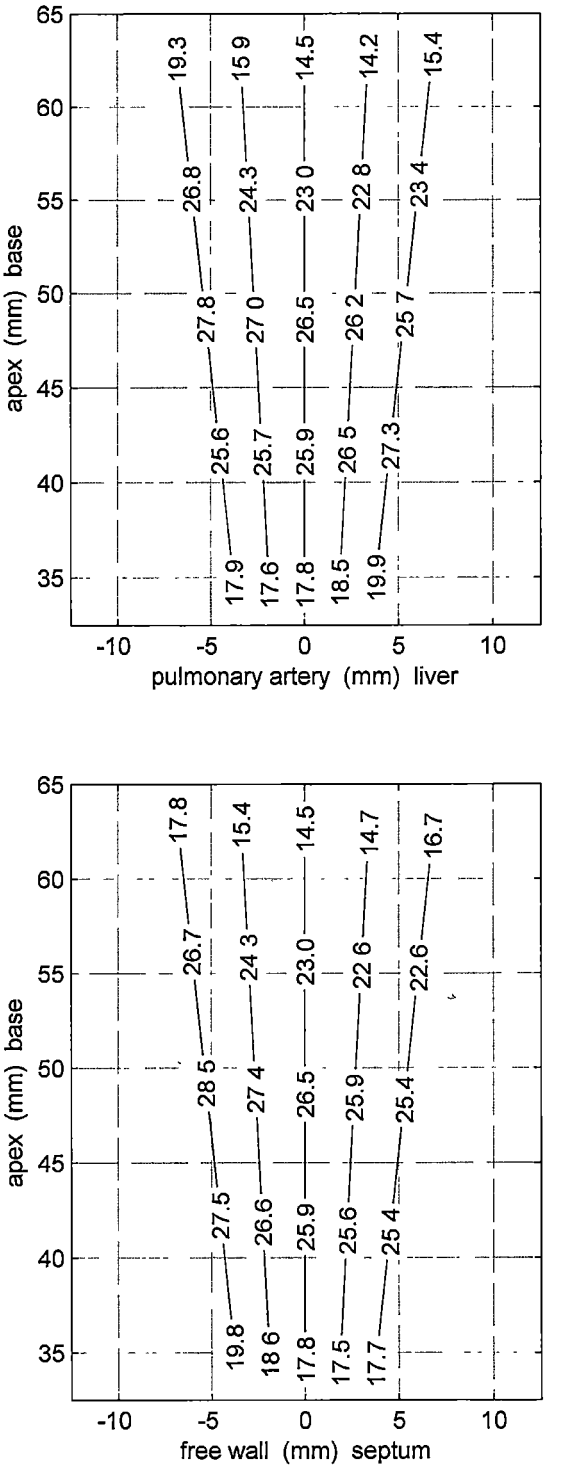

Figure 4.3.12: Percentage absolute segment (Ves – Ved) / Ves for off centre left ventricle catheter in tagged MRI model for blood conductivity / myocardium conductivity = 2.75. Lines represent catheter axes. Centre of numbers are positioned at centre of segments. Origin of coordinate system is catheter rotation point.

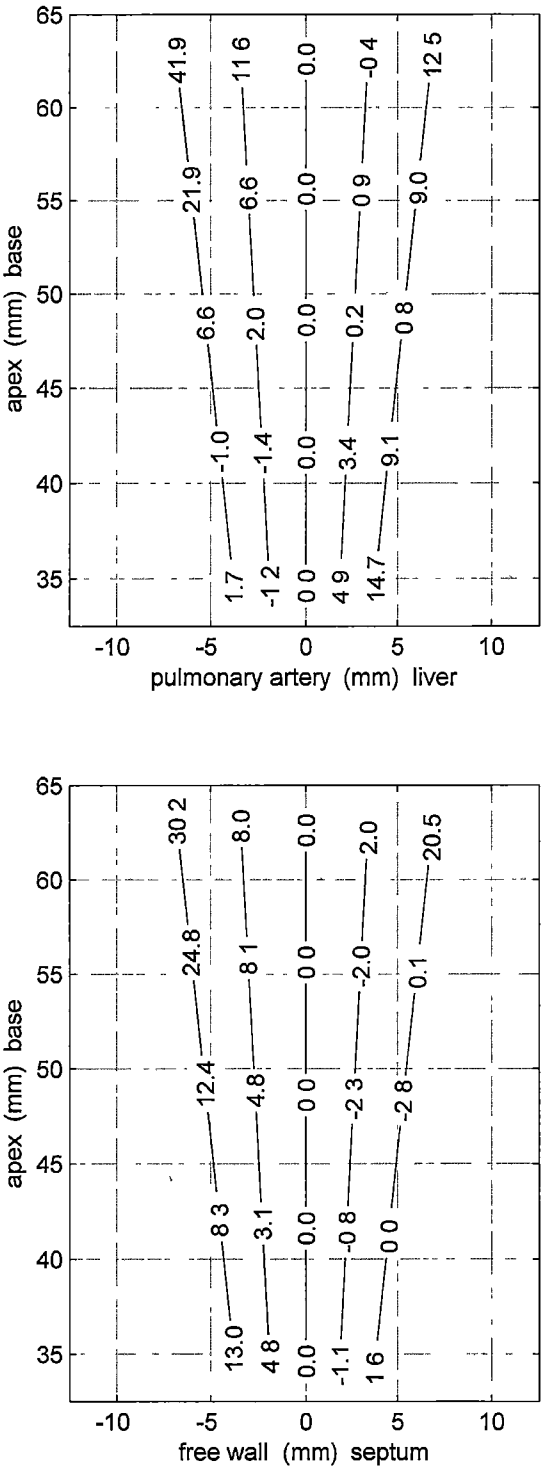

Figure 4.3.13: Percentage change in segment (Ves – Ved) for off centre left ventricle catheter in tagged MRI model for blood conductivity / myocardium conductivity = 2.75. Lines represent catheter axes. Centre of numbers are positioned at centre of segments. Origin of coordinate system is catheter rotation point.

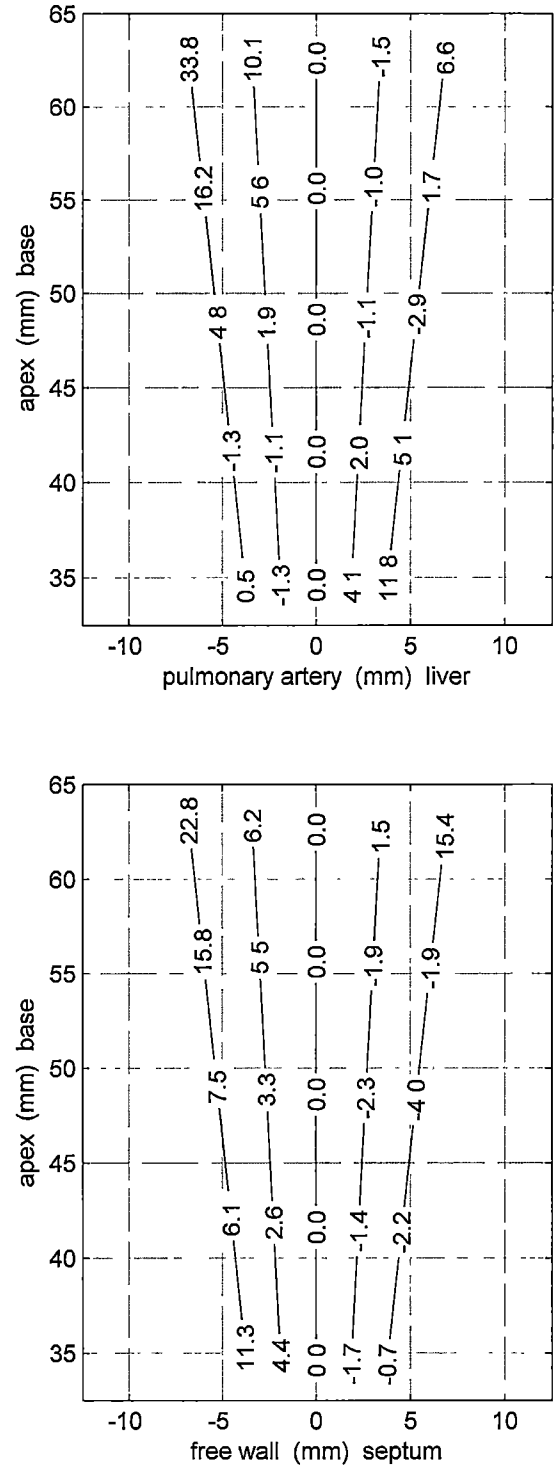

Figure 4.3.14: Percentage change in segment (Ves – Ved) / Ves for off centre left ventricle catheter in tagged MRI model for blood conductivity / myocardium conductivity = 2.75. Lines represent catheter axes. Centre of numbers are positioned at centre of segments. Origin of coordinate system is catheter rotation point.

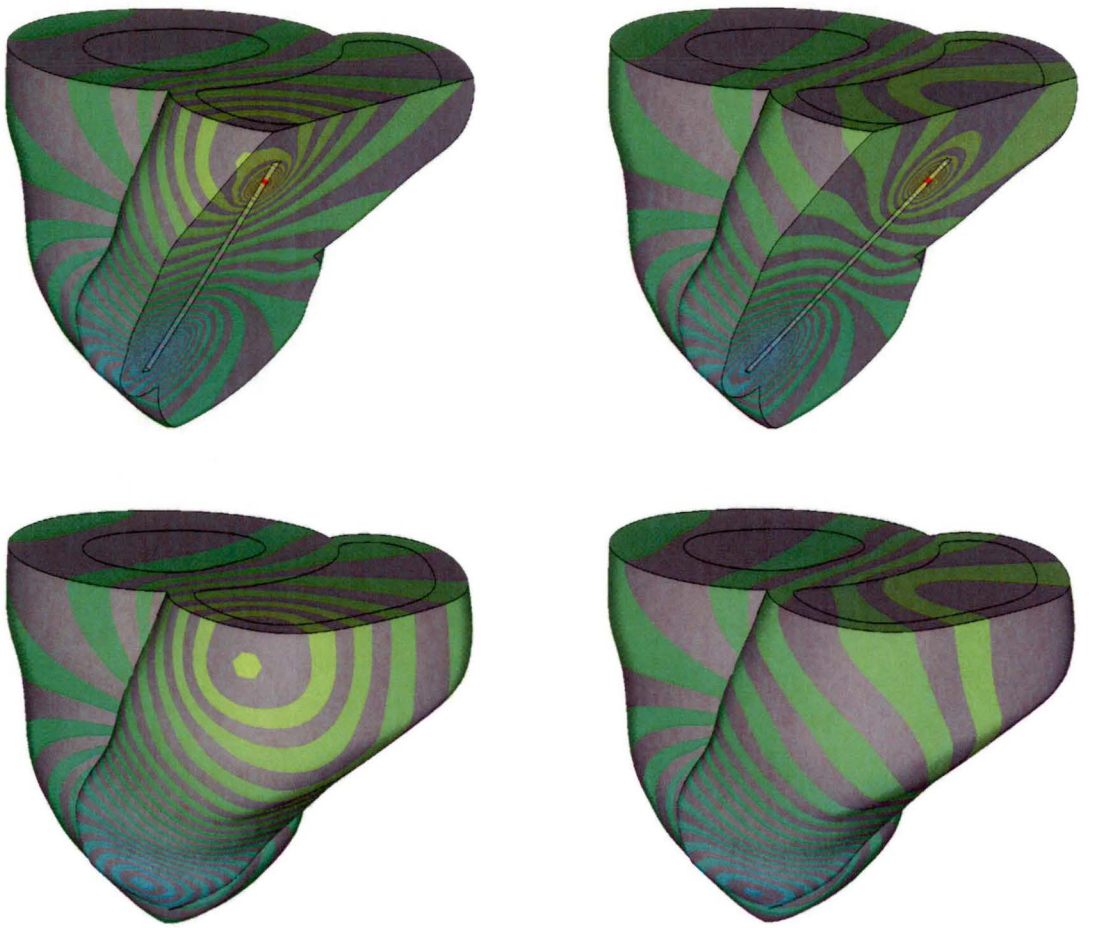

Figure 4.3.15: Off centre (liver - pulmonary artery direction) right ventricle catheter voltage contours in tagged MRI model at end systole for blood conductivity/myocardium conductivity = 2.75.

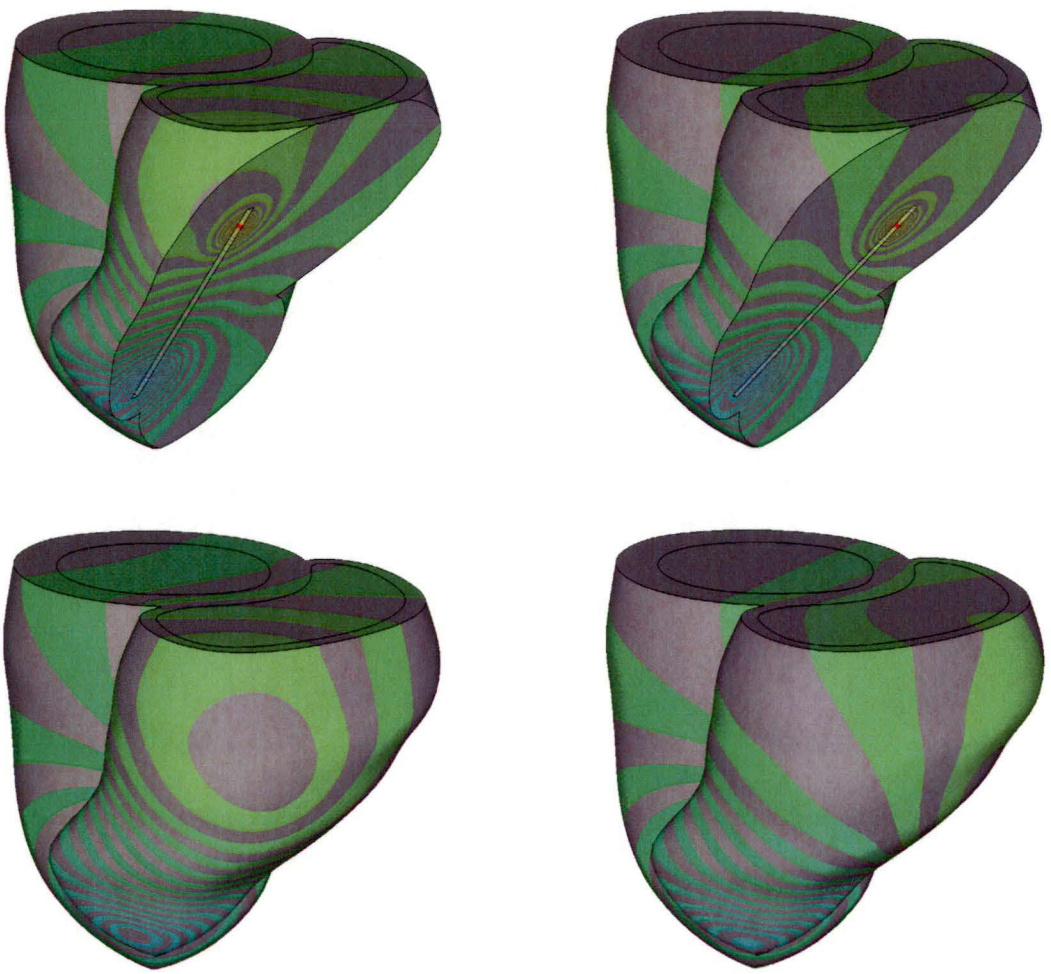

Figure 4.3.16: Off centre (liver - pulmonary artery direction) right ventricle catheter voltage contours in tagged MRI model at end diastole for blood conductivity/myocardium conductivity = 2.75.

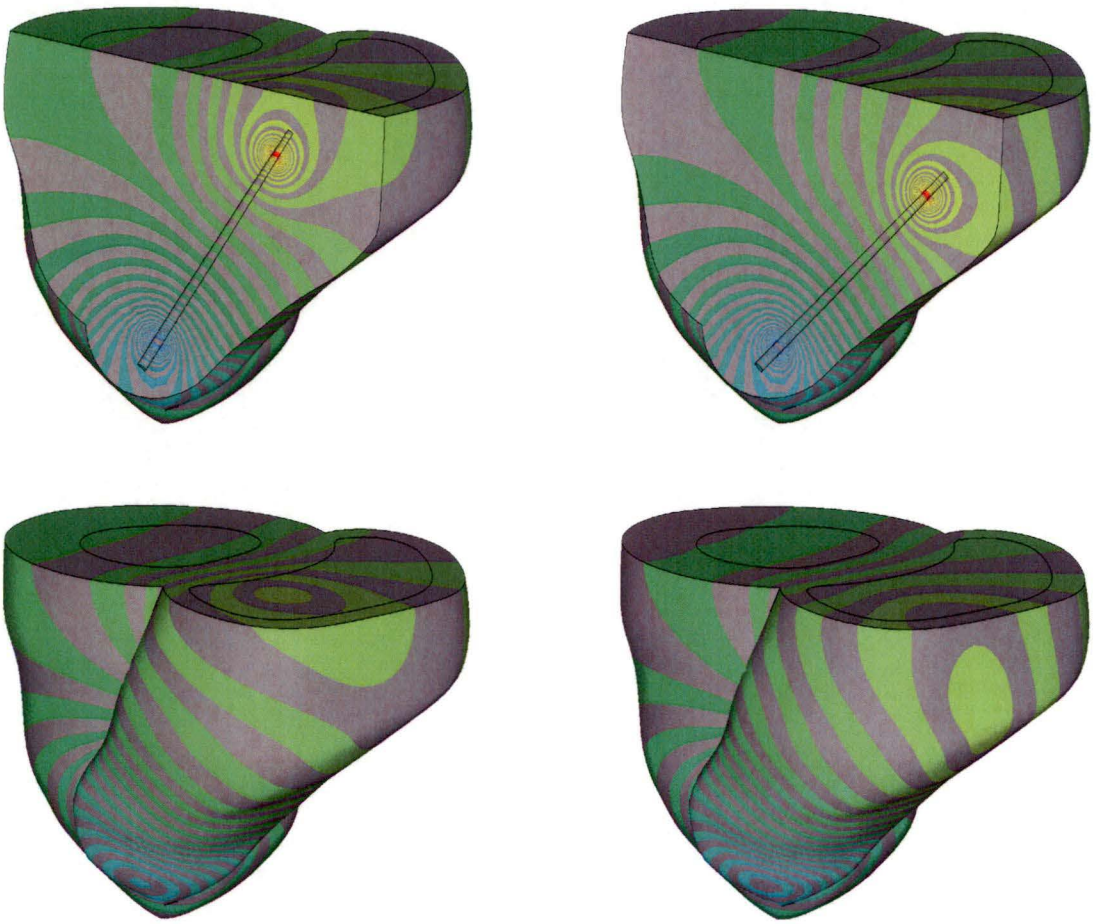

Figure 4.3.17: Off centre (septum - free wall direction) right ventricle catheter voltage contours in tagged MRI model at end systole for blood conductivity/myocardium conductivity = 2.75.

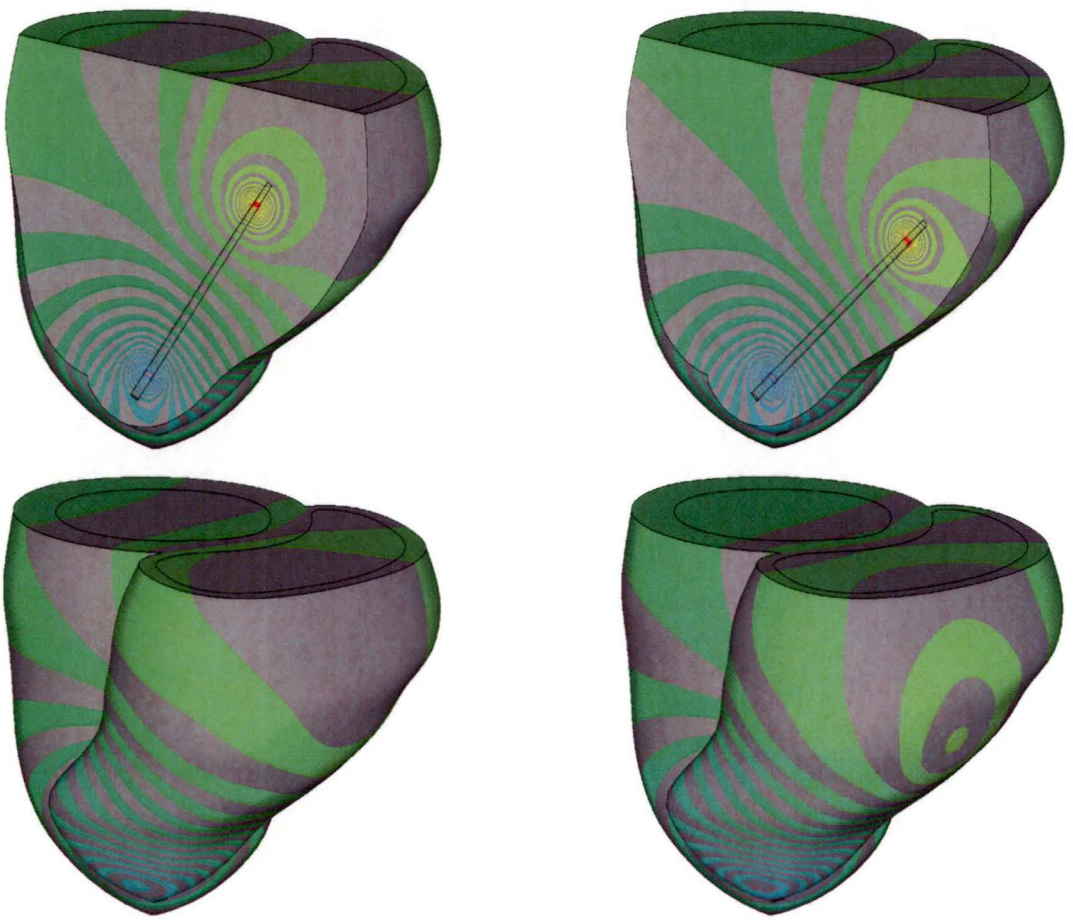

Figure 4.3.18: Off centre (septum - free wall direction) right ventricle catheter voltage contours in tagged MRI model at end diastole for blood conductivity/myocardium conductivity = 2.75.

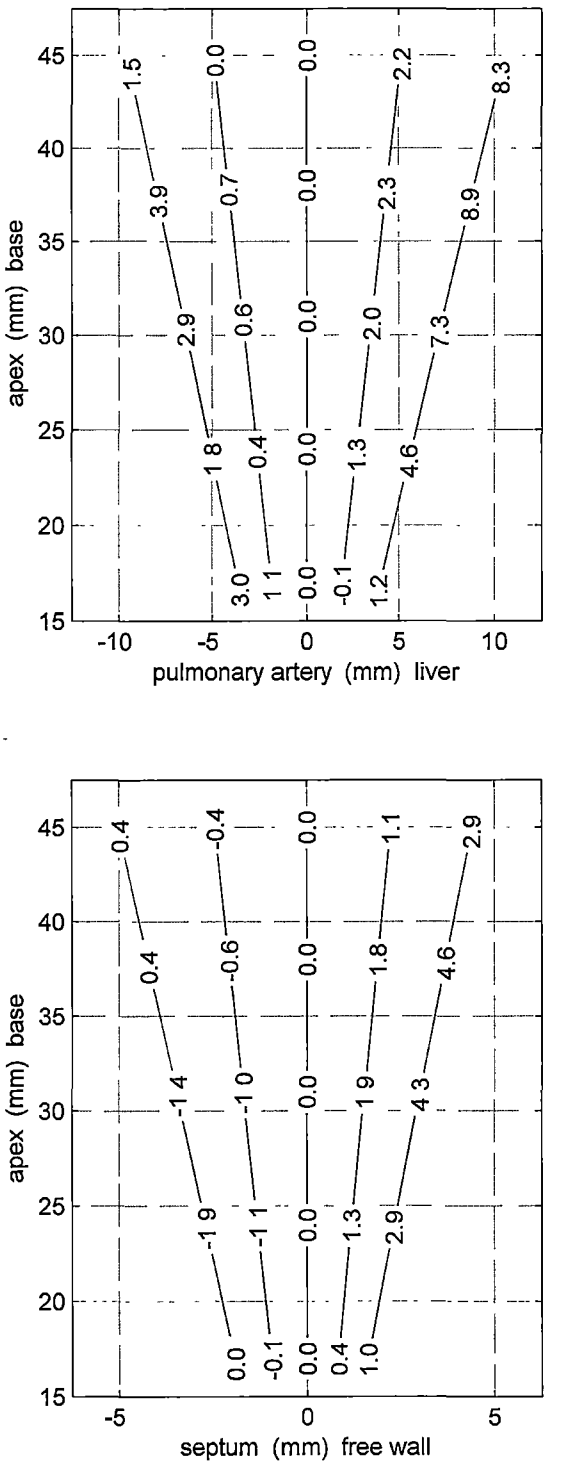

Figure 4.3.19: Percentage change in segment end systole voltage (Ves) for off centre right ventricle catheter in tagged MRI model for blood conductivity / myocardium conductivity = 2.75. Lines represent catheter axes. Centre of numbers are positioned at centre of segments. Origin of coordinate system is catheter rotation point.

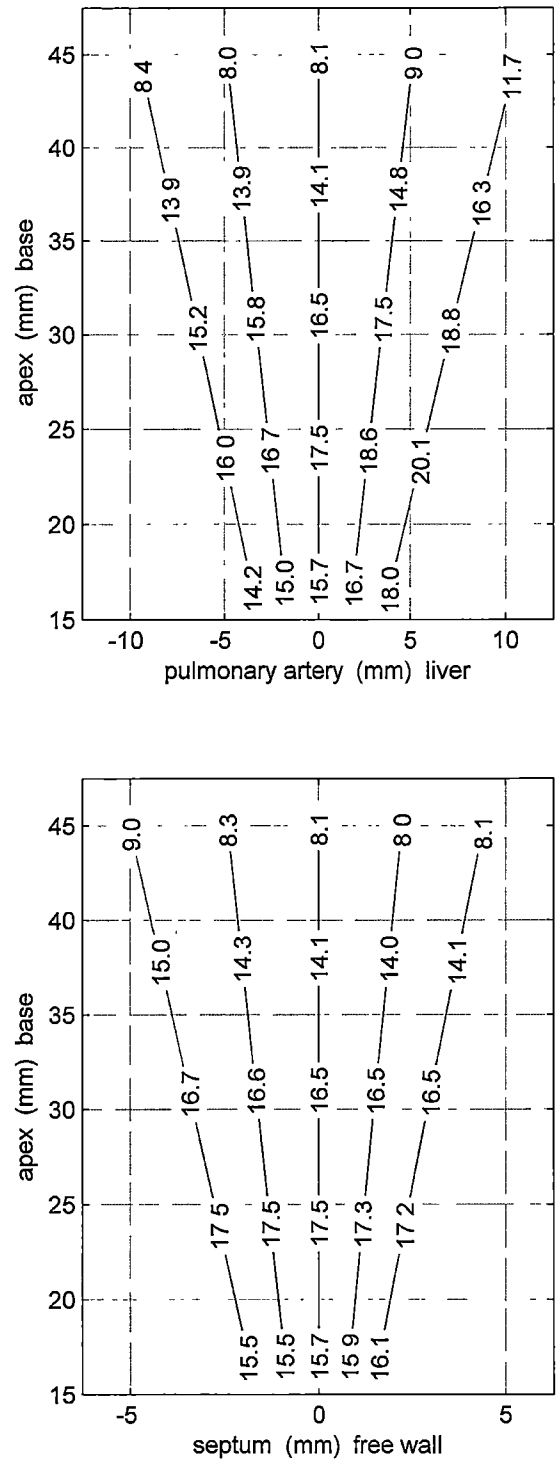

Figure 4.3.20: Percentage absolute segment (Ves – Ved) / Ves for off centre right ventricle catheter in tagged MRI model for blood conductivity / myocardium conductivity = 2.75. Lines represent catheter axes. Centre of numbers are positioned at centre of segments. Origin of coordinate system is catheter rotation point.

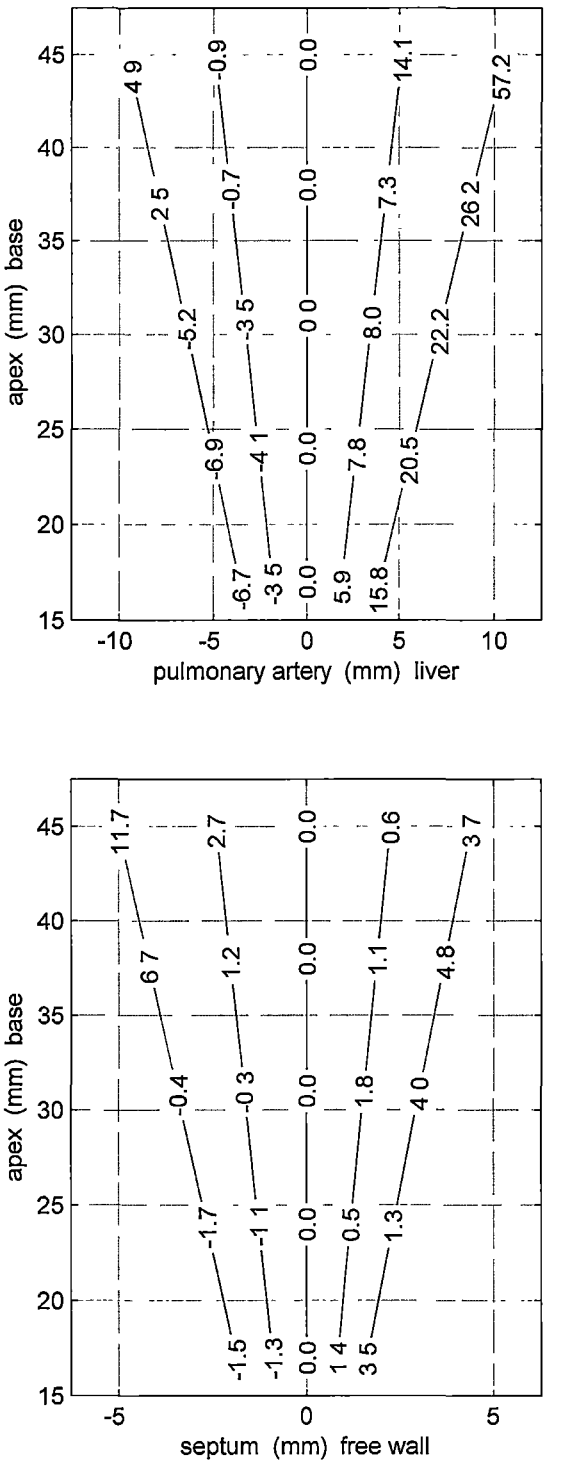

Figure 4.3.21: Percentage change in segment (Ves – Ved) for off centre right ventricle catheter in tagged MRI model for blood conductivity / myocardium conductivity = 2.75. Lines represent catheter axes. Centre of numbers are positioned at centre of segments. Origin of coordinate system is catheter rotation point.

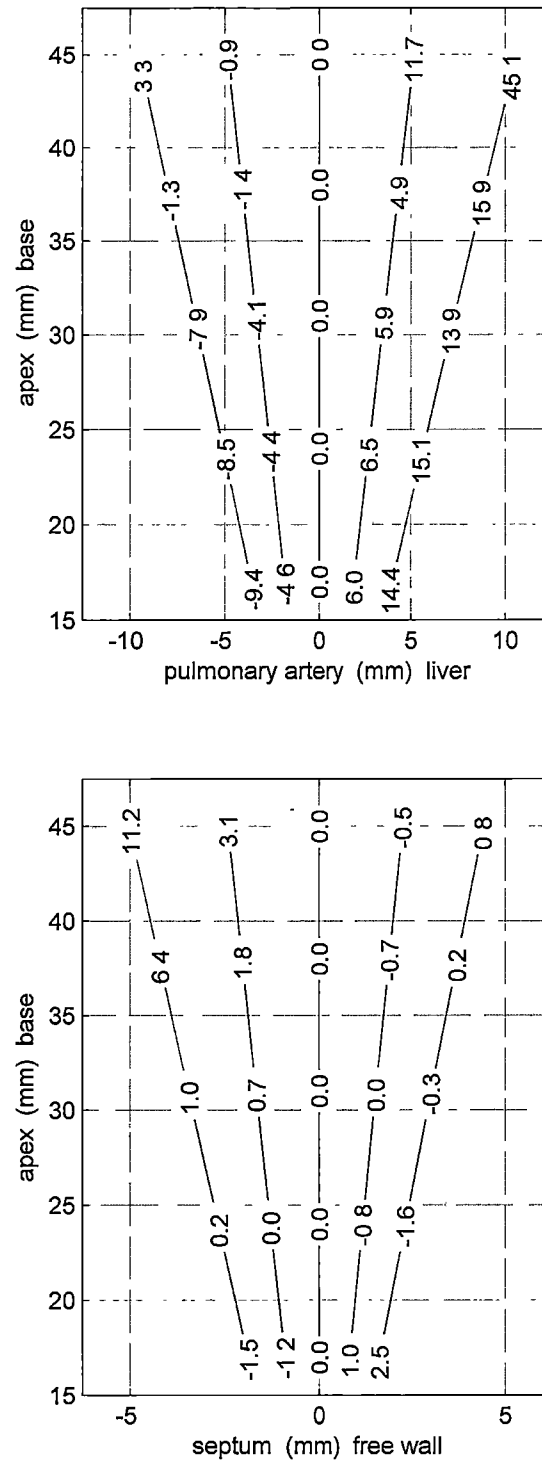

Figure 4.3.22: Percentage change in segment (Ves – Ved) / Ves for off centre right ventricle catheter in tagged MRI model for blood conductivity / myocardium conductivity = 2.75. Lines represent catheter axes. Centre of numbers are positioned at centre of segments. Origin of coordinate system is catheter rotation point.

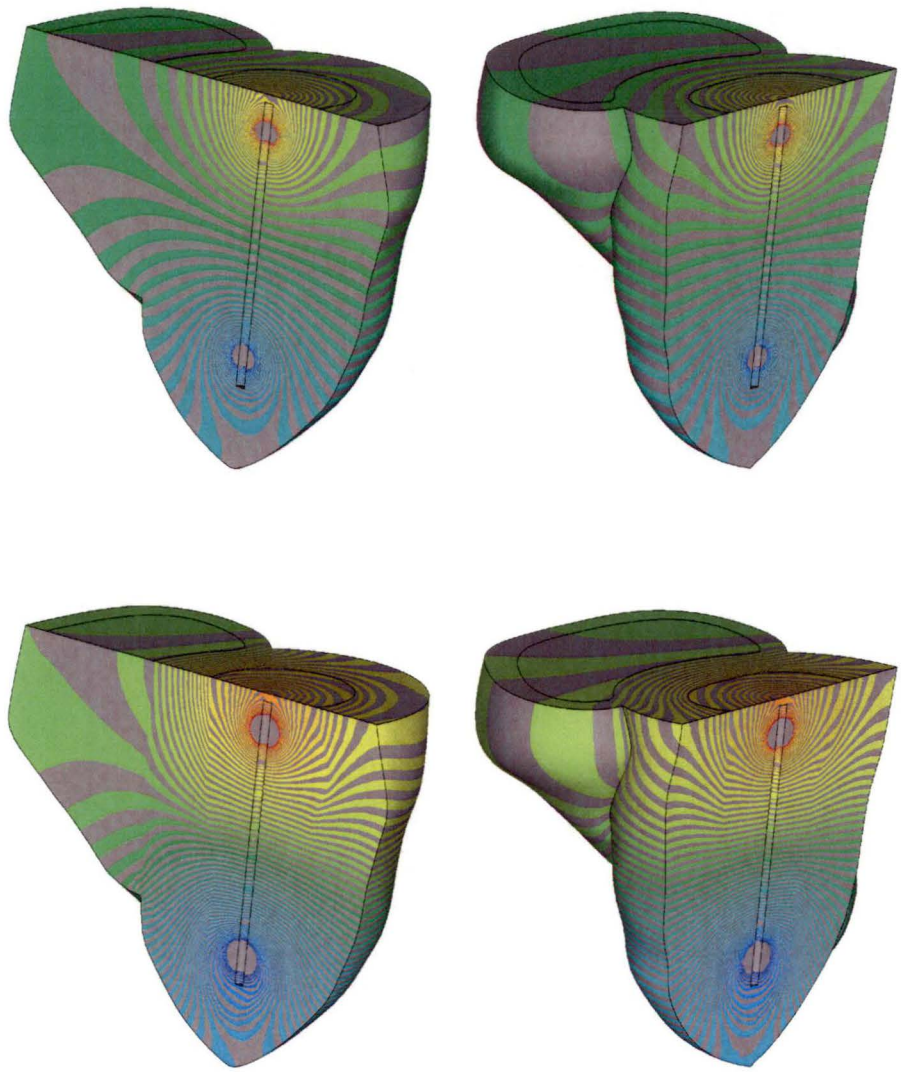

Figure 4.3.23: Left ventricle catheter voltage contours in tagged MRI model at end systole. Top: blood conductivity/myocardium conductivity = 1.0. Bottom: blood conductivity/myocardium conductivity = 4.5.

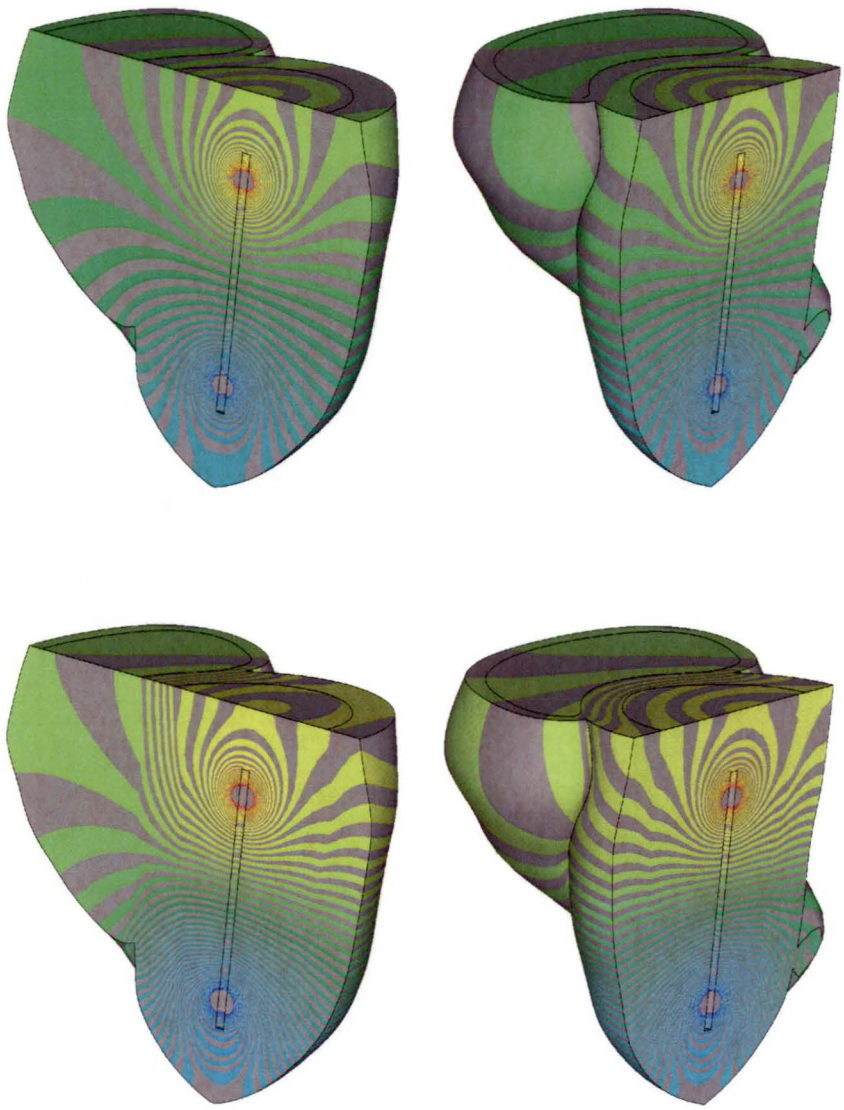

Figure 4.3.24: Left ventricle catheter voltage contours in tagged MRI model at end diastole. Top: blood conductivity/myocardium conductivity = 1.0. Bottom: blood conductivity/myocardium conductivity = 4.5.

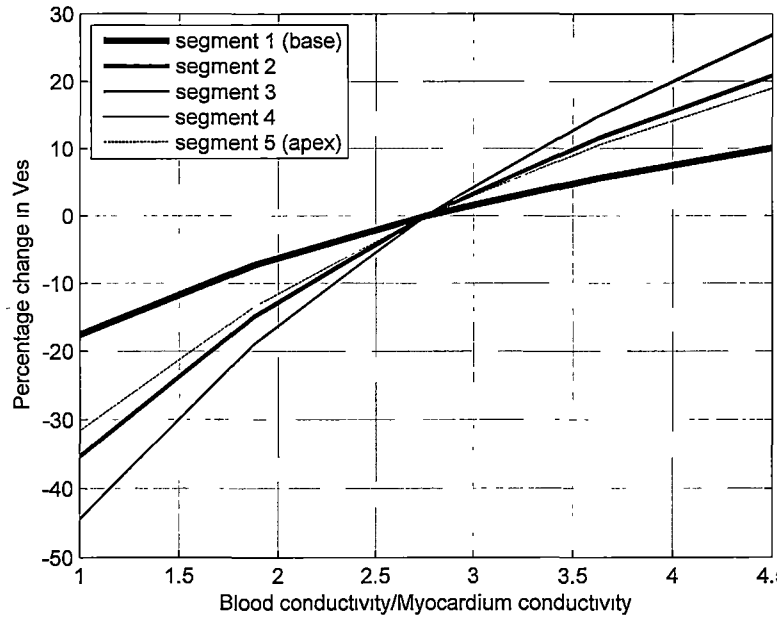

Figure 4.3.25: Percentage change in segment end systole voltage (Ves) for left ventricle catheter in tagged MRI model.

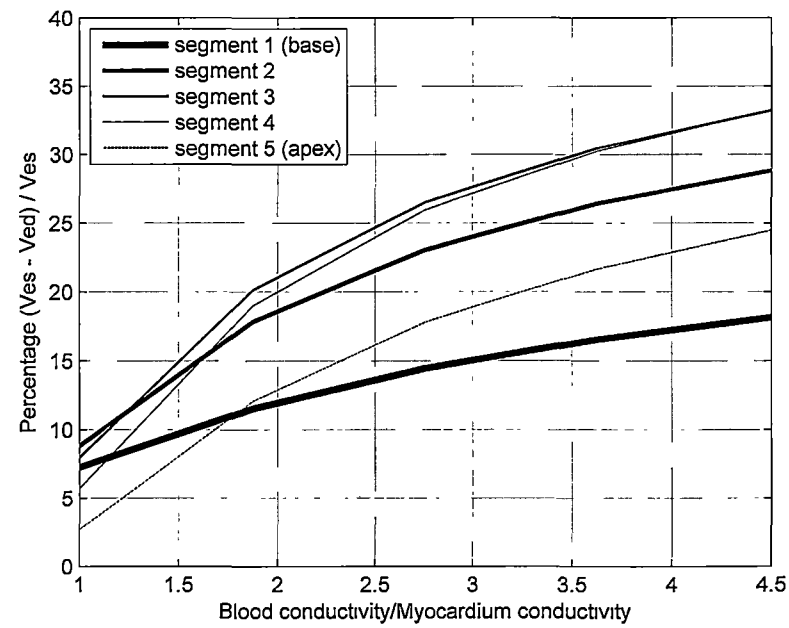

Figure 4.3.26: Percentage absolute segment (Ves – Ved) / Ves for left ventricle catheter in tagged MRI model.

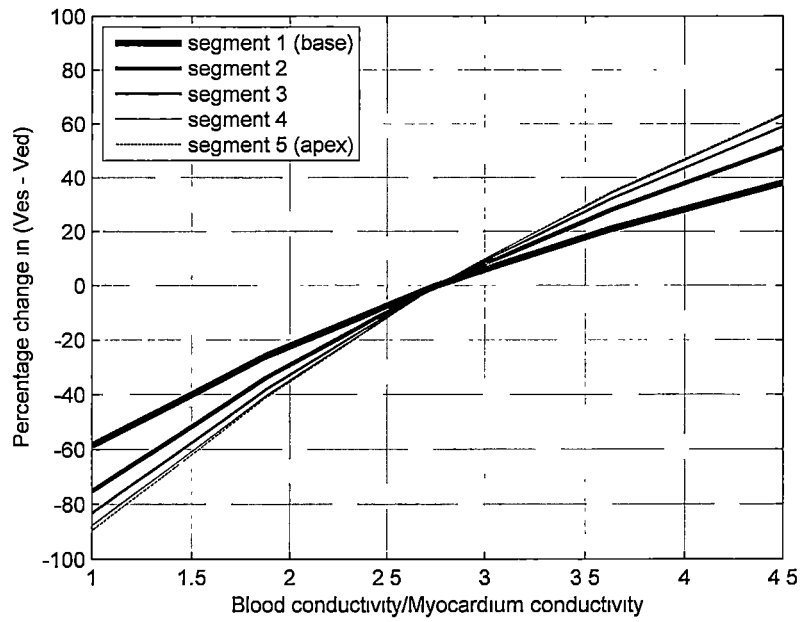

Figure 4.3.27: Percentage change in segment (Ves – Ved) for left ventricle catheter in tagged MRI model.

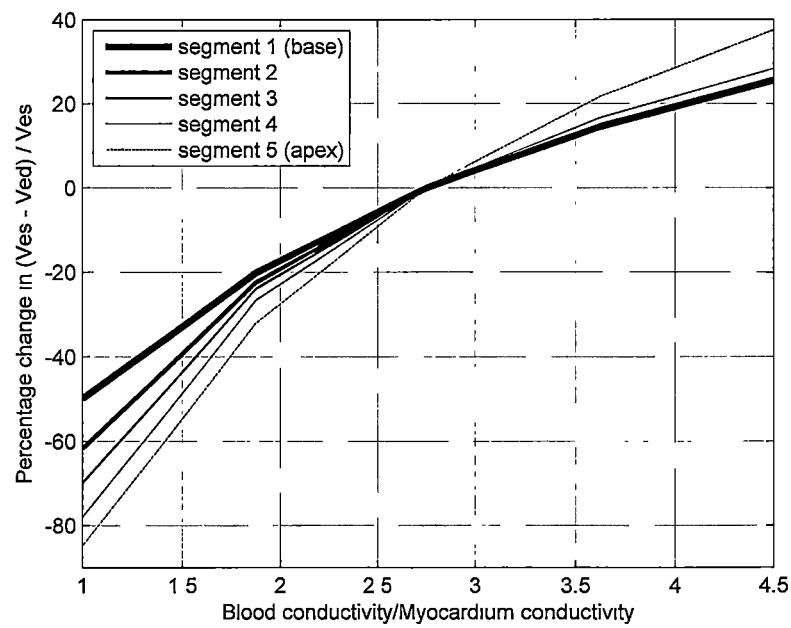

Figure 4.3.28: Percentage change in segment (Ves – Ved) / Ves for left ventricle catheter in tagged MRI model.

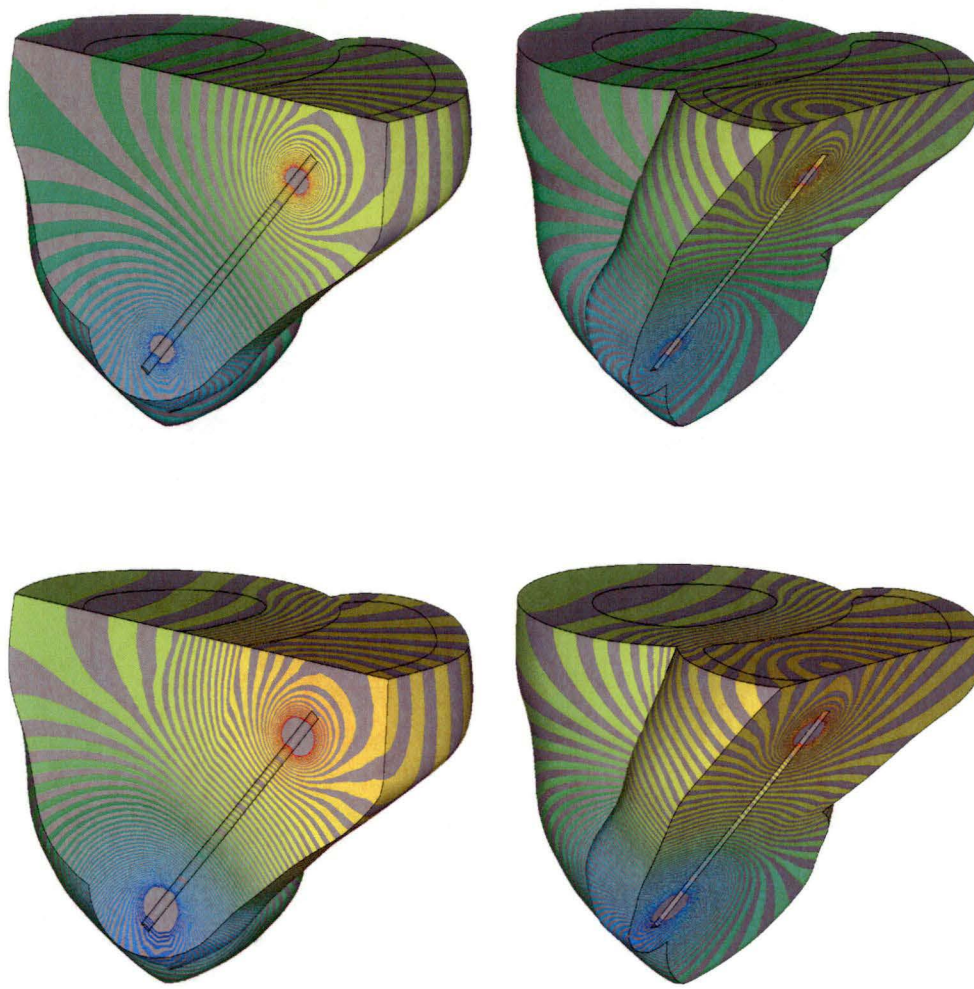

Figure 4.3.29: Right ventricle catheter voltage contours in tagged MRI model at end systole. Top: blood conductivity/myocardium conductivity = 1.0. Bottom: blood conductivity/myocardium conductivity = 4.5.

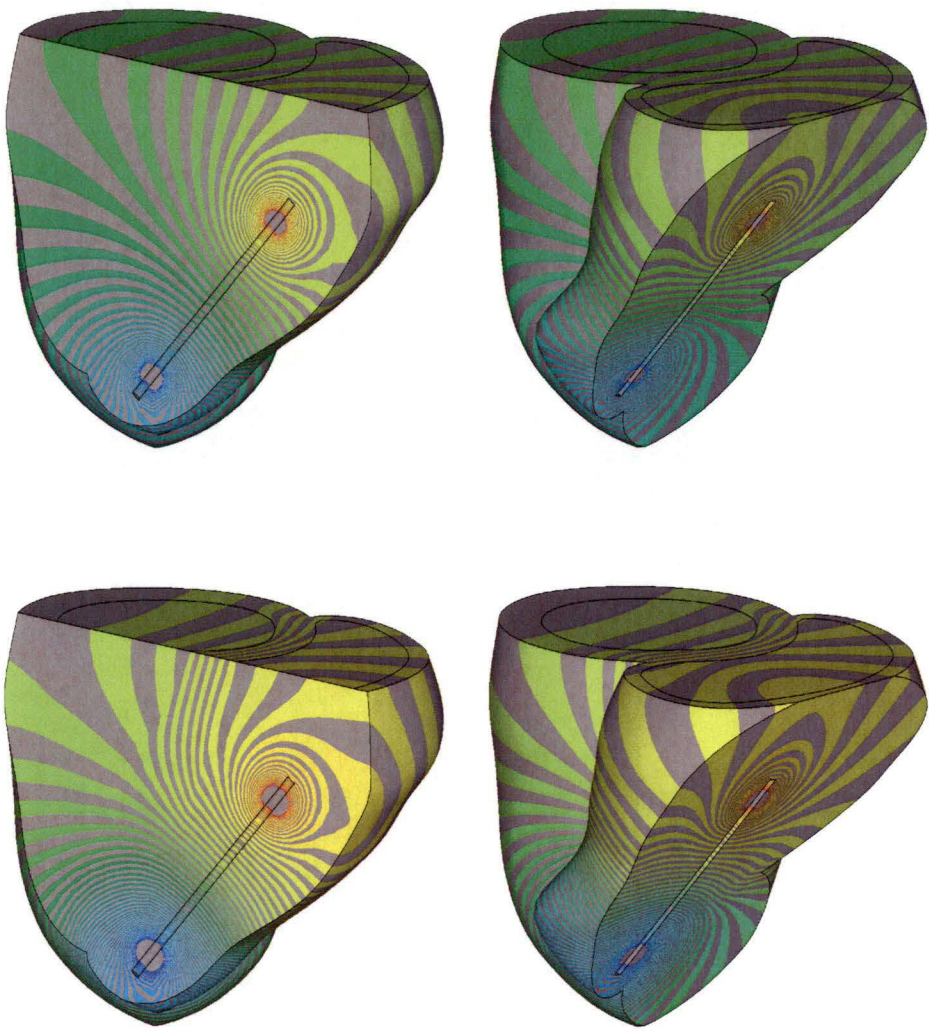

Figure 4.3.30: Right ventricle catheter voltage contours in tagged MRI model at end diastole. Top: blood conductivity/myocardium conductivity = 1.0. Bottom: blood conductivity/myocardium conductivity = 4.5.

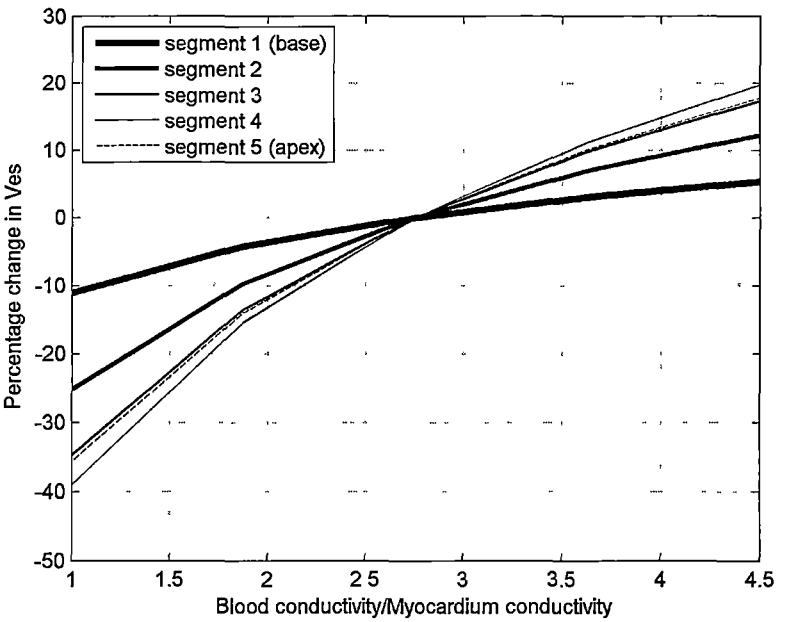

Figure 4.3.31: Percentage change in segment end systole voltage (Ves) for right ventricle catheter in tagged MRI model.

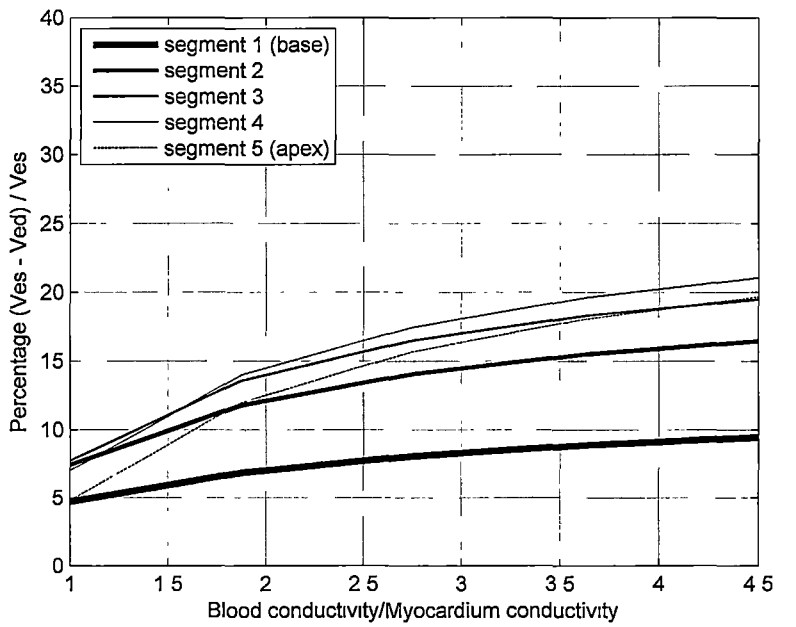

Figure 4.3.32: Percentage absolute segment (Ves – Ved) / Ves for right ventricle catheter in tagged MRI model.

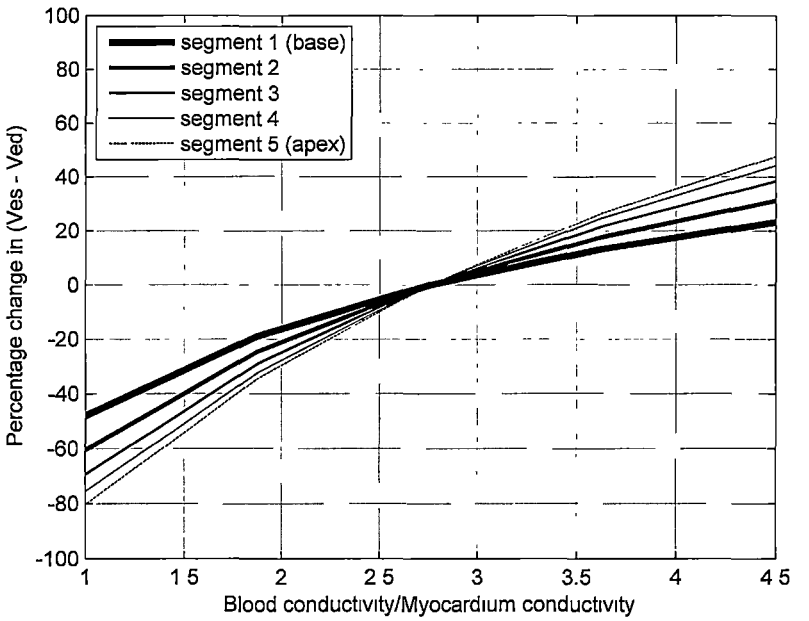

Figure 4.3.33: Percentage change in segment (Ves – Ved) for right ventricle catheter in tagged MRI model.

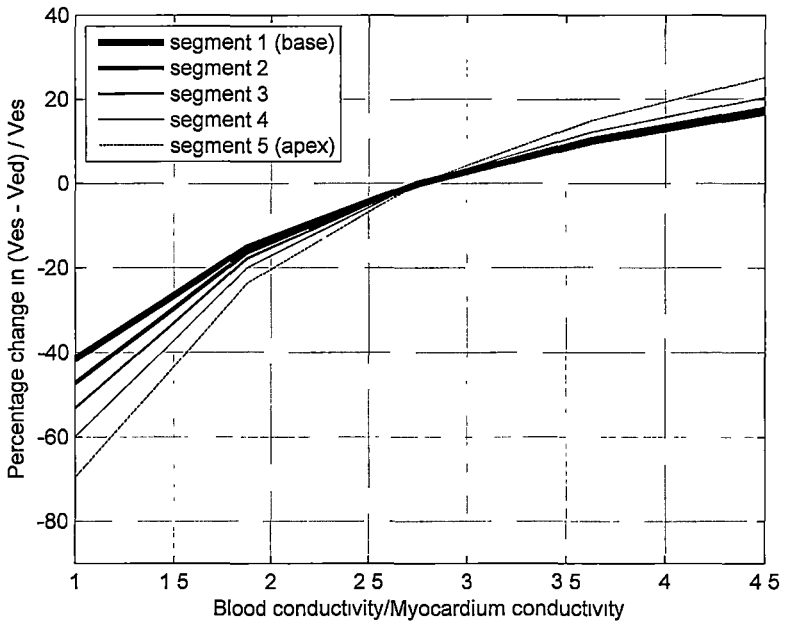

Figure 4.3.34: Percentage change in segment (Ves – Ved) / Ves for right ventricle catheter in tagged MRI model.

4.4 Discussion

The MRI model and tagged MRI model showed good agreement. The MRI end-diastole segment voltages, in Figure 4.3.1 and 4.3.2, were within 7% of tagged MRI. The MRI end-systole segment voltages were within 8% of tagged MRI, except at the apex. The MRI end-diastole to end-systole segment voltage differences were within, 23% in the left ventricle and 36% in the right ventricle, of tagged MRI, except at the apex.

In both the left and right ventricles an offset catheter generally causes an increase in end-systole segment voltage (Ves), and increase in (Ves – Ved). In general, this means worst case error results from catheter movement between centre and closer to the myocardium. The small negative values are due to the fact that what these investigations defined as centralised catheter were not quite the same centralised catheter position that is defined by minimum segment voltages. This new catheter centre definition is closer to the pulmonary artery and septum for the right ventricle catheter. For the left ventricle catheter it is closer to the septum, closer to the pulmonary artery at the apex and closer to the liver at the base. (Ves – Ved) is almost directly used to determine stroke volume using the standard conductance catheter formula. Using the standard conductance catheter formula, stroke volume is proportional to segment (1/Ved – 1/Ves). Assuming Ves – Ved << Ves or Ved, and a small error, a one percentage error in (Ves – Ved) for all segments (middle segments are more heavily weighted) will have approximately a one percent opposite effect on predicted stroke volume. So an increase in (Ves – Ved) from movement off centre will underestimate volume. The increase in (Ves – Ved) is typically greater than the increase in Ves, as indicated by percentage change in segment (Ves – Ved)/Ves plots. This means that the increase is not proportional to Ves and Ved, and that Ves increases proportionally more than Ved. It may be possible for the catheter to move during a cardiac cycle. If it moves off centre during systole only, the change in Ves will cause a change in (Ves – Ved) that may be greater than the change in (Ves – Ved) for a catheter off centre during the whole of the cardiac cycle. In the left ventricle the change in Ves is on the order of about 10% of (Ves – Ved)/Ves. In contrast the change in (Ves – Ved) is also on the order of 10% for the catheter movement shown. In the right ventricle the change in Ves is on the order of 25% to

50% of (Ves – Ved)/Ves. In contrast the change in (Ves – Ved) is on the order of 5% to 10% but a massive 25% with the catheter towards the liver. A right ventricle catheter moving off-centre during just systole may give a large error, but a catheter that is off centre but stationary throughout the cardiac cycle may give less error (except near the liver), due to some cancellation.

The order of magnitude of the results suggest that error due to catheter movement is significant in both the left and right ventricles. This is especially true since the catheter movements investigated were not the maximum possible. A curved catheter may also give even more error, but is more likely to decrease the segment voltages since the catheter may be at an angle relative to the contours between source electrodes.

The absolute segment (Ves – Ved)/Ves value for a conductivity ratio of 2.75 gives similar results to left and right ventricle experimental studies in the literature. The slopes of the segment curves decrease in magnitude and converge with increasing ratio. The values of the (Ves – Ved)/Ves curves are all quite low at ratios near 1 signifying increased conductivity of the opposite ventricle and myocardium. Maximum values are indicated for the middle segments due to local field effects creating higher voltage near the electrodes. This is further supported by a higher change in Ves for the middle segments compared to the apex and particularly in the right ventricle the base segments. The change in percentage (Ves – Ved) is strong and shows a clear pattern. For both ventricles the apex segment changes the most and the base segment the least, with gradual transition. In this regard the base segments, while they are less sensitive (lower Ves–Ved/Ves ratio) to the motion of the heart, they give less error at predicting motion with a change in ratio. The (Ves – Ved) is affected much more by changes in ratio than Ves, resulting in a similar pattern for percentage change in (Ves – Ved)/Ves. This means that the increase is not proportional to Ves and Ved, and that Ves increases proportionally more than Ved.

Higher ratio causes an over estimation in volume and lower ratio causes an underestimation of volume. Changes in ratio, for instance, down to 2 or up to 4, cause changes in (Ves – Ved) on the order of 25% for both ventricles. This sort of order of error makes the effect of ratio changes highly significant in both ventricles.

The modelling in this chapter has a number of limitations. These can be identified based on information compiled in the literature review chapter. This model assumed no current passed beyond the myocardium into surrounding tissues. This was based on the assumption that the heart is either covered with insulating adipose tissue (fat) or surrounded by insulating lung tissue. The surface of the heart in contact with the diaphragm/liver has little fat and some current may leak into the relatively low conductivity liver despite a large amount of fat covering the heart.

A more minor assumption was that the effects of anisotropic tissue conductivity could be ignored. Since the muscle fibre direction is in all directions in the plane of the myocardium, an equivalent isotropic value that has the same effect was assumed. Also another assumption is that trabeculations can be modelled as some smooth boundary between blood and myocardium.

Another limitation of this work is that it only tests one particular catheter geometry. A longer catheter may give less (most likely) error. To simulate a longer catheter however it may be necessary to extend the model into the atria, aorta and pulmonary artery, so source electrodes can be positioned outside the ventricle. Also the catheter was positioned as a straight catheter between base and apex. This minimised the effect of current flow into the base regions of the heart as the base was behind one of the source electrodes in the source electrode to source electrode direction. Accurate modelling of a catheter, for instance, between tricuspid valve and pulmonary artery would require inclusion of the atria and pulmonary artery, since the fibrous ring forming the base of the heart only acts as an insulator to active current propagation (depolarisation wave), not passive current flow. In such a situation anywhere up to half of the current may flow through the base region. The current flow only depends on source electrode positions, it has nothing to do with measurement electrode positions. Even if the measurement electrodes are curved towards the apex in such a situation, one must not neglect current flow through the base (to get an accurate result).

This study only investigated the effect on catheter measurements under the same conditions so calculation of ventricle volume was not required. Whatever the catheter position used, to obtain accurate ventricle volume from the model one would have to

model the full ventricles up to the level of the pulmonary, tricuspid, aortic and mitral valves. One cannot simply slice off the model near the valves since the valve plane moves during the cardiac cycle. Doing so, especially in the right ventricle would lead to inaccurate stroke volume changes as well as average volume. Conditions such as tricuspid regurgitation could make it impossible to determine blood flow from stroke volume if this was desired. This chapter also only considered normal human heart geometry. Hypertrophied and different sized hearts from humans may give different results. Animal hearts may also give different results.

4.5 Conclusion

The main conclusion from the work in this chapter is that catheter movement and changes in blood conductivity/myocardium conductivity may give significant error in the standard conductance catheter technique. In the next chapter the problem of correcting for these variables and others will be addressed in a simplified model of the heart.

Chapter 5. Investigation 2

5.1 Introduction

The purpose of this chapter is to investigate how well noiseless catheter measurements can be used to determine ventricular volume, tissue impedance and catheter position in a simple two-dimensional model. The previous chapter showed that catheter movement and tissue impedance changes give non-negligible error using existing methods for calculating volume from impedance measurements. Correction of these error sources is attempted by using additional information from different current source configurations and frequency changes in tissue properties. Different source configurations and source frequencies represent the only two source variables that can be changed. The ability to correct for the error sources using these variables is examined in a simplified model of the heart. The model will simulate simultaneous, four electrode technique catheter measurements taken at two different frequencies and multiple current source electrode separations. Finite element modelling offers the possibility of incorporating a priori information about geometry and electrical properties to map electrode measurements to stroke volume or blood flow. The effect of high frequency will be simulated by an exact 1.35 increase in tissue conductivity and a zero change in blood conductivity. Due to the simple, low variable number model used in this section only a subset of possible source current and voltage measurement configurations will be employed. First the derivatives of these voltage measurements will be calculated with respect to model variables to examine the magnitude of effect on catheter measurements. These derivative vectors will be compared to establish the separability of the effects of the three parameters. The technique employed to do this gives great insight into the mapping. Finally two different techniques will be employed to obtain an inverse mapping to the numerical model. These techniques will attempt to map catheter measurements to numerical model parameters. The two inverse techniques comprise neural networks and a new technique. It will be shown that a custom inverse mapping method outperforms the best conventional technique.

5.2 Methods

The parameterised two-dimensional numerical model used for studies in this chapter is detailed in the section entitled Numerical Model. Methods to calculate and compare the derivatives of catheter measurements with respect to the parameters of the numerical model are detailed in the section entitled Local Derivatives of the Numerical Model. Inverse mapping using neural networks of catheter measurements to model parameters is detailed in the section entitled Inverse Mapping Using Neural Networks. Finally inverse mapping using a new technique is detailed in the section Inverse Mapping Using New Distance Function Technique.

Numerical Model

The work in this chapter is based on the two-dimensional numerical model geometry shown in Figure 5.2.1. The model is parameterised by the variables *r*, *p*, and *c*, where: *r* represents half the width of the blood pool, *p* represents the distance the catheter is offset towards the tissue wall from the centre of the blood pool, and *c* represents the blood conductivity/myocardium conductivity ratio. The numerical model produces the voltage = voltage (V) x blood conductivity (S/m) / current (A) x width of model (m). This is the definition of all absolute voltages given in the results. The model has 10 electrodes. Distance between electrodes is 8mm and electrode length is 1mm.

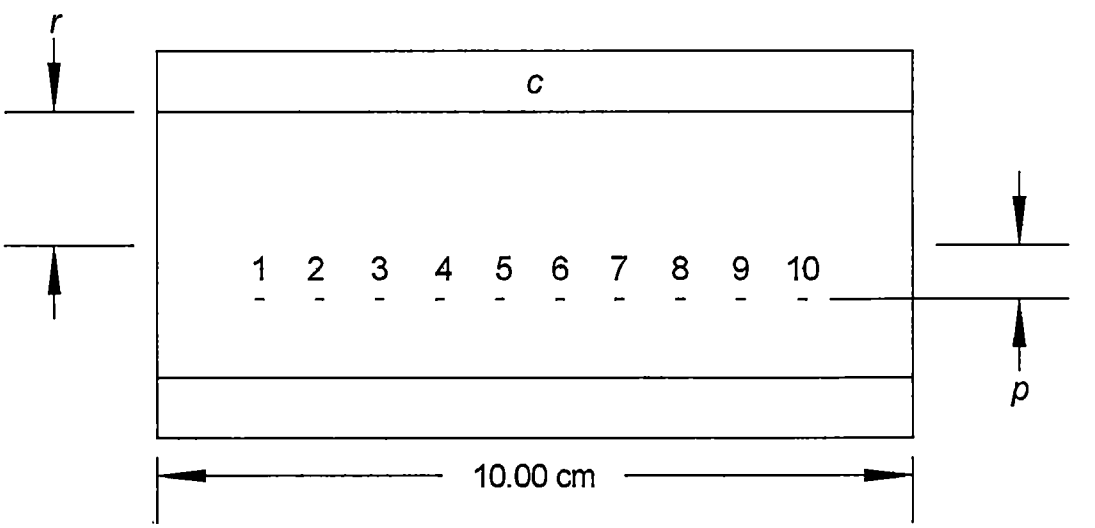

Figure 5.2.1: Numerical Model Geometry (drawn to scale). Model parameters: r = 1.75cm, p/r = 0.4.

All numerical modelling in this chapter is implemented using ANSYS finite element software version 10.0. The geometry is meshed in ANSYS using 2D eight node electric area elements (ANSYS element type: PLANE230). Element nodes along the electrodes are coupled in the VOLT degree of freedom to model each electrode. The solution for electric potential, based on the governing equation

$$\nabla \cdot (k \nabla u) = 0, \tag{5.2.1}$$

where: k = conductivity tensor, u = potential,

is solved (after application of boundary conditions) by formulating a matrix for the node voltages and solving using the ANSYS sparse matrix solver.

To obtain one set of catheter voltage measurements for a particular combination of r, p, and c, the numerical model is run four times, corresponding to four alternative "current" electrode pairs. The pairs used were electrodes 4-7, 3-8, 2-9 and 1-10. A voltage was set on one electrode, and a current on the other. Resulting voltages were measured between points of adjacent electrodes spanned by the "current" electrodes. Due to symmetry some of these voltages were the same and redundant voltages were not measured. These combinations of boundary conditions and measured voltages are shown in Table 5.2.1, as detailed below.

The first time the model is run with a source current of 1 AMPS at electrode 7 and voltage of zero at electrode 4. The voltage at electrode 6 minus the voltage at electrode 5 is recorded as the first catheter measurement. The second time the model is run with a source current of 1 AMPS at electrode 8 and voltage of zero at electrode 3. The voltage at electrode 6 minus the voltage at electrode 5 is recorded as the second catheter measurement. The voltage at electrode 7 minus the voltage at electrode 6 is recorded as the third catheter measurement. The third time the model is run with a source current of 1 AMPS at electrode 9 and voltage of zero at electrode 2. The voltage at electrode 6 minus the voltage at electrode 5 is recorded as the fourth catheter measurement. The voltage at electrode 7 minus the voltage at electrode 6 is recorded as the fifth catheter measurement. The voltage at electrode 8 minus the voltage at electrode 7 is recorded as the sixth catheter measurement. The fourth time the model is run with a source current of 1 AMPS at electrode 10 and

voltage of zero at electrode 1. The voltage at electrode 6 minus the voltage at electrode 5 is recorded as the seventh catheter measurement. The voltage at electrode 7 minus the voltage at electrode 6 is recorded as the eighth catheter measurement. The voltage at electrode 8 minus the voltage at electrode 7 is recorded as the ninth catheter measurement. The voltage at electrode 9 minus the voltage at electrode 2 is recorded as the tenth catheter measurement.

Table 5.2.1: Measured voltages from numerical model

Measurement	Current electrodes	Measured voltage (electrodes)
V_1	4 (0V), 7 (1A)	6 minus 5
V_2	3 (0V), 8 (1A)	6 minus 5
V_3	3 (0V), 8 (1A)	7 minus 6
V_4	2 (0V), 9 (1A)	6 minus 5
V_5	2 (0V), 9 (1A)	7 minus 6
V_6	2 (0V), 9 (1A)	8 minus 7
V_7	1 (0V), 10 (1A)	6 minus 5
V_8	1 (0V), 10 (1A)	7 minus 6
V_9	1 (0V), 10 (1A)	8 minus 7
V_{10}	1 (0V), 10 (1A)	9 minus 8

A total of twenty catheter measurements were obtained by running the model at both low frequency and high frequency. The high frequency catheter measurements eleven to twenty were obtained exactly the same way as catheter measurements one to ten except the tissue conductivity was multiplied by 1.35.

The convergence of the numerical model was assessed by changing the primary mesh density of the model. At different mesh densities the catheter measurements, number of nodes (degrees of freedom) and element count were recorded. A fixed set of model parameters (r = 1.75cm, p/r = 0.4, c = 2.75), representing average values used in this chapter, were used for assessing convergence. Using these same model parameters a total of eight different primary (the mesh was further refined around the electrodes) mesh densities were simulated. These primary mesh densities were:

0.0400, 0.0433, 0.0531, 0.0694, 0.0922, 0.1216, 0.1576, 0.2000 (cm). Results are shown in Section 5.3.

Local Derivatives of the Numerical Model

Local derivatives for a total of 20 catheter measurements were calculated using finite differencing of numerical model results. The local derivatives were calculated at only one set of the three parameters. The values of the three parameters are the same as that used for convergence assessment and represent approximately average values used in this chapter.

Partial derivatives with respect to r were calculated by generating 20 catheter measurements at the position r = 1.76 and r = 1.74 and given by:

$$\frac{\partial V_i(r=1.75, p/r=0.4, c=2.75)}{\partial r} = \frac{V_i(r=1.76, p/r=0.4, c=2.75) - V_i(r=1.74, p/r=0.4, c=2.75)}{0.02}$$

where: V_i = catheter measurement *i*.

Partial derivatives with respect to p/r were calculated by generating 20 catheter measurements at the position p/r = 0.41 and p/r = 0.39 and given by:

$$\frac{\partial V_i(r=1.75, p/r=0.4, c=2.75)}{\partial p/r} = \frac{V_i(r=1.75, p/r=0.41, c=2.75) - V_i(r=1.75, p/r=0.39, c=2.75)}{0.02}$$

where: V_i = catheter measurement *i*.

Partial derivatives with respect to c were calculated by generating 20 catheter measurements at the position c = 2.76 and c = 2.74 and given by:

$$\frac{\partial V_i(r=1.75, p/r=0.4, c=2.75)}{\partial c} = \frac{V_i(r=1.75, p/r=0.4, c=2.76) - V_i(r=1.75, p/r=0.4, c=2.74)}{0.02}$$

where: V_i = catheter measurement *i*.

The partial derivatives were organised into three vectors:

$$\frac{dV}{dr} = \left[\frac{\partial V_1}{\partial r} \quad \frac{\partial V_2}{\partial r} \quad \frac{\partial V_i}{\partial r} \quad \cdots \quad \frac{\partial V_{20}}{\partial r}\right],$$

$$\frac{dV}{dp/r} = \left[\frac{\partial V_1}{\partial p/r} \quad \frac{\partial V_2}{\partial p/r} \quad \frac{\partial V_i}{\partial p/r} \quad \cdots \quad \frac{\partial V_{20}}{\partial p/r}\right],$$

$$\frac{dV}{dc} = \left[\frac{\partial V_1}{\partial c} \quad \frac{\partial V_2}{\partial c} \quad \frac{\partial V_i}{\partial c} \quad \cdots \quad \frac{\partial V_{20}}{\partial c}\right].$$

Angles in Euclidean space were generated between full and subsets of these three (one for each of r, p/r and c) partial derivative vectors to give some insight into how well conditioned the inverse mapping is locally and the most important catheter measurements.

Inverse Mapping Using Neural networks

Neural networks were created using the MATLAB functions newff() and newgrnn() with the training data. Newff() was used to create simple feedforward networks and newgrnn() was used to create radial basis networks. Various feedforward networks were created with different numbers of hidden layers (1 or 2) and hidden layer neurons (3-20). The hidden layers all used the transfer function 'tansig' and had an output layer transfer function 'purelin'. Various radial basis networks were created with different values of spread constant (the Euclidean distance of the test data points from the training data points at which the radial basis functions outputs are half their maximum). All networks were configured to give a single output variable r with the 20 catheter measurements as inputs. After training the networks were applied with the test data to give a prediction for r. The actual value of r parameter from the test data was then subtracted from the r value given by the network to give the error.

Generation of training data was done in a 8×8×8 evenly spaced grid of model parameters. A set of 10 low frequency catheter measurements were recorded (by running the numerical model with a primary mesh density of 0.2cm) for each of the 512 grid points representing all combinations of the three model parameters:

r (cm) = [1, 1.214, 1.429, 1.643, 1.857, 2.071, 2.286, 2.5],

p/r = [0, 0.114, 0.229, 0.343, 0.457, 0.571, 0.686, 0.8],

c = [2.2, 2.357, 2.514, 2.671, 2.829, 2.986, 3.143, 3.3].

A set of corresponding 10 high frequency (with c divided by 1.35) catheter measurements were recorded (by running the numerical model with a primary mesh density of 0.2cm) for each of the 512 grid points using all combinations of the three model parameters:

r (cm) = [1, 1.214, 1.429, 1.643, 1.857, 2.071, 2.286, 2.5],

p/r = [0, 0.114, 0.229, 0.343, 0.457, 0.571, 0.686, 0.8],

c = [1.630, 1.746, 1.862, 1.979, 2.095, 2.212, 2.328, 2.444].

The numerical modelling process was fully automated using ANSYS scripting.

Generation of test data was done by selecting 50 random parameter points. The probability of selecting a parameter point was uniform over the range:
$1.2cm < r < 2.3cm$, $0.1 < p/r < 0.7$, $2.4 < c < 3.2$, and zero elsewhere. At each of these points a set of 20 catheter measurements were calculated. The first 10 measurements were simply the 10 catheter measurements for the three different parameters at the point. The second set of catheter measurements were the 10 catheter measurements calculated at the same r and p/r parameters as the point, but with a value of c equal to the c at the point divided by 1.35. The first 10 catheter measurements represented the response to lower frequency current and the second 10 represented the response to higher frequency current at which the tissue conductivity was assumed to increase by 1.35. Along with the 20 catheter measurements the three parameters associated with them were stored.

Inverse Mapping Using New Distance Function Technique

Uniformly gridded base data was interpolated for any arbitrary three parameters r, p/r and c within the range of the base data using MATLAB. 20 catheter measurements are generated using this interpolation process for any r, p/r and c. Optimisation was done to find the value of r, p/r and c, that gives the minimum mean squared error in the difference of the 20 interpolation generated catheter measurements and a particular set of 20 test data catheter measurements. The value of three parameters from the test data is then subtracted from the three parameter values given by the optimisation routine at its completion to give the error. The optimisation algorithm used was MATLAB's lsqnonlin('LargeScale','on') (non linear least squares optimisation) and the interpolation algorithm used was MATLAB's interpn('*linear') (linear interpolation).

Base/training data was the same data used for the neural network inverse mapping, except the minimum value of c was reduced by 1.35. The use of interpolation allowed both low frequency and high frequency to be generated from just 10 catheter measurements (half the numerical model runs as done for neural networks). A set of 10 catheter measurements were recorded (by running the numerical model with a primary mesh density of 0.2cm) for each of the 512 grid points representing all combinations of the three model parameters:
r (cm) = [1, 1.214, 1.429, 1.643, 1.857, 2.071, 2.286, 2.5],

p/r = [0, 0.114, 0.229, 0.343, 0.457, 0.571, 0.686, 0.8],
c = [1.6, 1.843, 2.086, 2.329, 2.571, 2.814, 3.057, 3.3].

The same test set of data was used that was generated for use with the neural networks as described in the previous section entitled Inverse Mapping Using Neural Networks.

5.3 Results

Numerical Model

A plot of the element mesh for a primary mesh density of 0.2cm is shown in Figure 5.3.1. Note the mesh refinement around the electrodes that was used.

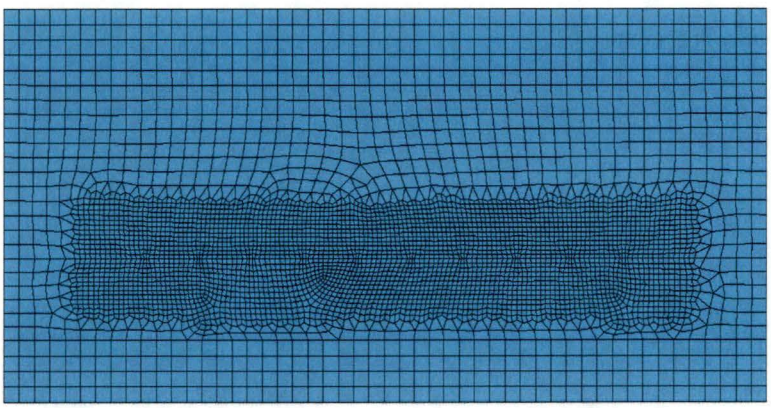

Figure 5.3.1: Finite element mesh for primary mesh density = 0.2cm. Model parameters: r = 1.75cm, p/r = 0.4, c = 1.75.

Contour plots of the voltage potential solution for a primary mesh density of 0.2cm are shown in Figure 5.3.2 to Figure 5.3.5. The different figures show the effect of changing the source electrodes used.

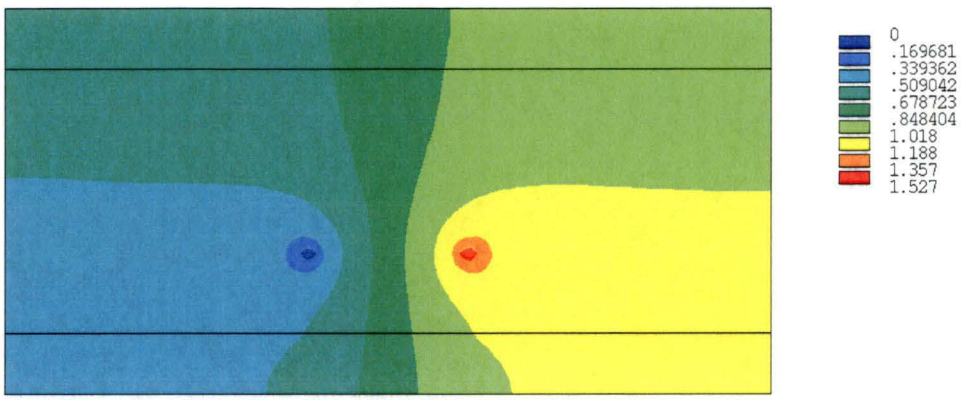

Figure 5.3.2: Finite element solution (voltage) distribution. Source electrodes = 4 and 7. Primary mesh density of 0.2cm. Numbers in legend are: voltage (V) x blood conductivity (S/m) / current (A) x width of model (m). Model parameters: r = 1.75cm, p/r = 0.4, c = 1.75.

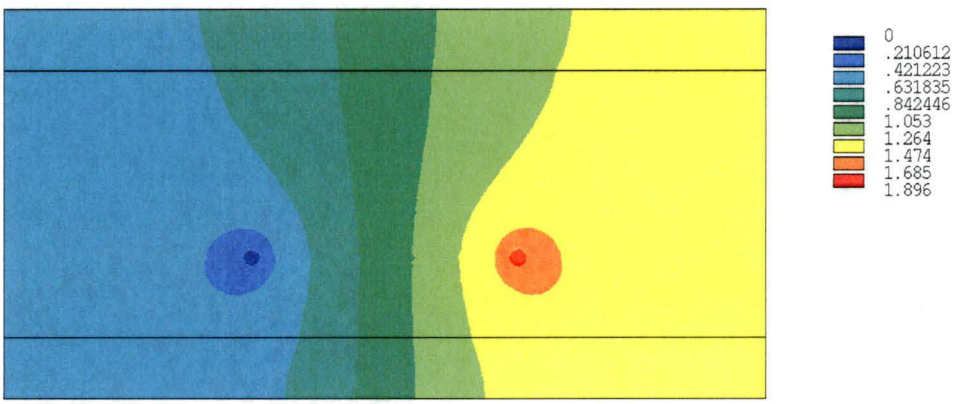

Figure 5.3.3: Finite element solution (voltage) distribution. Source electrodes = 3 and 8. Primary mesh density of 0.2cm. Numbers in legend are: voltage (V) x blood conductivity (S/m) / current (A) x width of model (m). Model parameters: r = 1.75cm, p/r = 0.4, c = 1.75.

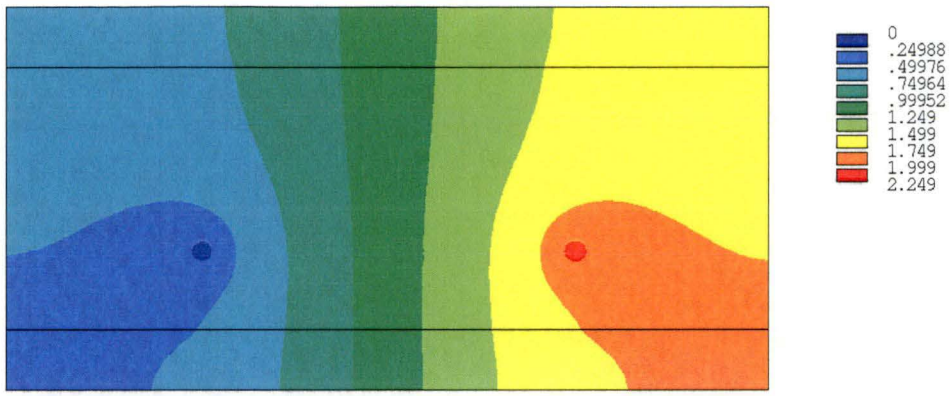

Figure 5.3.4: Finite element solution (voltage) distribution. Source electrodes = 2 and 9. Primary mesh density of 0.2cm. Numbers in legend are: voltage (V) x blood conductivity (S/m) / current (A) x width of model (m). Model parameters: r = 1.75cm, p/r = 0.4, c = 1.75.

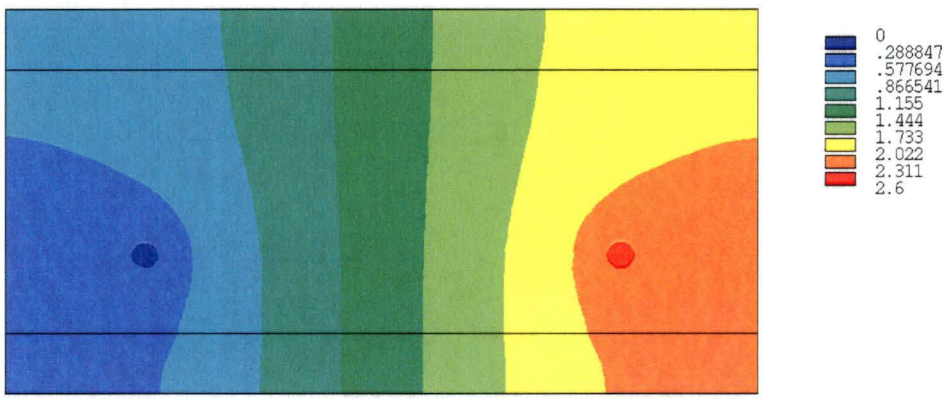

Figure 5.3.5: Finite element solution (voltage) distribution. Source electrodes = 1 and 10. Primary mesh density of 0.2cm. Numbers in legend are: voltage (V) x blood conductivity (S/m) / current (A) x width of model (m). Model parameters: r = 1.75cm, p/r = 0.4, c = 1.75.

For various mesh densities the percentage difference of the 10 catheter measurements relative to the most finely meshed model is shown in Table 5.3.1. The convergence of the rms error of all ten measurements is shown in Figure 5.3.6.

Table 5.3.1: Convergence of catheter measurements. Percentage difference of the 10 catheter measurements relative to most finely meshed model. Model parameters: r = 1.75cm, p/r = 0.4, c = 1.75.

Mesh size (cm)	0.0400	0.0433	0.0531	0.0694	0.0922	0.1216	0.1576	0.2000
Nodes	125740	116889	81830	59468	40458	25311	19033	14103
Elements	41661	38728	27085	19675	13375	8352	6278	4650
Variable	Percentage change from 0.0400 mesh size							
V_1	0.0000	-0.0034	-0.0090	-0.0134	-0.0198	-0.0407	-0.0571	-0.0772
V_2	0.0000	-0.0027	-0.0067	-0.0098	-0.0147	-0.0319	-0.0436	-0.0512
V_3	0.0000	-0.0037	-0.0062	-0.0119	-0.0174	-0.0316	-0.0443	-0.0618
V_4	0.0000	-0.0027	-0.0068	-0.0100	-0.0149	-0.0323	-0.0430	-0.0509
V_5	0.0000	-0.0034	-0.0051	-0.0102	-0.0146	-0.0264	-0.0364	-0.0505
V_6	0.0000	-0.0017	-0.0071	-0.0116	-0.0163	-0.0270	-0.0441	-0.0572
V_7	0.0000	-0.0029	-0.0070	-0.0103	-0.0153	-0.0328	-0.0430	-0.0518
V_8	0.0000	-0.0035	-0.0054	-0.0105	-0.0149	-0.0264	-0.0363	-0.0514
V_9	0.0000	-0.0014	-0.0063	-0.0100	-0.0137	-0.0214	-0.0357	-0.0481
V_{10}	0.0000	-0.0026	-0.0082	-0.0130	-0.0185	-0.0269	-0.0432	-0.0696

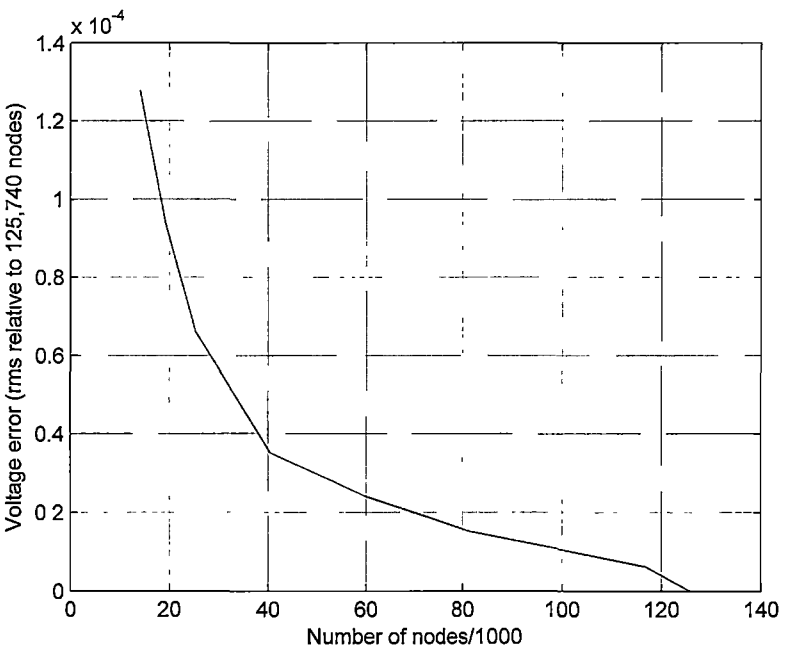

Figure 5.3.6: Convergence of catheter measurements. Numbers plotted are: Absolute rms error of all 10 measurements (V) x blood conductivity (S/m) / current (A) x width of model (m). Model parameters: r = 1.75cm, p/r = 0.4, c = 1.75.

Local Derivatives of the Numerical Model

Local partial derivatives of the catheter measurements with respect to model parameters r, p/r, c are given in Table 5.3.2, 5.3.3 and 5.3.4 respectively. All the partial derivatives were calculated at the local point r = 1.75cm, p/r = 0.4, c =2.75 as described in Section 5.2. Each table gives the absolute derivatives calculated with a mesh density of 0.05cm, percentage derivatives (absolute derivative/absolute measurement voltage at the local point x100) and percentage difference between derivative calculated at 0.08cm mesh and 0.05cm mesh (to give an idea of accuracy). Table 5.3.5 shows the angles between absolute partial derivative vectors for different combinations of measurement variables.

Table 5.3.2: Partial derivatives with respect to r. units are: voltage (V) x blood conductivity (S/m) / current (A) x width of model (m) / change in r (cm), 100 / change in r (cm), 100 / change in r (cm).

i	(absolute) $\frac{\partial V_i}{\partial r}$	(%) $\frac{\partial V_i}{\partial r}\times\frac{100}{V_i}$	(Δ%) $\left(\left(\frac{\partial V_i}{\partial r}\right)_{0.08}-\left(\frac{\partial V_i}{\partial r}\right)_{0.05}\right)\times\frac{100}{V_i}$
1	-0.0483	-17.6	-0.64
2	-0.0631	-30.2	-0.33
3	-0.0591	-25.5	-0.38
4	-0.0700	-37.1	-0.30
5	-0.0684	-35.1	-0.25
6	-0.0622	-27.5	-0.18
7	-0.0738	-40.9	-0.28
8	-0.0730	-39.9	-0.23
9	-0.0701	-36.5	-0.12
10	-0.0627	-27.9	-0.38
11	-0.0416	-15.4	-0.71
12	-0.0554	-27.4	-0.34
13	-0.0519	-23.0	-0.41
14	-0.0623	-34.4	-0.32
15	-0.0607	-32.4	-0.26
16	-0.0550	-25.1	-0.19
17	-0.0662	-38.3	-0.29
18	-0.0653	-37.3	-0.23
19	-0.0624	-33.8	-0.12
20	-0.0555	-25.4	-0.41

Table 5.3.3: Partial derivatives with respect to *p/r*. units are: voltage (V) x blood conductivity (S/m) / current (A) x width of model (m) / change in *p/r* (cm/cm), 100 / change in *p/r* (cm/cm), 100 / change in *p/r* (cm/cm).

i	(absolute) $\frac{\partial V_i}{\partial p/r}$	(%) $\frac{\partial V_i}{\partial p/r} \times \frac{100}{V_i}$	(Δ%) $\left(\left(\frac{\partial V_i}{\partial p/r}\right)_{0.08} - \left(\frac{\partial V_i}{\partial p/r}\right)_{0.05}\right) \times \frac{100}{V_i}$
1	0.0612	22.3	1.05
2	0.0590	28.2	0.81
3	0.0519	22.4	-1.10
4	0.0445	23.6	0.93
5	0.0441	22.7	-1.22
6	0.0410	18.1	-0.60
7	0.0311	17.2	1.26
8	0.0324	17.7	-1.59
9	0.0377	19.6	-0.54
10	0.0388	17.3	0.41
11	0.0516	19.1	1.22
12	0.0516	25.6	0.90
13	0.0452	20.1	-1.22
14	0.0408	22.5	0.98
15	0.0398	21.3	-1.30
16	0.0362	16.5	-0.66
17	0.0298	17.3	1.26
18	0.0306	17.5	-1.61
19	0.0343	18.6	-0.56
20	0.0343	15.7	0.45

Table 5.3.4: Partial derivatives with respect to c. units are: voltage (V) x blood conductivity (S/m) / current (A) x width of model (m) / change in c (S/m / S/m), 100 / change in c (S/m / S/m), 100 / change in c (S/m / S/m).

i	(absolute) $\frac{\partial V_i}{\partial c}$	(%) $\frac{\partial V_i}{\partial c} \times \frac{100}{V_i}$	(Δ%) $\left(\left(\frac{\partial V_i}{\partial c}\right)_{0.08} - \left(\frac{\partial V_i}{\partial c}\right)_{0.05}\right) \times \frac{100}{V_i}$
1	0.0060	2.2	0.02
2	0.0078	3.7	0.02
3	0.0072	3.1	0.02
4	0.0084	4.4	0.02
5	0.0082	4.2	0.02
6	0.0073	3.2	0.02
7	0.0085	4.7	0.01
8	0.0085	4.6	0.01
9	0.0082	4.3	0.02
10	0.0073	3.3	0.01
11	0.0072	2.7	0.02
12	0.0094	4.7	0.02
13	0.0087	3.9	0.02
14	0.0102	5.6	0.01
15	0.0099	5.3	0.02
16	0.0089	4.0	0.02
17	0.0104	6.0	0.01
18	0.0103	5.9	0.01
19	0.0100	5.4	0.01
20	0.0089	4.1	0.01

Table 5.3.5: Angles (in degrees) between absolute partial derivative vectors. i = 1-10 is low frequency data, i = 11-20 is equivalent high frequency data, i = 7-10 is segments between furthest separated source electrodes, i = 1,2,4,7 is middle segment (for each of the four different source configurations). Refer to Table 5.2.1 in Section 5.2 for precise definition of each i.

i used	dV/dr to $dV/dp/r$	dV/dr to dV/dc	$dV/dp/r$ to dp/dc
1-20	17.5	9.1	18.2
1-10	18.1	1.4	16.8
7-10,17-20	8.1	8.9	11.1
1,2,4,7,11,12,14,17	21.1	9.2	21.2
1,2,4,7	21.8	1.7	20.2

Inverse Mapping Using Neural networks

Table 5.3.6 shows the standard deviation (s.d.), mean, minimum and maximum of error in r parameter from inverse mapping using radial basis neural networks. The error is defined as the predicted r from the network minus the actual r of the test or training data. It should be divided by 1.75 (and multiplied by 100) to give percentage error. Two different networks are shown with different values of spread. Results for each network with test data and training data and are shown. Results from radial basis networks with different spread and multilayer neural networks with various configurations of hidden nodes were similar or worse than that in Table 5.3.6 and are not shown.

Table 5.3.6: Error in r parameter (cm). Radial basis neural network. Training data used 512 points based on 4096 numerical model simulations.

Configuration	s.d. error	mean error	min. error	max. error
Spread = 0.04 Test data input	0.1095	0.0041	-0.3127	0.1810
Spread = 0.04 Training data input	0.1422	-0.0071	-0.4523	0.2823
Spread = 0.03 Test data input	0.1108	-0.0272	-0.3567	0.1438
Spread = 0.03 Training data input	0.1202	-0.0071	-0.4052	0.2535

Inverse Mapping Using New Distance Function Technique

Table 5.3.7 shows the standard deviation (s.d.), mean, minimum and maximum of error in *r, p/r* and *c* parameters from inverse mapping using the new distance function technique. The error is defined as the predicted parameter from the network minus the actual parameter of the test data. The error for *r*, *p/r* and *c* should be divided by 1.75, 0.4 and 2.75 respectively (and multiplied by 100) to give percentage error. Results are shown for test data identical to that used in Table 5.3.6. Results for base/training data set as input give essentially zero error with this technique and are not shown.

Table 5.3.7: Error in r, p/r and c parameters (cm, cm/cm, S/m / S/m). New distance function technique. Training data used 512 points based on 2048 numerical model simulations.

Parameter	s.d. error	mean error	min. error	max. error
r	0.0032	+0.0030	-0.0099	+0.0084
p/r	0.0040	-0.0080	-0.0175	-0.0004
c	0.0108	+0.0129	-0.0108	+0.0324

5.4 Discussion

The results from the two dimensional model seem to have reasonable order of magnitude when compared to the results from the three-dimension models developed in Chapter 4. Comparing the numerical data in Figures 5.3.2 to 5.3.5 to Figures 4.3.1 and 4.3.2, suggests a two dimensional model with width of about 3cm gives the same magnitude of results as a catheter in the left or right ventricles of the three dimensional model. It should be noted that the catheter used in this chapter is different from the catheter used in the last chapter. It has ten electrodes rather than eight and the electrode spacing is 8mm compared to 7mm. This does not affect comparison since results are contours in Figures 5.3.2 to 5.3.5 and not segment voltages.

Derivatives with respect to r showed a strong decrease in catheter voltages with increasing r. Derivatives with respect to p/r showed a strong increase in catheter voltages with increasing p/r. Derivatives with respect to c also showed a relatively strong increase in catheter voltages with increasing c. While the magnitudes of derivatives with respect to c were smaller than the derivatives for r and p/r, c can vary by a much greater range. Looking at the percentage change in derivatives with increase in mesh density, all the derivatives change by less than 10% (comparing the last two columns of the tables), with derivatives with respect to p/r the least accurate. Derivatives with respect to r and c however showed a strong biased change in one direction with a change in mesh density.

The angles between different subsets of the derivative vectors (Table 5.3.5) suggest frequency was very important for distinguishing c from r. Frequency (i = 11-20) played little part in separating p/r and c, and p/r and r. Different voltages from the same segment (i = 1,2,4,7) were a significant factor in separating p/r and c, and p/r and r. In comparison the voltages from one particular source configuration (i = 7-10,17-20) played a much less significant role. This supports the usefulness of different current source configurations for distinguishing p/r. Although not shown, angles between derivatives with respect to myocardium thickness showed thickness behaved almost exactly the same as c. It appears that from a distance away from the myocardium (as used in these calculations of derivatives) thickness cannot be

separated from c. The use of derivative angles gave a great insight into the inverse mapping. In addition, calculation of derivative angles is simple and does not require determining the inverse mapping.

From Table 5.3.7 with worst case parameter error in the order of 1% or less, it would appear the inverse mapping using all 20 catheter measurements to predict r, p/r and c exists and is relatively unique. When thickness was included in the predicted variables (not shown) the parameter error was very high suggesting a non unique mapping. This supports to some extent the angle data that suggests that c and thickness cannot be distinguished from each other. The method used to generate Table 5.3.7 was the new distance function technique. The neural network approach gave over 30 times the standard deviation of error and 30 times the worst case error as the new distance function technique. This suggests neural networks are incapable of solving this particular inverse problem. They are not well suited to ill-conditioned mappings, such as this one.

The only limiting factor stopping the distance function from solving highly ill-conditioned problems is numerical error introduced through approximation of the numerical model by interpolation. If optimisation was coupled directly to the numerical model (although impractical), it could theoretically produce an inverse mapping as accurate as the numerical error in the numerical model. It would then be possible to solve any highly ill-conditioned inverse problem that is unique. The problem then is not the ability to produce an inverse mapping. The largest problem is the effect of unmodelled error on the inverse mapping. If the catheter measurements cannot be found exactly in the numerical model (due to difference between model and experiment configuration or just electrical noise or offsets), the inverse method may not converge properly to the best parameters. In the next chapter the effect of such error on the inverse method is assessed. The distance function is also changed to make the inverse method converge to better parameters.

The major limitation of the work in this chapter is that the results are based on a 2D model, not a 3D model.

5.5 Conclusion

The work in this chapter suggests that it is possible to uniquely map catheter measurements alone to predict volume, catheter position and myocardium conductivity. The new distance function technique worked far better than neural networks in generating this mapping. The data presented shows that it is frequency that allows conductivity to be separated from volume. Also it shows that it is different current source configurations that allow catheter position to be determined from volume and conductivity uniquely. Thickness appears to be indistinguishable from conductivity (when the catheter is at distance from the myocardium anyway). The major limitation of the work in this chapter is that the results are based on a 2D model, not a 3D model.

The next chapter will assess the performance of the distance function inverse mapping technique with unmodelled error. The technique will also be further developed.

Chapter 6. Investigation 3

6.1 Introduction

In this chapter the distance function technique used in Investigation 2 is extended to take account of unmodelled error. In Investigation 2 we showed that the distance function inverse approach may be used to obtain an arbitrarily close inverse mapping for small levels of unmodelled error (arising from interpolation error). In this chapter the performance of the distance function technique will be assessed on data with a much higher level of error, similar to that expected in a real application. In addition, a more generalised technique will be developed based on the concept of finding the most probable model configuration for a given catheter measurement. This more generalised technique has the potential to improve inverse mapping with error corrupted measurement data and also has the potential to account for non-unique inverse mapping using probability information (in general, the distance function technique used in Investigation 2 will converge to an unknown non-unique model). In this chapter the more generalised technique will be applied to improve performance under the condition of unmodelled error magnitude that is not uniform for various variables or transformations of variables. Firstly in Section 6.2 it will be shown how maximising probability and minimising distance relate to each other.

Unmodelled error in catheter measurements can come from a variety of sources. These include, with the approximate expected range of error in brackets:

- electronic noise (random gaussian distribution 0.1%-10+%)
- electronic biased error (constant error 0.1%-1+%)
- catheter electrode spacing biased error (constant error 0.5%-10%)
- geometry differences between model and experiment (constant error 0.5%-10+%)
- other (random error up to 10% during free breathing respiration, posture)

Factors complicate determining the most realistic amount of error for use in this chapter. For instance a more realistic three dimensional numerical model may be less sensitive to unmodelled error than the two dimensional model used for work in this chapter.

6.2 Theory

In this section it will be shown how maximisation of probability is the same as minimisation of sum of squared error.

The aim is to select the set of model parameters (eg ventricle geometry, catheter position) that is most probable to produce a set of measurements (eg catheter voltages). This problem can be stated as:

$$\begin{aligned} &\text{Choose } x_1, x_2, \ldots, x_m \text{ to} \\ &\text{maximise } P = P(x_1, x_2, \ldots, x_m, y'_1, y'_2, \ldots, y'_n), \end{aligned} \tag{6.2.1}$$

where: P = probability density function, $x_i = i^{th}$ model variable, $y'_i = i^{th}$ measured variable (catheter or transformed catheter measurements).

Now assuming the effect of each of the measurement variables is an independent Gaussian distribution of the error between measured variables and associated measurement variables from the model, P can be written as:

$$P = P_x(x_1, x_2, \ldots, x_m) \prod_{i=1}^{n} \frac{1}{\sigma_i \sqrt{2\pi}} e^{-\frac{(y'_i - y_i)^2}{2\sigma_i^2}}, \tag{6.2.2}$$

where: $y_i = i^{th}$ measurement variable from the model, σ_i = standard deviation of error between the i^{th} measured variable and the i^{th} measurement variable from model.

Rearranging (6.2.2) gives:

$$P = e^{\ln\left(P_x(x_1, x_2, \ldots, x_m) \prod_{i=1}^{n} \frac{1}{\sigma_i \sqrt{2\pi}}\right) - \sum_{i=1}^{n} \frac{(y'_i - y_i)^2}{2\sigma_i^2}}. \tag{6.2.3}$$

Maximising a monotonic function of P is equivalent to maximising P. Since the natural logarithm is a monotonic function, (6.2.1) can be written as:

$$\begin{aligned} &\text{Choose } x_1, x_2, \ldots, x_m \text{ to} \\ &\text{maximise } \ln(P) = \ln\left(P_x(x_1, x_2, \ldots, x_m) \prod_{i=1}^{n} \frac{1}{\sigma_i \sqrt{2\pi}}\right) - \sum_{i=1}^{n} \frac{(y'_i - y_i)^2}{2\sigma_i^2}. \end{aligned} \tag{6.2.4}$$

Alternatively (6.2.4) can be written as,

Choose $x_1, x_2, \ldots, x_m$ to

$$\text{minimise } -\ln(P) = \sum_{i=1}^{n} \frac{(y'_i - y_i)^2}{2\sigma_i^2} - \ln\left(P_x(x_1, x_2, \ldots, x_m) \prod_{i=1}^{n} \frac{1}{\sigma_i \sqrt{2\pi}} \right). \tag{6.2.5}$$

Alternatively (6.2.5) can be written as,

Choose $x_1, x_2, \ldots, x_m$ to

$$\text{minimise } -\ln(P) = \sum_{i=1}^{n} \frac{(y'_i - y_i)^2}{2\sigma_i^2} - \ln(P_x(x_1, x_2, \ldots, x_m)) - \ln\left(\prod_{i=1}^{n} \frac{1}{\sigma_i \sqrt{2\pi}} \right). \tag{6.2.6}$$

Since,

$$\prod_{i=1}^{n} \frac{1}{\sigma_i \sqrt{2\pi}} = C_1, \tag{6.2.7}$$

where C_1 is some constant,

Equation (6.2.6) reduces to,

Choose $x_1, x_2, \ldots, x_m$ to

$$\text{minimise} \sum_{i=1}^{n} \frac{(y'_i - y_i)^2}{2\sigma_i^2} - \ln(P_x(x_1, x_2, \ldots, x_m)). \tag{6.2.8}$$

Alternatively (6.2.8) can be written,

Choose $x_1, x_2, \ldots, x_m$ to

$$\text{minimise} \sum_{i=1}^{n} \frac{(y'_i - y_i)^2}{2\sigma_i^2} + (A - \ln(P_x(x_1, x_2, \ldots, x_m))), \tag{6.2.9}$$

where: A = constant selected to make the bracketed term always greater than zero.

Alternatively (6.2.9) can be written,

$$\text{Choose } x_1, x_2, \ldots, x_m \text{ to}$$

$$\text{minimise} \sum_{i=1}^{n} \left(\frac{C_2}{\sigma_i} (y'_i - y_i) \right)^2 + \left(C_2 \sqrt{2(A - \ln(P_x(x_1, x_2, \ldots, x_m)))} \right)^2, \tag{6.2.10}$$

where: C_2 = any constant.

Equation (6.2.10) states that the most probable set of model parameters is one that minimises the weighted mean squared error including an extra error-like term that depends on the model variables.

Now if,

$$P(x_1, x_2, \ldots, x_m) = C_3, \tag{6.2.11}$$

where C_3 is some constant,

then (6.2.10) can be reduced to,

$$\text{Choose } x_1, x_2, \ldots, x_m \text{ to}$$

$$\text{minimise} \sum_{i=1}^{n} \left(\frac{C_2}{\sigma_i} (y'_i - y_i) \right)^2 . \tag{6.2.12}$$

Equation (6.2.12) states that the most probable set of model parameters is the one that minimises the weighted (by some number inversely proportional to the standard deviation) mean squared error of measurement.

If the error of measurement is identically distributed (6.2.12) reduces to,

$$\text{Choose } x_1, x_2, \ldots, x_m \text{ to}$$

$$\text{minimise } \sum_{i=1}^{n} (y'_i - y_i)^2 . \tag{6.2.13}$$

Equation (6.2.13) states that the most probable set of model parameters is the one that minimises the mean squared error of measurement.

Equation (6.2.13) was used in Investigation 2 and will be used again in the first part of the methods of this chapter. We have shown how this equation assumes uniform probability distributions of error for all variables. Equation (6.2.12) will be used in the second and third parts of the methods of this chapter. It allows for non-uniform probability distributions of error in variables. Equation (6.2.10) (which is in a form suitable for use with specialised least squares optimisation routines) and (6.2.8) will be discussed later in the chapter. These equations additionally allow incorporation of parameter variation probability.

6.3 Methods

Numerical modelling in this chapter was identical to the last chapter and will not be repeated here. The exact same base/training data generation and interpolation of catheter measurements was done in this chapter as in the last chapter for the distance function based inverse mapping. The exact same MATLAB optimisation routine used in the last chapter, lsqnonlin() was used for methods in this chapter. The difference in this chapter is that error is applied to test measurements and a different distance function is optimised. The new methods and applications only will be presented. The methods are divided into three sections: Performance with Uniformly Distributed Unmodelled Error, Average/Difference Transformation to Reduce Biased Unmodelled Error, and Same Segment Ratio Transformation to Reduce Biased Unmodelled Error. The first methods section will provide information about how sensitive the inverse mapping is to uniform distribution of error added to measurement data. This information will be in the form of model parameter error. The second and third sections will introduce methods to minimise the effects of biased measurement error. These two sections seek to reduce the effect of biased measurement error by using transformations of measurement data that cancel it out to some extent. The optimisation bounds on the parameters were: $1.2<r<2.3$, $0.1<p/r<0.7$, and $2.4<c<3.2$. The optimisation initial starting values were: $r = 1.4$, $p/r = 0.6$, and $c = 3$.

Performance with Uniformly Distributed Unmodelled Error

Generation of test data was accomplished by running the numerical model with the parameters $r = 1.75$cm, $p/r = 0.4$ and $c = 2.75$ to generate 20 catheter measurements. 50 sets of test data were generated by adding to this set of 20 catheter measurements random normally distributed error with mean of zero and desired standard deviation, s.

The optimisation procedure was then used to minimise the mean squared difference between a set of all 20 (both frequencies) or first 10 (low frequency only) test measurements and the data interpolated from the base data. The optimisation procedure was used to find all or a subset (with one or more parameters fixed to the actual value: $p/r = 0.4$, $c = 2.75$) of the three model parameters. Parameter error for r,

p/r and c was the final parameter from optimisation minus 1.75cm, 0.4 and 2.75 respectively.

This procedure was repeated a number of times as detailed in Section 6.4 for various values of s, various parameters fixed in the optimisation, and different inclusion of measurement data (both frequencies/low frequency only).

Average/Difference Transformation to Reduce Biased Unmodelled Error

Generation of test data was accomplished by running the numerical model with the parameters r = 1.45cm, p/r = 0.4 and c = 2.75 to generate 20 catheter measurements. This was repeated with the parameters r = 2.05cm, p/r = 0.4 and c = 2.75 to generate another set of 20 measurements. The first set of measurements with r = 1.45cm represent end-systole measurements while the second set of measurements with r = 2.05cm represent end-diastole measurements. From these 40 measurements, 20 average and 20 difference values were calculated. 50 sets of test data were generated by adding to this set of 40 transformed catheter measurements, random normally distributed error with mean of zero and desired standard deviation, s. The 20 average values had error added with a higher standard deviation to represent biased error. The 20 difference values had a much smaller standard deviation of error added to represent some cancellation of biased error.

The optimisation procedure was then used to minimise the weighted mean squared difference between a set of all 40 test measurements and the equivalent transformed data interpolated from the base data. The weights used had the appropriate ratio based on standard deviation of error applied as specified in (6.2.12). The optimisation procedure was used to find the parameters r1 (end-systole r), r2 (end-diastole r) and p/r. c was fixed at the actual value of 2.75. Parameter error for r1, r2, p/r was the final parameter from optimisation minus 1.45cm, 2.05 and 0.4 respectively. Parameter error for the average and difference in r was the value derived from the final optimisation parameter minus 1.75cm and 0.6cm respectively.

For comparison purposes, the optimisation procedure was repeated with 50 sets of data created from the original 40 catheter measurements with uniform error added with standard deviation equal to that added to the average transformed data. The

optimisation procedure was also repeated with 50 sets of data created from the first 20 or second 20 original measurements only with standard deviation equal to that added to the average transformed data. In this case the optimisation procedure was used to find the parameters r1 only or r2 only, respectively, and p/r.

Same Segment Ratio Transformation to Reduce Biased Unmodelled Error

Generation of test data was accomplished by running the numerical model with the parameters r = 1.75cm, p/r = 0.4 and c = 2.75 to generate 20 catheter measurements. From these 20 measurements 20 additional transformed variables were calculated. These 20 additional variables were: V_1/V_2, V_1/V_4, V_1/V_7, V_2/V_4, V_2/V_7, V_4/V_7, V_3/V_5, V_3/V_8, V_5/V_8, V_4/V_9, V_{11}/V_{12}, V_{11}/V_{14}, V_{11}/V_{17}, V_{12}/V_{14}, V_{12}/V_{17}, V_{14}/V_{17}, V_{13}/V_{15}, V_{13}/V_{18}, V_{15}/V_{18}, V_{14}/V_{19}. These ratios contain measurements from the same segment at the same frequency, but with different current source electrode configuration. 50 sets of test data were generated by adding to this set of 40 catheter measurements random normally distributed error with mean of zero and desired standard deviation, s. The 20 original values had error added with a higher standard deviation to represent biased error. The 20 transformed values had a much smaller standard deviation of error added to represent some cancellation of biased error.

The optimisation procedure then was used to minimise the weighted mean squared difference between a set of all 40 or just the 20 low frequency test measurements and the equivalent data interpolated from the base data. The weights used had the appropriate ratio based on standard deviation of error applied as specified in (6.2.12). The optimisation procedure was used to find the parameter r. p/r and c were fixed. Parameter error for r was the final parameter from optimisation minus 1.75cm.

This procedure was repeated a number of times as detailed in the Section 6.4 for various values of standard deviation and different inclusion of measurement data (both frequencies/low frequency only).

6.4 Results

Results for this chapter are given in Tables 6.4.1 to 6.4.20. These tables summarise parameter error for each study. Standard deviation (s.d.) of error, mean error, minimum error and maximum error are tabulated for each parameter predicted by the inverse method in the study. Parameter error is the parameter predicted by the inverse method minus the actual test data parameter value. The parameter error is given in absolute form so different parameters with the same amount of error are actually a different percentage of error. Error data should be divided by 1.75, 0.4, 2.75 (and multiplied by 100) to generate percentage parameter error for r, p/r and c respectively. Also presented in the tables is standard deviation of parameters divided by half the range of parameters (difference between maximum and minimum optimisation bounds) in percent.

Performance with Uniformly Distributed Unmodelled Error

Tables 6.4.1 and 6.4.2 show parameter error from studies with 0.25% standard deviation normally distributed error added to measurement data. Table 6.4.3 shows parameter error from a study with 0.5% standard deviation normally distributed error added to measurement data. Tables 6.4.4 to 6.4.8 show parameter error from studies with 1% standard deviation normally distributed error added to measurement data. Tables 6.4.9 to 6.4.12 show parameter error for studies with 4% standard deviation normally distributed error added to measurement data. Table 6.4.13 shows parameter error for a study with 8% standard deviation normally distributed error added to measurement data. Different studies show different combinations of parameters fixed/predicted and different amounts of measurement data used (both frequencies/low frequency only).

Table 6.4.1: Parameter error. Data from both frequencies used. Added error standard deviation = 0.25%. Parameters used for test data: r = 1.75, p/r = 0.4, c = 2.75. Parameters fixed: none. Parameters solved for: r, p/r, c.

Parameter	s.d.	mean error	min. error	max. error	%s.d./range
r	0.0121	0.0080	-0.0160	0.0420	2.2
p/r	0.0122	-0.0073	-0.0298	0.0152	4.1
c	0.0728	0.0415	-0.0930	0.1727	18.2

Table 6.4.2: Parameter error. Low frequency data only. Added error standard deviation = 0.25%. Parameters used for test data: r = 1.75, p/r = 0.4, c = 2.75. Parameters fixed: none. Parameters solved for: r, p/r, c.

Parameter	s.d.	mean error	min. error	max. error	%s.d./range
r	0.0360	0.0093	-0.0548	0.0775	6.5
p/r	0.0173	-0.0058	-0.0414	0.0434	5.8
c	0.3367	0.0911	-0.3500	0.4500	84.2

Table 6.4.3: Parameter error. Data from both frequencies used. Added error standard deviation = 0.5%. Parameters used for test data: r = 1.75, p/r = 0.4, c = 2.75. Parameters fixed: none. Parameters solved for: r, p/r, c.

Parameter	s.d.	mean error	min. error	max. error	%s.d./range
r	0.0259	0.0099	-0.0428	0.0709	4.7
p/r	0.0191	-0.0039	-0.0454	0.0468	6.4
c	0.1754	0.0519	-0.3401	0.4500	43.85

Table 6.4.4: Parameter error. Data from both frequencies used. Added error standard deviation = 1%. Parameters used for test data: r = 1.75, p/r = 0.4, c = 2.75. Parameters fixed: none. Parameters solved for: r, p/r, c.

Parameter	s.d.	mean error	min. error	max. error	%s.d./range
r	0.0403	0.0159	-0.0650	0.1028	7.3
p/r	0.0403	-0.0007	-0.1140	0.0810	13.4
c	0.2831	0.0812	-0.3500	0.4500	70.8

Table 6.4.5: Parameter error. Data from both frequencies used. Added error standard deviation = 1%. Parameters used for test data: r = 1.75, p/r = 0.4, c = 2.75. Parameters fixed: c. Parameters solved for: r, p/r.

Parameter	s.d.	mean error	min. error	max. error	%s.d./range
r	0.0312	0.0061	-0.0680	0.0768	5.7
p/r	0.0505	-0.0037	-0.1877	0.0947	16.8

Table 6.4.6: Parameter error. Low frequency data only. Added error standard deviation = 1%. Parameters used for test data: r = 1.75, p/r = 0.4, c = 2 .75. Parameters fixed: c. Parameters solved for: r, p/r.

Parameter	s.d.	mean error	min. error	max. error	%s.d./range
r	0.0337	0.0037	-0.0578	0.0668	6.1
p/r	0.0562	-0.0063	-0.1288	0.0997	18.7

Table 6.4.7: Parameter error. Data from both frequencies used. Added error standard deviation = 1%. Parameters used for test data: r = 1.75, p/r = 0.4, c = 2.75. Parameters fixed: p/r. Parameters solved for: r, c.

Parameter	s.d.	mean error	min. error	max. error	%s.d./range
r	0.0394	0.0070	-0.0676	0.0631	7.2
c	0.2827	0.0407	-0.3500	0.4500	70.7

Table 6.4.8: Parameter error. Data from both frequencies used. Added error standard deviation = 1%. Parameters used for test data: r = 1.75, p/r = 0.4, c = 2.75. Parameters fixed: p/r, c. Parameters solved for: r.

Parameter	s.d.	mean error	min. error	max. error	%s.d./range
r	0.0075	0.0073	-0.0107	0.0250	1.4

Table 6.4.9: Parameter error. Data from both frequencies used. Added error standard deviation = 4%. Parameters used for test data: r = 1.75, p/r = 0.4, c = 2.75. Parameters fixed: none. Parameters solved for: r, p/r, c.

Parameter	s.d.	mean error	min. error	max. error	%s.d./range
r	0.1061	0.0133	-0.1920	0.2452	19.3
p/r	0.1713	-0.0322	-0.3000	0.2335	57.1
c	0.3744	0.1016	-0.3500	0.4500	93.6

Table 6.4.10: Parameter error. Data from both frequencies used. Added error standard deviation = 4%. Parameters used for test data: r = 1.75, p/r = 0.4, c = 2.75. Parameters fixed: c. Parameters solved for: r, p/r.

Parameter	s.d.	mean error	min. error	max. error	%s.d./range
r	0.1070	0.0327	-0.1203	0.2598	19.5
p/r	0.1804	-0.0114	-0.3000	0.2487	60.1

Table 6.4.11: Parameter error. Low frequency data only. Added error standard deviation = 4%. Parameters used for test data: r = 1.75, p/r = 0.4, c = 2.75. Parameters fixed: c. Parameters solved for: r, p/r.

Parameter	s.d.	mean error	min. error	max. error	%s.d./range
r	0.1817	0.0483	-0.1407	0.5500	33.0
p/r	0.2068	-0.0215	-0.3000	0.3000	68.9

Table 6.4.12: Parameter error. Data from both frequencies used. Added error standard deviation = 4%. Parameters used for test data: r = 1.75, p/r = 0.4, c = 2.75. Parameters fixed: p/r, c. Parameters solved for: r.

Parameter	s.d.	mean error	min. error	max. error	%s.d./range
r	0.0367	-0.0025	-0.0742	0.0780	6.7

Table 6.4.13: Parameter error. Data from both frequencies used. Added error standard deviation = 8%. Parameters used for test data: r = 1.75, p/r = 0.4, c = 2.75. Parameters fixed: p/r, c. Parameters solved for: r.

Parameter	s.d.	mean error	min. error	max. error	%s.d./range
r	0.0921	0.0020	-0.1720	0.2176	16.7

Average/Difference Transformation to Reduce Biased Unmodelled Error

Tables 6.4.14 to 6.4.17 show the effect of average/difference transformation (as discussed in Section 6.3) on prediction error. Table 6.4.14 is from a study using the transformations, whereas Table 6.4.15 to 6.4.17 are from equivalent studies not using the transformations but with similar measurement error magnitude added.

Table 6.4.14: Parameter error using average/difference transformation. Data from both frequencies used. Average error standard deviation = $4\% \times V_{average}$ and difference error standard deviation = $1\% \times V_{average}$. Parameters used for test data: r1 = 1.45, r2 = 2.05, p/r = 0.4, c = 2.75. Parameters fixed: c = 2.75. Parameters solved for simultaneously: r1, r2, p/r.

Parameter	s.d.	mean error	min. error	max. error	%s.d./range
r1	0.0313	0.0012	-0.0733	0.0688	5.7
r2	0.0600	-0.0213	-0.1760	0.1049	10.9
Diff. r	0.0290	-0.0225	-0.1028	0.0360	5.3
Av. r	0.0456	-0.0100	-0.1246	0.0869	8.3
p/r	0.0536	-0.0267	-0.2014	0.0745	17.9

Table 6.4.15: Parameter error using no transformation. Data from both frequencies used. Error standard deviation = $4\% \times V_{average}$. Parameters used for test data: r1 = 1.45, r2 = 2.05, p/r = 0.4, c =2.75. Parameters fixed: c = 2.75. Parameters solved for simultaneously: r1, r2, p/r.

Parameter	s.d.	mean error	min. error	max. error	%s.d./range
r1	0.0716	-0.0039	-0.1137	0.1487	13.0
r2	0.1454	-0.0124	-0.2380	0.2500	26.4
Diff. r	0.0744	-0.0085	-0.1243	0.1297	13.5
Av. r	0.1084	-0.0081	-0.1758	0.1993	19.7
p/r	0.1703	-0.0634	-0.3000	0.2025	56.8

Table 6.4.16: Parameter error using no transformation. Data from both frequencies used. Error standard deviation = 4%×$V_{average}$. Parameters used for test data: r1 = 1.45, p/r = 0.4, c = 2.75. Parameters fixed: c = 2.75. Parameters solved for: r1, p/r.

Parameter	s.d.	mean error	min. error	max. error	%s.d./range
r1	0.0575	0.0109	-0.1083	0.1194	10.5
p/r	0.1630	-0.0312	-0.3000	0.2194	54.3

Table 6.4.17: Parameter error using no transformation. Data from both frequencies used. Error standard deviation = 4%×$V_{average}$. Parameters used for test data: r2 = 2.05, p/r = 0.4, c =2.75. Parameters fixed: c = 2.75. Parameters solved for: r2, p/r.

Parameter	s.d.	mean error	min. error	max. error	%s.d./range
r2	0.1589	0.0104	-0.2430	0.2500	28.9
p/r	0.1838	-0.0428	-0.3000	0.2193	61.3

Same Segment Ratio Transformation to Reduce Biased Unmodelled Error

Table 6.4.18 to 6.4.20 are all from studies using same-segment ratio transformations (as discussed in Section 6.3). Table 6.4.18 is from a study using data from both frequencies and lower added measurement error. A comparison study not using the transformations would be the study in Table 6.4.12. Table 6.4.19 is from an equivalent study with twice as much error. A comparison study not using the transformations would be the study in Table 6.4.13. Finally Table 6.4.20 is from a study equivalent to Table 6.4.19 but with only low frequency data used.

Table 6.4.18: Parameter error using same-segment ratio transformation. Data from both frequencies used. Error standard deviation = 4% and same-segment ratio error = $1\% \times V_{ratio}$. Parameters used for test data: r = 1.75, p/r = 0.4, c = 2.75. Parameters fixed: p/r = 0.4, c = 2.75. Parameters solved for: r.

Parameter	s.d.	mean error	min. error	max. error	%s.d./range
r	0.0102	0.0044	-0.0120	0.0241	1.9

Table 6.4.19: Parameter error using same-segment ratio transformation. Data from both frequencies used. Error standard deviation = 8% and same-segment ratio error = $2\% \times V_{ratio}$. Parameters used for test data: r = 1.75, p/r = 0.4, c = 2.75. Parameters fixed: p/r = 0.4, c = 2.75. Parameters solved for: r.

Parameter	s.d.	mean error	min. error	max. error	%s.d./range
r	0.0270	-0.0013	-0.0588	0.0660	4.9

Table 6.4.20: Parameter error using same-segment ratio transformation. Low frequency data only. Error standard deviation = 8% and same-segment ratio error = $2\% \times V_{ratio}$. Parameters used for test data: r = 1.75, p/r = 0.4, c = 2.75. Parameters fixed: p/r = 0.4, c = 2.75. Parameters solved for: r.

Parameter	s.d.	mean error	min. error	max. error	%s.d./range
r	0.0413	0.0031	-0.1090	0.1184	7.5

6.5 Discussion

The mean error presented in the results gives the sort of error that can be expected in the average parameter values predicted when random noise with mean of zero is present in the catheter measurements. The standard deviation is a more appropriate indicator of the effect of biased error, or a single unaveraged parameter prediction. Values of %s.d./range close to 100 indicate no predicting ability in the case of biased error. In general, the mean parameter error is quite low throughout the results, suggesting that random noise with mean of zero can be reduced through averaging the parameter predictions (however, filtering the measurement data would probably give better performance).

As indicated in the first part of the results, it would seem that the inverse mapping is very sensitive to unmodelled error. Even with only 1% measurement data error the parameter error standard deviation is 10 times that in the last chapter (Table 5.3.7) and on the order of several percent for both r and p/r. However with just this 1% error c is almost unpredictable (Table 6.4.4). With 0.25% error c is also unpredictable from just low frequency data (Table 6.4.2). The data supports the conclusion in the last chapter that frequency is primarily responsible for separating c from r. With 1% error, fixing c or p/r only, has marginal effect on improving the accuracy of the other parameters. Accuracy is only significantly improved when both p/r and c are fixed. It would appear that c and p/r can not be predicted from a distance away from the myocardium (as modelled in this chapter) when this level of error is present. Filtering could probably be employed to reduce random error through filtering of measurement data and/or extensions to the method as discussed later, however it would not reduce biased error since it does not have a mean of zero.

Average/difference transformation appears to be useful in improving the accuracy of the difference in r, equivalent to stroke volume. Parameter error was reduced two to three times using the technique between table 6.4.15 and 6.4.14. Additional studies used for comparison purposes, Tables 6.4.16 and 6.4.17, show a marked decrease in accuracy of predicting parameters when r is larger. This would suggest the length-of-catheter to r ratio should be made as large as possible to improve accuracy. Alternatively, placing the catheter closer to the myocardium may help. These two

tables when compared to Table 6.4.15 also suggest there is no significant difference between inverse mapping two single measurements separately or simultaneously coupled in the p/r variable. The p/r value given is similar to an average of that given by the independent inverse mappings. It should be noted that the average/difference transformation only works because the biased error is the same at the two different r values, allowing some sort of cancellation.

Same segment ratio transformation also appears to be very useful. Error in Tables 6.4.18 and 6.4.19 were reduced by a factor of about three times over Tables 6.4.12 and 6.4.13. It should be noted that this transformation relies on having different source electrode configurations. Otherwise, the only way of getting a different measurement across the same segment is to change the frequency. The transformation may cancel out biased error such as catheter manufacturing error or local field effects on electrodes such as trabeculations.

The extension of the distance function technique to incorporate a priori assumptions about relative error magnitude of catheter measurements, appeared to be useful, based on its applications with the two transformations.

A further extension of the distance function technique to incorporate a priori information about the probability of different parameters occurring, maybe useful for filtering out random error from measurement data and allow the technique to solve non-unique mappings by making them unique with added probability information. Applying filtering may also speed up the optimisation.

Limitations of the work in this chapter are, that like the last chapter, results were from a two-dimensional model rather than a realistic three-dimensional model. Other limitations are that the extended distance function technique assumed a normal distribution of error. This is probably a reasonable assumption based on the ideas of the central limit theorem. However in practise a different distribution could probably be replaced with a normal distribution with the same standard deviation (second moment of inertia) with little error. Using the normally distributed error assumption allows optimisation of the natural logarithm of the probability using specialised, more efficient optimisation routines. When inverse mapping data in this chapter, the

ratio of error standard deviations was set to the known ratios of added error, in a real application it may be different. Something that was not addressed in this chapter was that of non-independent error. This is especially important when adding transformations of variables to the distance function. The weighting of non-independent variables should be reduced/shared.

In all the studies in this chapter parameters optimised were in the form of the variables r, p/r, c. Transforming these variables (or carefully selecting parameters) into new variables may make the optimisation search space smoother. Optimisation algorithms work best with particular function shapes. However one may have to recalculate the base data based on an even grid of the new variables to enable easy setting of optimisation bounds. Changing the optimisation to optimise the probability directly would be impractical due to the large range of values. The distance function essentially is the natural logarithm of the probability, greatly compressing this large range of values.

When a variable was fixed during optimisation it was set at a known value. In practise one may not know the fixed parameters exactly and fixing them to an incorrect value may give some error. An implicit assumption throughout this chapter and the last was that frequency caused a known change in conductivity. The effect of this frequency change not being known exactly, may give some error.

6.6 Conclusion

The work in this chapter suggests it is not possible to determine catheter position or myocardium conductivity very accurately when placed a large distance from the myocardium when moderate error is present. The inverse mapping is highly sensitive to unmodelled error. A catheter may have to be placed close to the myocardium to get some idea of catheter position or myocardium conductivity under experimental conditions. A longer length catheter may have the effect of achieving the same result. The extended distance function technique developed in this chapter allowed parameter error to be reduced. Similar to Chapter 5, the major limitation of the work in this chapter is that the results are based on a 2D model, not a 3D model.

Chapter 7. Conclusion

Summary

The conductance catheter is the one of the most promising techniques for use as an implantable blood flow sensor. While the low power consumption of the technique is one of its main advantages, the existing accuracy of the technique is insufficient for the intended application. Improvement in accuracy may be possible if more of the data available from the conductance catheter is utilised. The problem then is the complex task of mapping available data to changes in ventricle geometry.

Through development of numerical models the accuracy of the conductance catheter was assessed. The models provided a controlled experimental environment.

Catheter movement was found to be highly significant as well as blood conductivity/myocardium conductivity ratio.

A method for mapping a large number of conductance catheter measurements to ventricle geometry was developed. This involved finding the inverse solution to a numerical model. Two approaches were employed, a new technique and neural networks. These approaches were tested on a two-dimensional simplified heart model. The new technique was shown to be capable of close to exact inverse mapping, while a wide array of neural network techniques failed comprehensively. Numerical model derivative information was used to gather an insight into the inverse mapping. Derivative angles between different numerical model parameters were calculated to determine the relative effect and separability of different model parameters.

The new inverse technique was applied to data with error. The effect of error and how it related to angles between the derivative vectors of various variables was examined. The technique was further developed and applied to reducing biased experimental error, due to catheter geometry difference between model and experiment and other unmodelled error. The improved technique significantly reduced error from these sources. The improved technique also has the potential to be used in a temporal filter of random unbiased error in the data.

The inverse technique developed is relatively computationally intensive and requires a parameterized numerical model to be developed to use it, however it offers the possibility of determining blood flow accurately from a conductance catheter. The parameterised numerical model provides a convenient way of incorporating a priori geometry and conductivity information and the improved new inverse technique provides a convenient way of incorporating a priori error and parameter dynamics information.

Future Work

Many opportunities are available for future work in relation to this topic.

The work of investigation one (chapter four) is limited to one particular catheter geometry. The catheter used was relatively short. A longer catheter may give different results. Modelling a different catheter geometry may require extending the models into the atria and pulmonary artery/aorta. It was assumed no current flowed outside the heart myocardium. In reality some current will flow through the liver and epicardial fat (if it is thin or non-existent) into surrounding structures. Fibre direction, even though the resulting conductivity can probably be safely assumed to be equivalent to some isotropic value, could be incorporated into the models. Trabeculation, even though the resulting model can probably be safely assumed to be a smooth border between blood and myocardium, could be incorporated into the model. Rough experimental validation of aim three could be achieved by wiggling an equivalent conductance catheter around inside a patient and by changing the blood/myocardium conductivity ratio using saline injection.

The inverse mapping technique could be further developed in a number of ways. The work done in the second and third investigation chapters could be applied to three-dimensional models like those used in investigation one rather than a simplified two-dimensional model. It is desirable to perform experimental validation, but even if blood flow can be measured independently, a major problem is gathering the required geometry and conductivity information to compare with that predicted by the model.

The inverse mapping method provides the potential to determine tissue conductivity and its variability more accurately than experimental techniques, due to no damage to the tissue, in a wide array of living animal or even human subjects. For instance a catheter with closely spaced electrodes could be placed in the blood pool next to the heart wall in desired location, and assumed fibre direction and geometry could be used to generate numerical model data for the inverse solution of tissue conductivity.

Other types of sensor could be developed to overcome regurgitation error problems with the conductance catheter technique. Ultrasound could be explored, as a future improvement in battery technology (fuel cells?) could make such techniques more feasible for implantable use. Studies could investigate how well a single crystal catheter could measure flow in a pulmonary artery of a pulmonary hypertensive patient with heterogeneous velocity profile. Also viscous pressure drop measurement of velocity using some sort of conductance catheter type correction for blood viscosity (from hematocrit) and flow cross-sectional area could be explored. New concepts based on biotechnology/nanotechnology such as collecting/synthesizing and then releasing and measuring a marker in the blood to obtain blood flow using indicator dilution formulae could be another future option.

This thesis has developed and tested new conductance catheter methods, and has moved us a step closer to enabling practical development of an implantable blood flow and pressure monitor.

References

[1] D. L. Franklin, N. W. Watson, and R. L. Van Citters, "Blood velocity telemetered from unanaesthetised animals," *Nature*, vol. 203, pp. 528–530, Aug. 1964.

[2] A. Ohlsson, S. H. Kubo, D. Steinhaus, D. T. Connelly, S. Adler, C. Bitkover, R. Nordlander, L. Ryden, and T. Bennett, "Continuous ambulatory monitoring of absolute right ventricular pressure and mixed venous oxygen saturation in patients with heart failure using an implantable haemodynamic monitor," *European Heart Journal*, vol. 22, no. 11, pp. 942–954, Jun. 2001.

[3] D. M. Steinhaus, R. Lemery, D. R. Bresnahan Jr, L. Handlin, T. Bennett, A. Moore, D. Cardinal, L. Foley, and R. Levine, "Initial experience with an implantable hemodynamic monitor," *Circulation*, vol. 93, no. 4, pp. 745–752, Feb. 1996.

[4] A. Magalski, P. Adamson, F. Gadler, M. Boehm, D. Steinhaus, D. Reynolds, K. Vlach, C. Linde, B. Cremers, B. Sparks, and T. Bennett, "Continuous ambulatory right heart pressure measurements with an implantable hemodynamic monitor: a multicenter, 12-month follow-up study of patients with chronic heart failure," *Journal of Cardiac Failure*, vol. 8, no. 2, pp. 63–70, Apr. 2002.

[5] C. Berton and B. Cholley, "Equipment review: new techniques for cardiac measurement – oesophageal doppler, fick principle using carbon dioxide, and pulse contour analysis," *Critical Care*, vol. 6, no. 3, pp. 216–221, Jun. 2002.

[6] C. E. Ditmyer, M. Shively, D. B. Burns, and R. T. Reichman, "Comparison of continuous with intermittent bolus thermodilution cardiac output measurements," *Am. J. Crit. Care*, vol. 4, no. 6, pp. 460–465, Nov. 1995.

[7] R. Linton, D. Band, T. O'Brien, M. Jonas, and R. Leach, "Lithium dilution cardiac output measurement: a comparison with thermodilution," *Crit. Care Med.*, vol. 25, no. 11, pp. 1796–1800, Nov. 1997.

[8] S. R. Montgomery, "Blood flow measurements," in *Biomechanics and related bio-engineering topics: proceedings of a symposium held in Glascow, September 1964*, R. M. Kenedi, Ed. Pergamon Press, 1965, ch. 22, pp. 249–264.

[9] R. S. C. Cobbold, *Transducers for biomedical measurements*. John Wiley & Sons, Inc., 1974, pp. 244–321.

[10] R. Gent, *Applied physics and technology of diagnostic ultrasound*, Australia: Milner Publishing, 1997.

[11] G. P. Ussia, A. Privitera, M. Campisi, M. Carminati, and F. De Luca, "Intracardiac echocardiography using the AcuNav™ ultrasound catheter during percutaneous closure of multiple atrial septal defects," *Ital. Heart J.*, vol. 5, no. 5, pp. 392–395, May 2004.

[12] R. F. Bonner, T. R. Clem, P. D. Bowen, and R. L. Bowman, "Laser doppler continuous real-time monitor of pulsatile and mean blood flow in tissue microcirculation," in *Scattering Techniques, Applied to Supra-Molecular and Nonequilibrium Systems*, S. H. Chen, B. Chu, and R. Nossal, Ed. New York: Plenum, 1981, pp. 685–702.

[13] P. A. White and A. N. Redington, "Right ventricular volume measurement: can conductance do it better?," *Physiol. Meas.*, vol. 21, no. 3, pp. R23–R41, Aug. 2000.

[14] J. Baan, E. T. van der Velde, H. G. de Bruin, G. J. Smeenk, J. Koops, A. D. van Dijk, D. Temmerman, J. Senden, and B. Buis, "Continuous measurement of left ventricular volume in animals and humans by conductance catheter," *Circulation*, vol. 70, no. 5, pp. 812–823, Nov. 1984.

[15] J. Baan, E. T. van der Velde, P. Steendijk, and J. Koops, "Calibration and application of the conductance catheter for ventricular volume measurement," *Automedica*, vol. 11, pp. 357–365, 1989.

[16] B. Gopakumaran, P. Osborn, J. H. Petre, and P. A. Murray, "A new technique to measure and track blood resistivity in intracardiac impedance volumetry," *Journal of Clinical Monitoring*, vol. 13, no. 6, pp. 363–371, Nov. 1997.

[17] J. C. Woodard, C. D. Bertram, and B. S. Gow, "Detecting right ventricular volume changes using the conductance catheter," *PACE*, vol. 15, no. 12, pp. 2283–2294, Dec. 1992.

[18] E. M. Staal, P. Steendijk, G. Koning, J. Dijkstra, J. W. Jukema, and J. Baan, "Continuous on-line measurement of absolute left ventricular volume by transcardiac conductance: angiographic validation in sheep," *Crit. Care Med.*, vol. 30, no. 6, pp. 1301–1305, Jun. 2002.

[19] W. S. Sageman and D. E. Amundson, "Thoracic electrical bioimpedance measurement of cardiac output in postaortocoronary bypass patients," *Crit. Care Med.*, vol. 21, no. 8, pp. 1139–1142, Aug. 1993.

[20] S. A. Loer, W. Schlack, D. Ebel, and J. Tarnow, "Effects of partial liquid ventilation on regional pulmonary blood flow distribution of isolated rabbit lungs," *Crit. Care Med.*, vol. 28, no. 5, pp. 1522–1525, May 2000.

[21] C. B. Saper, S. Iversen, and R. Frackowiak, "Integration of sensory and motor function: the association areas of the cerebral cortex and the cognitive capabilities of the brain," in *Principles of neural science, fourth edition*, E. R. Kandel, J. H. Schwartz, and T. M. Jessell, Ed. McGraw-Hill, 2000, ch. 19, pp. 375–379.

[22] K. R. Foster and H. P. Schwan, "Dielectric properties of tissues and biological materials: a critical review," *Critical Reviews in Biomedical Engineering*, vol. 17, no. 1, pp. 25-104, 1989.

[23] T. Zhao, "Electrical impedance and haematocrit of human blood with various anticoagulants," *Physiol. Meas.*, vol. 14, pp. 299-307, 1993.

[24] J. W. Dellimore and R. G. Gosling, "Change in blood conductivity with flow rate," *Medical and Biological Engineering*, pp. 904-913, Nov. 1975.

[25] M. Ninomiya, M. Fujii, M. Niwa, K. Sakamoto and H. Kanai, "Physical properties of flowing blood," *Biorheology*, vol. 25, pp. 319-328, 1988.

[26] F. Jaspard and M. Nadi, "Dielectric properties of blood: an investigation of temperature dependence," *Physiol. Meas.*, vol. 23, pp. 547-554, 2002.

[27] R. Pethig, "Dielectric properties of body tissues," *Clin. Phys. Physiol. Meas.*, vol. 8, Suppl. A, pp. 5-12, 1987.

[28] H. P. Schwan, "Electrical properties of blood and its constituents," *Blut*, vol. 46, pp. 185-197, 1983.

[29] P. Steendijk, E. T. Van Der Velde and J. Baan, "Dependence of anisotropic myocardial electrical resistivity on cardiac phase and excitation frequency," *Basic Research in Cardiology*, vol. 89, pp. 411-426, 1994.

[30] P. Steendijk, G. Mur, E. T. Van Der Velde and J. Baan, "The four-electrode resistivity technique in anisotropic media: theoretical analysis and application on myocardial tissue in vivo," *IEEE Transactions on Biomedical Engineering*, vol. 40, no. 11, Nov. 1993.

[31] M. A. Fallert, M. S. Mirotznik, S. W. Downing, E. B. Savage, K. R. Foster, M. E. Josephson and D. K. Bogen, "Myocardial electrical impedance mapping of ischemic sheep hearts and healing aneurysms," *Circulation*, vol. 87, pp. 199-207, 1993.

[32] M. Osypka and E. Gersing, "Tissue impedance spectra and the appropriate frequencies for EIT," *Physiol. Meas.*, vol. 16, pp. A49-A55, 1995.

[33] S. Rush, J. A. Abildskov and R. McFee, "Resistivity of body tissues at low frequencies," *Circulation Research*, vol. 12, pp. 40-50, Jan. 1963.

[34] F. A. Duck, *Physical properties of tissue*. Academic Press, New York, London, 1990.

[35] L. A. Geddes and L. E. Baker, "The specific resistance of biological material-a compendium of data for the biomedical engineer and physiologist," *Med. & biol. Engng.*, vol. 5, pp. 271-293, 1967.

[36] C. Gabriel, S. Gabriel and E. Corthout, "The dielectric properties of biological tissues: i. Literature survey," *Phys. Med. Biol.*, vol. 41, pp. 2231-2249, 1996.

[37] S. Gabriel, R. W. Lau and C. Gabriel, "The dielectric properties of biological tissues: ii. measurments in the frequency range 10 Hz to 20 GHz," *Phys. Med. Biol.*, vol. 41, pp. 2251-2269, 1996.

[38] S. Gabriel, R. W. Lau and C. Gabriel, "The dielectric properties of biological tissues: iii. Parametric models for the dielectric spectrum of tissues," *Phys. Med. Biol.*, vol. 41, pp. 2271-2293, 1996.

[39] F. Jaspard, M. Nadi and A. Rouane, "Dielectric properties of blood: an investigation of haematocrit dependence," *Physiol. Meas.*, vol. 24, pp. 137-147, 2003.

[40] E. D. Trautman and R. S. Newbower, "A practical analysis of the electrical conductivity of blood," *IEEE Transactions on Biomedical Engineering*, vol. 30, no. 3, Mar. 1983.

[41] E. Zheng, S. Shao and J. G. Webster, "Impedance of skeletal muscle from 1 Hz to 1 MHz," *IEEE Transactions on Biomedical Engineering*, vol. 31, no. 6, Jun. 1984.

[42] R. F. Rushmer, D. K. Crystal and C. Wagner, "The functional anatomy of ventricular contraction," *Circ. Res.*, vol. 1, pp. 162-170, 1953.

[43] P. M. F. Nielsen, I. J. Le Grice, B. H. Smaill and P. J. Hunter, "Mathematical model of geometry and fibrous structure of the heart," *Am. J. Physiol.*, vol. 260, pp. H1365-H1378, 1991.

[44] K. F. Augenstein, E. R. McVeigh and A. A. Young, "Magnetic resonance imaging and ventricle mechanics," *Phil. Trans. R. Soc. Lond.*, vol. 359, pp. 1263-1275, 2001.

[45] P. J. Hunter, A. J. Pullan and B. H. Smaill, "Modeling total heart function," *Annu. Rev. Biomed. Eng.*, vol. 5, pp. 147-77, 2003.

[46] R. L. Winslow, D. F. Scollan, A. Holmes, C. K. Yung, J. Zhang and M. S. Jafri, "Electrophysiological modeling of cardiac ventricluar function: from cell to organ," *Annu. Rev. Biomed. Eng.*, vol. 2, pp. 119-55, 2000.

[47] V. Schejbal, "Epikardiales fettgewebe der rechten herzkammer – morphologie, morphometrie und funktionelle bedeutung," *Pneumologie*, vol. 43, pp. 490-499, 1989.

[48] D. K. Tansey, Z. Aly and M. N. Sheppard, "Fat in the right ventricle of the normal heart," *Histopathology*, vol. 46, pp. 98-104, 2005.

[49] *Magnetic Resonance Imaging, 2nd ed., vol. 2*, D. D. Stark and W.G. Bradley, Jr, Ed. Mosby Year Book, St. Louis, 1992.

[50] M. R. Paling and B. R. J. Williamson, "Epipericardial fat pad: CT findings," *Radiology*, vol.165, pp. 335-339, 1987.

[51] *MRI and CT of the Cardiovascular System*, C. B. Higgins and A. De Roos, Ed. Lippincott Williams & Wilkins, Philadelphia, Pa., London, 2006.

[52] Y. Wang, S. J. Riederer and R. L. Ehman, "Respiratory motion of the heart: kinematics and the implications for spatial resolution in coronary imaging," *MRM*, vol. 33, pp. 713-719, 1995.

[53] D. Manke, P. Rösch, K. Nehrke, P. Börnert and O. Dössel, "Model evaluation and calibration for prospective respiratory motion correction in coronary MR angiography based on 3-D image registration," *IEEE Transactions on Medical Imaging*, vol. 21, no. 9, pp. 1132-1141, Sep. 2002.

[54] K. McLeish, D. L. G. Hill, D. Atkinson, J. M. Blackall and R. Razavi, "A study of motion and deformation of the heart due to respiration," *IEEE Transactions on Medical Imaging*, vol. 21, no. 9, pp. 1142-1150, Sep. 2002.

[55] G. Schechter, C. Ozturk, J. R. Resar and E. R. McVeigh, "Respiratory motion of the heart from free breathing coronary angiograms," *IEEE Transactions on Medical Imaging*, vol. 23, no. 8, pp. 1046-1056, Aug. 2004.

[56] D. Manke, P. Rösch, K. Nehrke, P. Börnert and O. Dössel, "Respiratory motion in coronary magnetic resonance angiography: a comparison of different motion models," *J. Magn. Reson. Imaging*, vol. 15, pp. 661-671, 2002.

[57] P. G. Danias, M. Stuber, R. M. Botnar, K. V. Kissinger, R. R. Edelman and W. J. Manning, "Relationship between motion of coronary arteries and diaphragm during free breathing: lessons from real-time MR imaging," *AJR*, vol. 172, pp. 1061-1065, Apr. 1999.

[58] M. Francone, S. Dymarkowski, M. Kalantzi and J. Bogaert, "Real-time cine MRI of ventricular septal motion: a novel approach to assess ventricular coupling," *J. Magn. Reson. Imaging*, vol. 21, pp. 305-309, 2005.

[59] A. P. Yoganathan, Z. He, and S. C. Jones, "Fluid mechanics of heart valves," *Annu. Rev. Biomed. Eng.*, vol. 6, pp. 331-62, 2004.

[60] J. Lotz, C. Meier, A. Leppert and M. Galanski, "Cardiovascular flow measurement with phase-contrast MR imaging: basic facts and implementation," *Radiographics*, vol. 22, pp. 651-671, 2002.

[61] G. P. Chatzimavroudis, J. N. Oshinski, R. H. Franch, P. G. Walker, A. P. Yoganathan and R. I. Pettigrew, "Evaluation of the precision of magnetic resonance phase velocity mapping for blood flow measurements," *Journal of Cardiovascular Magnetic Resonance*, vol. 3, no. 1, pp. 11-19, 2001.

[62] C. P. Cheng, R. J. Herfkens, A. L. Lightner, C. A. Taylor and J. A. Feinstein, "Blood flow conditions in the proximal pulmonary arteries and vena cavae: healthy children during upright cycling exercise," *Am J Physiol Heart Circ Physiol*, vol. 287, pp. H921-H926, 2004.

[63] H. G. Bogren, R. H. Klipstein, R. H. Mohiaddin, D. N. Firmin, S. R. Underwood, R. S. O. Rees and D. B. Longmore, "Pulmonary artery distensibility and blood flow patterns: a magnetic resonance study of normal subjects and of patients with pulmonary arterial hypertension," *Am Heart J*, vol. 118, no. 5, pp. 990-999, 1989.

[64] E. Sloth, K. C. Houlind, S. Oyre, W. Y. Kim, E. M. Pedersen, H. S. Jørgensen and J. M. Hasenkam, "Three-dimensional visualization of velocity profiles in the human main pulmonary artery with magnetic resonance phase-velocity mapping," *Am Heart J*, vol. 128, no. 6, pp. 1130-1138, 1994.

[65] A. A. Tardivon, E. Mousseaux, F. Brenot, J. Bittoun, O. Jolivet, E. Bourroul and P. Duroux, "Quantification of hemodynamics in primary pulmonary hypertension with magnetic resonance imaging," *Am J Respir Crit Care Med*, vol. 150, pp. 1075-80, 1994.

[66] M. M. Hoeper, J. Tongers, A. Leppert, S. Baus, R. Maier and J. Lotz, "Evaluation of right ventricular performance with a right ventricular ejection thermodilution catheter and MRI in patients with pulmonary hypertension," *Chest*, vol. 120, pp. 502-507, 2001.

[67] M. Carlsson, P. Cain, C. Holmqvist, F. Stahlberg, S. Lundback and H. Arheden, "Total heart volume variation throughout the cardiac cycle in humans," *Am J Physiol Heart Circ Physiol*, vol. 287, pp. H243-H250, 2004.

[68] A. A. W. Roest, P. Kunz, H. J. Lamb, W. A. Helbing, E. E. Van Der Wall and A. De Roos, "Biventricular response to supine physical exercise in young adults assessed with ultrafast magnetic resonance imaging," *Am J Cardiol*, vol. 87, pp. 601-605, 2001.

[69] E. Hammarström, B. Wranne, F. J. Pinto, J. Puryear and R. L. Popp, "Tricuspid annular motion," *J Am Soc Echo*, vol. 4, pp. 131-9, 1991.

[70] S. Westaby, R. B. Karp, E. H. Blackstone and S. P. Bishop, "Adult human valve dimensions and their significance," *Am J Cardiol*, vol. 53, pp. 552-556, 1984.

[71] S. Dong, A. P. Crawley, J. H. MacGregor, Y. F. Petrank, D. W. Bergman, I. Belenkie, E. R. Smith, J. V. Tyberg and R. Beyar, "Regional left ventricular systolic function in relation to the cavity geometry in patients with chronic right ventricular pressure overload," *Circulation*, vol. 91, pp. 2359-2370, 1995.

[72] F. E. Rademakers, W. J. Rogers, W. H. Guier, G. M. Hutchins, C. O. Siu, M. L. Weisfeldt, J. L. Weiss and E. P. Shapiro, "Relation of regional cross-fibre shortening to wall thickening in the intact heart," vol. 89, pp. 1174-1182, 1994.

[73] I. Haber, D. N. Metaxas and L. Axel, "Using tagged MRI to reconstruct a 3D heartbeat," *Computing in Science & Engineering*, vol. 2, no. 5, pp.18-30, Sep/Oct 2000.

[74] I. Haber, D. N. Metaxas and L. Axel, "Three-dimensional systolic kinematics of the right ventricle," *Am J Physiol Heart Circ Physiol*, vol. 289, H1826-H1833, 2005.

[75] M. B. Buchalter, J. L. Weiss, W. J. Rogers, E. A. Zerhouni, M. L. Weisfeldt, R. Beyar and E. P. Shapiro, "Noninvasive quantification of left ventricular rotational deformation in normal humans using magnetic resonance imaging myocardial tagging," *Circulation*, vol. 81, pp. 1236-1244, 1990.

[76] R. Beyar, "From organs to molecules: steps and consequences," *Ann. N. Y. Acad. Sci.*, vol. 1047, pp. 1-12, 2005.

[77] A. Bouchard, C. B. Higgins, B. F. Byrd III, E. G. Amparo, L. Osaki and R. Axelrod, "Magnetic resonance imaging in pulmonary arterial hypertension," *Am J Cardiol*, vol. 56, pp. 938-942, 1985.

[78] J. T. Marcus, A. V. Noordegraaf, R. J. Roeleveld, P. E. Postmus, R. M. Heethaar, A. C. Van Rossum and A. Boonstra, "Impaired left ventricular filling due to right ventricular pressure overload in primary pulmonary hypertension," *Chest*, vol. 119, pp. 1761-1765, 2001.

[79] M. J. Kern, *The cardiac catheterization handbook, 4th ed.*, Mosby, Philadelphia, PA, 2003.

[80] R. M. Berne, *Cardiovascular physiology, 6th ed.*, Mosby Year Book, St. Louis, 1992.

[81] A. M. R. Agur and A. F. Dalley II, *Grants atlas of anatomy, 11 ed.*, Lippincott Williams & Wilkins, Philadelphia, 2005.

[82] B. R. Wilcox, A. C. Cook and R. H. Anderson, *Surgical anatomy of the heart, 3rd ed.*, Cambridge University Press, Cambridge, UK, New York, 2004.

[83] *Gray's anatomy, 39th ed.*, S. Standring Ed., Elsevier Churchill Livingstone, Edinburgh, New York, 2005.

[84] *Hurst's the heart, 9th ed., Volume 1*, R. W. Alexander, R. C. Schlant and V. Fuster Ed., McGraw Hill, Health Professions Division, New York, 1998.

[85] *Biomedical Engineering Fundamentals*, J. D. Bronzino Ed., CRC Press, 2006.

[86] W. R. Milnor, *Cardiovascular physiology*, Oxford University Press, New York, 1990.

[87] J. Baan, T. T. A Jong, P. L. M. Kerkhof, R. J. Moene, A. D. Van Dijk, E. T. Van Der Velde and J. Koops, "Continuous stroke volume and cardiac output from intra-ventricular dimensions obtained with impedance catheter," *Cardiovascular Research,* vol. 15, pp. 328-334, 1981.

[88] P. Steendijk, E. T. Van Der Velde and J. Baan, "Left ventricular stroke volume by single and dual excitation of conductance catheter in dogs," *Am. J. Physiol.*, vol. 264, pp. H2198-H2207, 1993.

[89] G. Iacobellis, D. Corradi and A. M. Sharma, "Epicardial adipose tissue: anatomic, biomolecular and clinical relationships with the heart," *Nat Clin Pract Cardiovasc Med*, vol. 2, no. 10, pp. 536-543, Oct. 2005.

[90] A. D'Avila, M. Scanavacca, E. Sosa, J. N. Ruskin and V. Y. Reddy, "Pericardial anatomy for the interventional electrophysiologist," *J Cardiovasc Electrophysiol*, vol. 14, pp. 422-430, Apr. 2003.

[91] G. Fricke, U. Studer and H. D. Scheu, "Pulsatile velocity of blood in the pulmonary artery of dogs: measurement by an ultrasound gauge," *Cardiovascular Research*, vol. 4, pp. 371-379, 1970.

[92] T. M. Wadas, "The implantable hemodynamic monitoring system," *Critical Care Nurse*, vol. 25, no. 5, pp. 14-27, Oct. 2005.

[93] M. D. Feldman, Y. Mao, J. W. Valvano, J. A. Pearce and G. L. Freeman, "Development of a multifrequency conductance catheter based system to determine LV function in mice," *The American Journal of Physiology*, vol. 278, pp. H1411-H1420, 2000.

[94] D. Georgakopoulos and D. A. Kass, "Estimation of parallel conductance by dual-frequency conductance catheter in mice," *The American Journal of Physiology*, vol. 279, pp. H443-H450, 2000.

[95] P. A. White, C. I. Brookes, H. B. Ravn, E. E. Stenbog, T.D. Christensen, R. R. Chaturvedi, K. Sorensen, V. E. Hjortdal and A. N. Redington, "The effect of changing excitation frequency on parallel conductance in different sized hearts," *Cardiovascular Research*, vol. 38, pp. 668-675, 1998.

[96] T. S. Gawne, K. S. Grey and R. E. Goldstein, "Estimating left ventricular offset volume using dual-frequency conductance catheters," *The Journal of Applied Physiology*, vol. 63, pp.872-876, 1987.

[97] B. Gopakumaran, J. H. Petre, P. K. Osborn and P. Schluter, "Method and apparatus to correct for electric current leakage in conductance volumetry;" US patent # 5,882,312, 1999.

[98] L. Kornet, J. J. Schreuder, E. T. Van Der Velde, J. Baan and J. R. Jansen, "A new approach to determine parallel conductance for left ventricular volume measurements," *Cardiovascular Research*, vol. 48, pp. 455-463, 2000.

[99] B. Gopakumaran, J. H. Petre, P. K. Osborn and P. Schluter, "Method and apparatus to correct for electric field non-uniformity in conductance catheter volumetry;" US patent # 5,971,933, 1999.

[100] S. Kun and R. A. Peura, "Analysis of conductance volumetric measurement error sources," *Med. & Biol. Eng. & Comput.*, vol. 32, pp. 94-100, 1994.

[101] A. Bishop, P. White, P. Oldershaw, R. Chaturvedi, C. Brookes and A. Redington, "Clinical application of the conductance catheter technique in the adult human right ventricle," *International Journal of Cardiology*, vol. 58, pp. 211-221, 1997.

[102] B. Gopakumaran, J. H. Petre, B. Sturm, R. D. White and P. A. Murray, "Estimation of current leakage in the left and right ventricular conductance volumetry using a dynamic finite element model," *IEEE Transactions on Biomedical Engineering*, vol. 47, no. 11, pp. 1476-1486, 2000.

[103] W.P. Segars. Development of a new dynamic NURBS-based cardiac-torso (NCAT) phantom., PhD dissertation, The University of North Carolina, May 2001.

[104] S. Krayer, K. Rehder, J. Vettermann, E. P. Didier and E. L. Ritman, "Position and motion of the human diaphragm during anesthesia-paralysis," *Anesthesiology*, vol. 70, pp. 891-898, 1989.

[105] C. Tei, J. P. Pilgrim, P. M. Shah, J. A. Ormiston and M. Wong, "The tricuspid valve annulus: study of size and motion in normal subjects and in patients with tricuspid regurgitation," *Circulation*, vol. 66, no. 3, pp. 665-671, 1982.

[106] R. W. Salo, "The theoretical basis of a computational model for the determination of volume by impedance," *Automedica*, vol. 11, pp. 299-310, 1989.

[107] R. W. Salo, "Method and apparatus for measuring ventricular volume;" US patent # 4,674,518, 1987.

[108] R. W. Salo, T. G. Wallner and B. D. Pederson, "Measurement of ventricular volume by intracardiac impedance: theoretical and empirical approaches," *IEEE Transactions on Biomedical Engineering*, vol. 33, no. 2, pp. 189-195, Feb. 1986.

[109] *Clinical cardiac pacing, second edition*, K. A. Ellenbogen, G. N. Kay, and B. L. Wilkoff, Ed. Saunders, 2000, ch. 11-12, pp. 293-324.

[110] *Clinical cardiac pacing, first edition*, K. A. Ellenbogen, G. N. Kay, and B. L. Wilkoff, Ed. Saunders, 1995, ch. 13, pp. 234-249.

[111] M. Schaldach, *Electrotherapy of the heart.* Springer-Verlag, 1992, pp. 105-143.